An efficient numerical approach to model wave overtopping of rubble mound breakwaters

M.L.A. Moretto

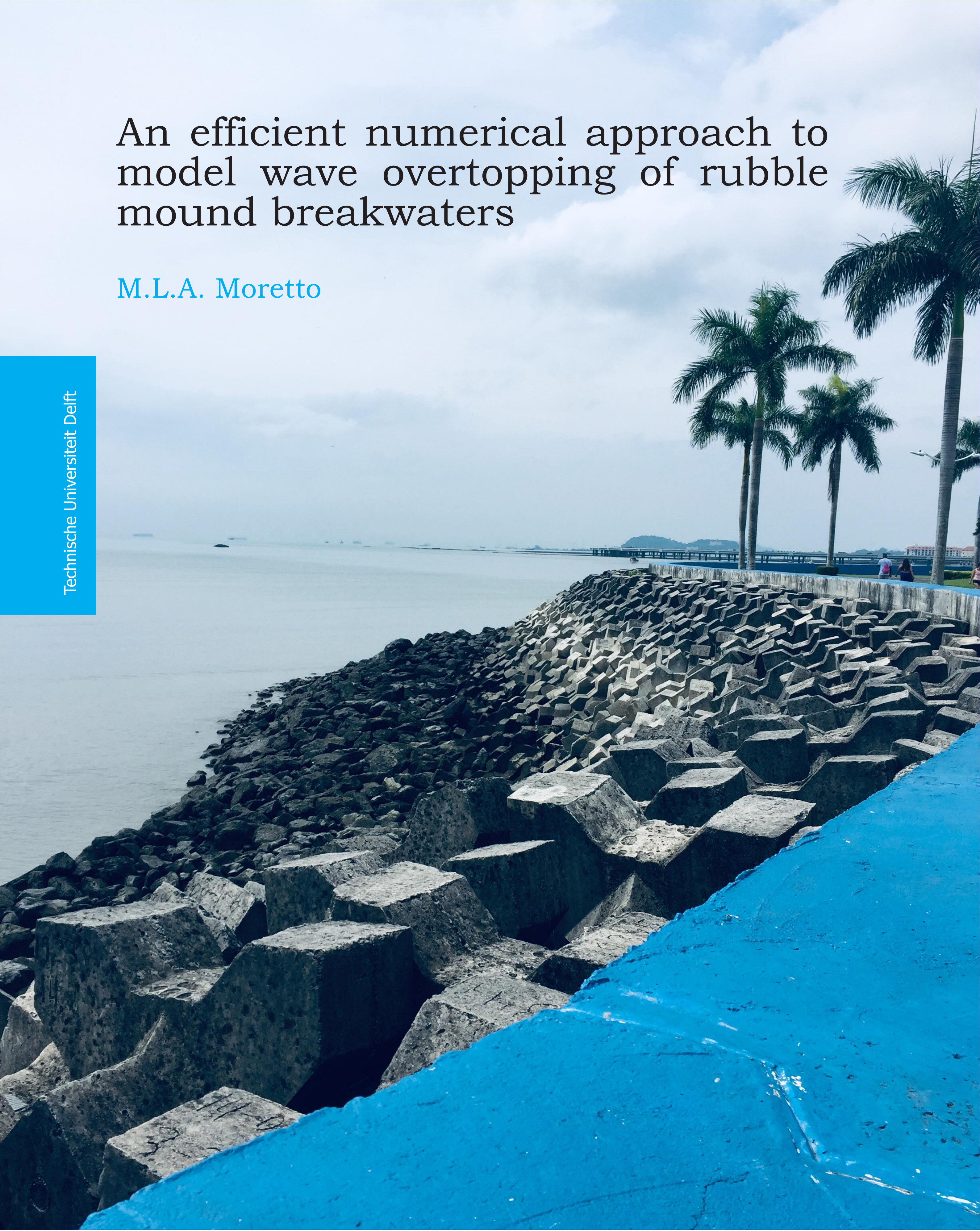

Technische Universiteit Delft

Delft University of Technology

Challenge the future

Photo cover image:
X-bloc breakwater with wave wall along the coastline of Panama City.
Source: Personal image,
September 2019
Copyright ©

The presented work was conducted and carried out in cooperation with
Royal HaskoningDHV.

An efficient numerical approach to model wave overtopping of rubble mound breakwaters

by

M.L.A. Moretto

For the degree of Master of Science in Civil Engineering at Delft University of Technology

February 17, 2020

DELFT UNIVERSITY OF TECHNOLOGY
DEPARTMENT OF
HYDRAULIC ENGINEERING

The undersigned hereby certify that they have read and recommend to the Faculty of Civil Engineering and Geosciences (CEG) for acceptance a thesis entitled

An efficient numerical approach to model wave overtopping of rubble mound breakwaters

by

M.L.A. Moretto

in partial fulfillment of the requirements for the degree of

MASTER OF SCIENCE CIVIL ENGINEERING AND GEOSCIENCES (CEG)
HYDRAULIC ENGINEERING

at the Delft University of Technology

Dated: February 17, 2020

Thesis committee:

Chairman:
Dr. ir. Antonini, A.
Delft University of Technology
Hydraulic Engineering
Coastal Engineering

Members:
Ir. van den Bos, J.
Delft University of Technology
Hydraulic Engineering
Coastal Engineering

Dr. Tissier, M.F.S.
Delft University of Technology
Hydraulic Engineering
Environmental Fluid Dynamics

Ir. van der Lem, C.
Royal HaskoningDHV
Maritime
Senior Port Engineer

Ir. drs. Boersen, S.
Royal HaskoningDHV
Rivers & Coasts
Hydraulic & Coastal Engineer

Preface

This research marks the last stage of the master in Civil Engineering at the Delft University of Technology, Faculty of Civil Engineering and Geosciences. It has been the last challenge in obtaining the title of Master of Science in the field of Hydraulic Engineering.

This thesis was carried out in collaboration with the Rivers & Coasts Department at Royal HaskoningDHV, which makes considerable efforts to create innovative design tools for coastal defences. In line with this ambition, Royal HaskoningDHV joined Boskalis Westminster, van Oord and Deltares in a Join Industry Project (JIP) named "JIP CoastalFOAM", which aims to contribute to the validation and expansion of a numerical model as design tool. I would like to thank Royal HaskoningDHV for the provided opportunity, resources and internal knowledge to perform this thesis at their offices in Rotterdam. I take this opportunity to express my gratitude to all the persons who had an impact on this final work.

My special thanks go to Alessandro Antonini for his constant and valuable guidance. His knowledge about the OpenFOAM package and numerical modelling was essential and highly appreciated. His input at every meeting and availability for discussion have substantially increased the quality of this research. Jeroen van den Bos' input, guidance and knowledge on rubble mound breakwaters and numerical modelling have helped me throughout the process. Always present at every progress meeting and willing to take the time to spar and discuss, which was greatly appreciated. I would like to thank Marion Tissier as well, for her precious feedback and time. Her contribution has certainly helped in increasing the quality of this report.

I would also like to express my deep gratitude to both my supervisors at Royal HaskoningDHV, Cock van der Lem and Stef Boersen. They have welcomed, introduced and guided me all along the way, offering me also the opportunity to attend my first scientific conference in Panama City, the 38th IAHR world congress with as theme "Water - Connecting the World". Their continuing assistance and feedback were essential.

Lastly, I would like to thank my family and friends for their personal support during these months. Without their encouragement it would not have been an enjoyable and instructive journey.

M.L.A. Moretto
Delft, February 17, 2020

Abstract

Worldwide, rubble mound breakwaters are designed and built to shelter and protect coastal areas from overtopping and flooding, especially harbours and shorelines. Rubble mound breakwaters are essential to preserve desired hydraulic conditions within the hinterland, avoiding damage to inhabited or industrial areas. This research focuses on the wave overtopping of rubble mound breakwaters as failure mechanism. To assess the wave overtopping engineers can adopt multiple methods. These methods can be ordered in increasing degree of accuracy and costs: empirical methods, neural networks, numerical models and physical laboratory experiments. The preliminary design phase is a highly iterative process. Using physical laboratory experiments within this phase is an expensive choice, therefore empirical methods are often preferred. Nevertheless, this research revealed that empirical methods, e.g. the so called EurOtop 2018, show significant shortcomings in assessing average overtopping quantities over rubble mound breakwaters, even more when the geometrical complexity of the structure increases (presence of protruding wave wall). This thesis re-calibrated the roughness coefficient proposed by the original EurOtop 2018 approach, referred to as the updated EurOtop 2018 method.

Numerical models are proposed as a possible solution between empirical methods (which can be carried out quickly given their low complexity) and physical laboratory experiments (which need more time but are characterised by high accuracy). They have been increasingly used and accepted in the past decades. Following this trend, the Joint Industry Project (JIP) CoastalFOAM [1] was launched with the objective to develop and validate a numerical model (OpenFOAM, waves2Foam, OceanWaves3D and JIP additions; referred to as CoastalFOAM) capable of accurately modelling the wave-structure interaction of rubble mound breakwaters. This research aims to calibrate and evaluate the CoastalFOAM model to assess small to large wave overtopping of rubble mound breakwaters with protruding or non-protruding wave wall, considering 500 waves. The evaluation of CoastalFOAM shows that this numerical model can be used, instead of empirical methods (e.g. updated EurOtop 2018), to assess the average overtopping discharges. CoastalFOAM showed excellent agreement with measurements for large and medium overtopping cases, while resulting less accurate for small overtopping cases.

The analysis revealed, however, that the average overtopping discharge as a quantity is not capable of identifying the magnitude of large overtopping events (without modelling all 500 waves). This can be considered critical in determining whether the structure is safe enough in terms of Serviceability Limit State (SLS) or Ultimate Limit State (ULS). Consequently, this thesis proposes a new methodology to assess the maximum overtopping volume within a storm, applying the concept of wave focusing and using the NewWave theory. The input variables for the NewWave profile are extracted from the spectral properties at the toe of the breakwater. A first order wave maker is used to generate the NewWave profile, making the methodology sensitive for the degree of non-linearity of the considered wave conditions. This NewWave methodology offers improved accuracy to assess the maximum overtopping volumes when compared to the EurOtop 2018 approach. Furthermore, this research proposes to apply the inverse EurOtop 2018 technique to assess the average overtopping discharge using the NewWave maximum overtopping volume. However, the accuracy of this methodology is lower than that obtained with the updated EurOtop 2018 guidelines.

This study shows that CoastalFOAM can be used, instead of the current empirical methods, to assess the average overtopping discharge within the design cycle of rubble mound breakwaters. However, according to what has emerged, CoastalFOAM shows to be less accurate in calculating small overtopping discharges as opposed to medium and large. On the other hand, when considering the maximum overtopping volume as design criterion the proposed NewWave methodology showed to be the most efficient and accurate.

[1] The Joint Industry Project (JIP) CoastalFOAM was founded in 2015 by the following engineering companies: Royal HaskoningDHV, Boskalis Westminster, van Oord and Deltares.

Contents

Preface iii

Abstract v

List of Figures ix

List of Tables xv

1 Introduction 1
- 1.1 Importance of this research 1
- 1.2 Coastal structures 2
- 1.3 Numerical models 3
- 1.4 Problem definition and description 3
- 1.5 Research objective and questions 4
- 1.6 Research methodology 4

2 Physical experiments 7
- 2.1 Introduction 7
- 2.2 Geometry 7
- 2.3 Wave parameters 8
- 2.4 Validation cases 9

3 Empirical Methods 11
- 3.1 Introduction 11
- 3.2 Average overtopping formulas 11
- 3.3 Comparison 15
- 3.4 Provisional conclusions 17

4 Numerical Model 19
- 4.1 Introduction 19
- 4.2 Numerical framework 19
- 4.3 Mathematical model 20
- 4.4 Wave generation 23
- 4.5 Ventilated boundary 24
- 4.6 Overtopping 24
- 4.7 Numerical set-up 25

5 Model validation 27
- 5.1 Introduction 27
- 5.2 Calibration case and procedure 27
- 5.3 Calibration of numerical model 28
- 5.4 Evaluation of medium overtopping cases 35
- 5.5 Sensitivity analysis 39
- 5.6 Evaluation of large overtopping cases 42
- 5.7 Evaluation of small overtopping cases 44
- 5.8 Summary 46

6 Model application 49
- 6.1 Introduction 49
- 6.2 Importance of the maximum overtopping volume 49
- 6.3 Focused wave group 51
- 6.4 The NewWave theory 51
- 6.5 Application of the NewWave theory 53

6.6 Methodology to assess the maximum overtopping volume (V_{max}) 53
6.7 Methodology to assess the average overtopping discharge, q 64

7 Comparison with empirical methods **67**
7.1 Introduction 67
7.2 Comparison EurOtop 2018 with CoastalFOAM, q 67
7.3 Comparison EurOtop 2018 with NewWave methodologies 71
7.4 Provisional conclusions 75

8 Discussion, conclusions and further research **77**
8.1 Discussion 77
8.2 Conclusions 79
8.3 Recommendations 82

References **85**

A Appendix A **91**

B Appendix B **93**
B.1 Time lag 93
B.2 Amplification steering paddle. 93
B.3 OceanWaves3D coupling 95
B.4 Reflection structure 96

C Appendix C **101**
C.1 Spectrum fit 101
C.2 Composite Weibull distribution 102
C.3 NewWave profiles in OceanWaves3D 103
C.4 Filtering out the spurious waves. 104

D Appendix D **105**
D.1 Cumulative overtopping figures 105

List of Figures

1.1 Kansai Airport (JP), flooded during the passage of Typhoon Jebi 2018. Figure printed from Business Insider Nederland. 1

1.2 The structure and various tools of the current design process adopted by consultants and contractors to obtain a final design. Figure printed from Van den Bos et al. (2015). 2

1.3 Proposed research methodology, in eight steps. 5

2.1 Sketch representing the geometry of the rubble mound breakwater in the numerical and physical flume. The dimensions are given in meters. The water level is varied along the 54 cases and represented by T-codes: 0.70 m (T30*), 0.75 m (T20*) and 0.80 m (T10*). 7

2.2 Hydraulic and geometrical parameters used in this research. 8

2.3 (a) Reflection coefficient plotted against the prototype overtopping discharge for each T20* case. (b) Ursell number plotted against the prototype overtopping discharge for each T20* case. 9

3.1 Mean overtopping discharges for 54 physical laboratory experiments, including a comparison between physical laboratory measurements and the EurOtop 2018 guidelines (γ_f = 0.40). 16

3.2 Mean overtopping discharges for 54 physical laboratory experiments, including a comparison between physical laboratory measurements and the updated EurOtop 2018 guidelines (γ_f) = 0.53. 16

4.1 Sketch showing the nested OpenFOAM domain within the OceanWaves3D domain, dimensions reported in meters. 20

4.2 The numerical model OpenFOAM with the various additional packages (Waves2Foam, OceanWaves3D and JIP CoastalFOAM improvements) for ease of reference in this report globally referred to as "CoastalFOAM". 20

4.3 [NTS = not to scale] Sketch of the numerical wave flume: a) OceanWaves3D domain; b) OpenFOAM domain. Dimensions are given in meters 25

4.4 OpenFOAM mesh resolutions, from coarse to fine around wave wall (based on Jacobsen et al. (2018)). 26

5.1 Summary of parameters describing a non-protruding wave wall test sample with a medium prototype overtopping discharge. Red line showing where the modelled wave overtopping is captured above the protruding wave wall. Note that the water level and structure levels are given relative to the bottom of the flume. The bottom of the flume is not shown. 28

5.2 (a) Surface elevation captured at wave gauge closest to structure (No. 5), x = 40.10 m, showing the discrepancy in the modelled surface elevation (extreme event) compared to measurements. (b) Comparison between modelled and measured surface elevation spectra, over 500 waves. 28

5.3 Cumulative overtopping results for a non-protruding wave wall and medium overtopping, including a comparison between: physical laboratory measurements and the initial model (B1). Figure based on Boersen et al. (2019). 29

5.4 Modelled (A1) surface elevation captured at wave gauge (No. 5), x = 40.10 m. Upper plot: no time lag is experienced at 125 s. Middle plot: T_{lag} = 0.85 s is found at 415 s. Lower plot: the lag is enhanced as the simulation is carried further, around 865 s the lag T_{lag} equals 1.72 s. 30

5.5 (a) Incoming surface elevation captured at wave gauge (No. 5), showing the discrepancy in the modelled (A2) surface elevation (extreme event) compared to measurements. (b) Comparison between modelled (A2) and measured incoming surface elevation spectra, over 300 waves. 31
5.6 (a) Incoming surface elevation captured at wave gauge closest to structure (5), x = 40.10 m, showing the improved (A4) modelled wave conditions. (b) Comparison between modelled (A4) and measured incoming surface elevation spectra, over 300 waves. . . . 31
5.7 Cumulative overtopping results for a non-protruding wave wall and medium overtopping, including a comparison between: physical laboratory measurements, the improved numerical model (A5) and the initial model (B1) set-up. 35
5.8 Summary of parameters describing a protruding wave wall test sample with a medium prototype overtopping discharge. Red line showing where the modelled wave overtopping is captured above the protruding wave wall. 35
5.9 Cumulative overtopping results for a protruding wave wall and medium overtopping, including a comparison between: physical laboratory measurements and the improved numerical model (A5). 36
5.10 Cumulative measured overtopping results for a non-protruding wave wall and medium overtopping, showing the six considered individual overtopping events. 37
5.11 Four different batches were used to construct the core of the breakwater in the physical flume. All four sieve curves are plotted against each other. The gradings (D_{n50}) and porosities (n) of batches 1, 4 and average are modelled in OpenFOAM. 39
5.12 Cumulative overtopping results for a non-protruding wave wall and medium overtopping, including a comparison between three numerical model runs (batch 1, batch 4 and batch average) with varying core characteristics (D_{n50} and n). 39
5.13 Cumulative overtopping results for a non-protruding wave wall and medium overtopping, including a comparison between four numerical model runs with varying porous flow coefficients (α and β) and KC). 40
5.14 Cumulative overtopping results for a protruding wave wall and medium overtopping, including a comparison between two numerical model runs with varying degree of openness of wave wall (0.5% and 3% degree of openness). 41
5.15 Cumulative overtopping results for a protruding wave wall and small overtopping, including a comparison between: the improved numerical model (A5) and the improved numerical model with an increased resolution (3x) in the overtopping region and measurements. 41
5.16 Summary of parameters describing a non-protruding wave wall test sample with a large prototype overtopping discharge. Red line showing where the modelled wave overtopping is captured above the non-protruding wave wall. 42
5.17 Cumulative overtopping results for a non-protruding wave wall and large overtopping, including a comparison between: physical laboratory measurements and the improved numerical model (A5). 42
5.18 Summary of parameters describing a protruding wave wall test sample with a large prototype overtopping discharge. Red line showing where the modelled wave overtopping is captured above the protruding wave wall. 43
5.19 Cumulative overtopping results for a protruding wave wall and large overtopping, including a comparison between: physical laboratory measurements and the improved numerical model (A5). 43
5.20 Summary of parameters describing a non-protruding test sample with a small prototype overtopping discharge. Red line showing where the modelled wave overtopping is captured above the non-protruding wave wall. 44
5.21 Cumulative overtopping results for a non-protruding wave wall and small overtopping, including a comparison between: physical laboratory measurements and the improved numerical model (A5). 44
5.22 Summary of parameters describing a protruding test sample with a small prototype overtopping discharge. Red line showing where the modelled wave overtopping is captured above the protruding wave wall. 45

5.23 Cumulative overtopping results for a protruding wave wall and small overtopping, including a comparison between: physical laboratory measurements and the improved numerical model (A5). . . . 45
5.24 Mean overtopping discharge for non-protruding wave wall cases in terms of relative overtopping rate and relative freeboard, including a comparison between: physical laboratory measurements, the improved numerical model (CoastalFOAM). . . . 46
5.25 Mean overtopping discharge for protruding wave wall cases in terms of relative overtopping rate and relative freeboard, including a comparison between: physical laboratory measurements and CoastalFOAM. . . . 47

6.1 Maximum volumes plotted against the average discharges for the respective cases, 27 protruding wave wall cases and 27 non-protruding wave wall cases. . . . 50
6.2 Technique to estimate the maximum overtopped volume from the measured cumulative overtopping curves. . . . 50
6.3 Process to achieve the desired NewWave profile at focus location, including: the NewWave theory to compute the NewWave profile at focus location, the linear wave theory to transform the NewWave profile to the paddle and a first order wave generation to produce the necessary steering file. . . . 53
6.4 Flowchart representing the followed methodology in order to obtain $V_{max,NewWave}$ for each case which is compared to $V_{max,measured}$. Red colour representing MATLAB procedures, yellow numerical modelling in CoastalFOAM, purple measurements and gray input parameters for the NewWave model. . . . 54
6.5 (a) Showing two possible spectrum fits applied to the incoming wave spectrum, where the JONSWAP ($\gamma = 3.3$) showed a good comparison with the measured incoming spectrum. Grey lines showing the threshold cut-off limits f_{LC} and f_{HC}. (b) Location where the incoming measured wave spectrum was captured (wave gauge 5). . . . 55
6.6 Comparison between two possible NewWave events depending on which enhancement factor (γ) is used and where the Pierson Moskowits NewWave profile shows an improved capacity of focusing compared to the JONSWAP NewWave profile. . . . 55
6.7 Composite Weibull exceedance curve for incoming wave heights considering case T205, showing a Rayleigh distribution (red line) until the threshold wave height and from there a Weibull distribution (red dotted line). . . . 56
6.8 Comparing the most non-linear NewWave focused wave group (a, b) with the least non-linear NewWave focused wave group (c, d), where the spurious waves gain in magnitude for increasing non-linear character. . . . 58
6.9 A comparison for case T203 (a) and T207 (b) between the NewWave profile containing the low frequency error wave (black line) and the NewWave profile where the low frequency wave is filtered out (red dotted line). . . . 59
6.10 (a) Comparison between CoastalFOAM and OceanWaves3D surface elevation time series for a non-protruding wave wall case, where the difference is induced by the reflection of the rubble mound breakwater. (b) The location at which the comparison is made. (c) The instantaneous overtopping discharge caused by the NewWave. (d) The location at which the overtopping discharge is captured. . . . 60
6.11 (a) Comparison between $\eta_{0.1\%,theory}$, $\eta_{max,OCW3D}$ and $\eta_{0.1\%,OF,in}$ for the nine non-protruding cases at focus location. (b) Range in which focusing of the incoming NewWave occurs. 61
6.12 Figure on the left showing the various locations at which focusing is forced, for a non-protruding wave wall case (A3W1T205), and how the overtopping volume varies along these locations. Table 6.2 showing the exact results. . . . 61
6.13 Maximum overtopping volumes, including a comparison between the NewWave approach and measurements. (a) For non-protruding wave wall cases. (b) For protruding wave wall cases. . . . 62
6.14 The maximum overtopping volume plotted against the Ursell number, including a comparison between: the NewWave methodology and the measurements for non-protruding wave wall cases. . . . 63

6.15 The maximum overtopping volume plotted against the Ursell number, including a comparison between: the NewWave methodology and the measurements for protruding wave wall cases. 63
6.16 Mean overtopping discharge for non-protruding wave wall cases in terms of relative overtopping rate and relative freeboard, including a comparison between: physical laboratory measurements and the NewWave single event approach using the updated roughness (γ_f = 0.53). 65
6.17 Mean overtopping discharge for protruding wave wall cases in terms of relative overtopping rate and relative freeboard, including a comparison between: physical laboratory measurements and the NewWave single event approach using the updated roughness (γ_f = 0.53). 65

7.1 Mean overtopping discharge for non-protruding wave wall cases in terms of relative overtopping rate and relative freeboard, including a comparison between: physical laboratory measurements, the improved numerical model (CoastalFOAM) and the updated EurOtop 2018 guidelines. 68
7.2 Mean overtopping discharge for protruding wave wall cases in terms of relative overtopping rate and relative freeboard, including a comparison between: physical laboratory measurements, the improved numerical model (CoastalFOAM) and the updated EurOtop 2018 guidelines. 69
7.3 Schematization of methods considered in the present research to assess q, where a distinction is made based on the availability of physical experiments. The accuracy of each method is given in function of RMSE values and measured average overtopping discharges, light blue boxes are for protruding wave wall cases and yellow for non-protruding wave wall cases. 70
7.4 Maximum overtopping volumes, including a comparison between three different methods and measurements: NewWave, EurOtop 2018 (γ_f = 0.40) and EurOtop 2018 (γ_f = 0.53); (a) for non-protruding wave wall cases; (b) for protruding wave wall cases. 71
7.5 The maximum overtopping volume plotted against the Ursell number, including a comparison between: the NewWave methodology, the updated EurOtop 2018 approach and the measurements for non-protruding wave wall cases. 72
7.6 The maximum overtopping volume plotted against the Ursell number, including a comparison between: the NewWave methodology, the updated EurOtop 2018 approach and the measurements for protruding wave wall cases. 72
7.7 Mean overtopping discharge for non-protruding wave wall cases in terms of relative overtopping rate and relative freeboard, including a comparison between: physical laboratory measurements, the NewWave single event methodology and the EurOtop 2018 guideline (using the updated roughness). 73
7.8 Mean overtopping discharge for protruding wave wall cases in terms of relative overtopping rate and relative freeboard, including a comparison between: physical laboratory measurements, the NewWave single event methodology and the EurOtop 2018 guideline (using the updated roughness). 74

8.1 Recommended methodology to follow at start of the design of a rubble mound breakwater when CoastalFOAM is to be used to assess the amount of wave overtopping. . . 82
8.2 In the event that physical laboratory experiments are to be performed the present research recommends to carry out steps 1 to 7 and collect the best possible data to calibrate the numerical model. 83

B.1 Incoming modelled and measured spectra at wave gauge closest to structure (5), x = 40.10 m. Showing that the amplification performed in this research performs better in terms of spectral wave height comparison with measurements. 94
B.2 Incident surface elevation captured at wave gauge closest to structure (No. 5), x = 40.10 m, showing the the discrepancies in modelling the incident surface elevations (extreme waves) when OceanWaves3D is coupled to OpenFOAM. 95
B.3 Incident surface elevation captured at wave gauge closest to structure (No. 5), x = 40.10 m, showing the improvement in coupling when adopting the proposed solution. . 95

B.4 Measured sieving curve of the armour layer in the physical flume. 98
B.5 Measured sieving curve of the filter layer in the physical flume. 98
B.6 Measured sieving curve of the core in the physical flume. Four different batches were used to construct the core of the breakwater in the physical flume. All four sieve curves are plotted against each other. 98
B.7 The α dimensionless resistance coefficient plotted against the β dimensionless resistance coefficients. Contours of the error between simulated and experimental surface elevations, using a set of dimensionless resistance coefficients, for different flow regimes (characterised by the porous Reynolds number (Re_p)). 99

C.1 Showing two possible spectrum fits applied to the incoming wave spectrum. Where the JONSWAP (γ = 3.3) showed a good comparison with the measured incoming spectrum. Grey lines showing the threshold cut-off limits f_{LC} and f_{HC}. Cases T201 to T209 without T205. 101
C.2 Composite Weibull exceedance curve for incoming wave heights considering cases T201 to T209 without T205, showing a Rayleigh distribution (red) until the threshold wave height and from there a Weibull distribution (red dotted line). 102
C.3 Incident surface elevation measured at focusing point, including a comparison between: the OceanWaves3D model generated surface elevation using a first-order wave generation and the theoretical NewWave profile according to NewWave theory, for cases T201 to T209 without T203 and T207. 103
C.4 A comparison between the NewWave profile containing the low frequency error wave (black line) and the NewWave profile where the low frequency wave is filtered out (red dotted line), showing the induced set-up in front of the incident NewWave profile for highly non-linear cases such as T206 for example. Cases T201-T209 are shown except T203 and T207. 104

D.1 Cumulative overtopping results for a large overtopping discharge for (a) a non-protruding wave wall and (b) a protruding wave wall, including a comparison between: physical laboratory measurements, the improved numerical model and the updated EurOtop 2018 guideline. 105
D.2 Cumulative overtopping results for a medium overtopping discharge for (a) a non-protruding wave wall and (b) a protruding wave wall, including a comparison between: physical laboratory measurements, the improved numerical model and the updated EurOtop 2018 guideline. 105
D.3 Cumulative overtopping results for a small overtopping discharge for (a) a non-protruding wave wall and (b) a protruding wave wall, including a comparison between: physical laboratory measurements, the improved numerical model and the updated EurOtop 2018 guideline. 106

List of Tables

2.1 Ranges of hydraulic and geometrical boundary conditions in which the 54 test samples lie. 9

3.1 CLASH data base ranges for which the roughness coefficient (double rock layer) was re-calibrated. 13
3.2 Parameters reported in Molines and Medina (2016) to compute the dimensionless overtopping discharge. 14
3.3 Input parameters for the previous empirical methods. 15
3.4 Root mean squared errors compared to measurements, including a comparison between: the EurOtop 2018, the Neural Network and Molines and Medina 2016. The mean measured average overtopping discharges over the respective 27 cases (non-protruding or protruding) are reported to interpret the magnitude of the reported errors (RMSE). . . 17

5.1 Summary of parameters describing a non-protruding wave wall test sample with a medium prototype overtopping discharge. 28
5.2 Statistical and spectral parameters (RMSE, PCC and H_{m0}) describing the quality of the wave conditions at wave gauge 5, including a comparison between: the original and improved numerical model (A2 and A4) in terms of total, incoming and reflected wave conditions. 32
5.3 Multiple sets of dimensionless resistance coefficients used in the parametrisation of van Gent (1995), showing that the desired bulk reflection can be obtained using different sets of coefficients. 34
5.4 Statistical and spectral parameters (RMSE, PCC and H_{m0}) describing the quality of the wave conditions at wave gauge 5, including a comparison between: the numerical model (A2, A4 and A5) in terms of total, incoming and reflected wave conditions. 34
5.5 Summary of parameters describing a protruding wave wall test sample with a medium prototype overtopping discharge. 35
5.6 Statistical and spectral parameters (RMSE, PCC and H_{m0}) describing the quality of the wave conditions at wave gauge 5, including a comparison between: the improved numerical model (A5) in terms of total, incoming and reflected wave conditions. 36
5.7 Individual overtopping volumes (O1-O6) for the non-protruding wave wall with medium prototype overtopping case, including a comparison between: the measurements, the initial model (B1) and the improved model (A5) set-up. 38
5.8 Individual overtopping volumes (O1-O6) for the protruding wave wall with medium prototype overtopping case, including a comparison between: the measurements and the improved model (A5) set-up. 38
5.9 Summary of parameters describing a non-protruding wave wall test sample with a large prototype overtopping discharge. 42
5.10 Statistical and spectral parameters (RMSE, PCC and H_{m0}) describing the quality of the wave conditions following the proposed validation process, for a non-protruding test sample with a large prototype overtopping discharge. 42
5.11 Summary of parameters describing a protruding wave wall test sample with a large prototype overtopping discharge. 43
5.12 Statistical and spectral parameters (RMSE, PCC and H_{m0}) describing the quality of the wave conditions following the proposed validation process, for a protruding test sample with a large prototype overtopping discharge. 43
5.13 Summary of parameters describing a non-protruding wave wall test sample with a small prototype overtopping discharge. 44

5.14 Statistical and spectral parameters (RMSE, PCC and H_{m0}) describing the quality of the wave conditions following the proposed validation process, for a non-protruding test sample with a small prototype overtopping discharge. 44
5.15 Summary of parameters describing a protruding wave wall test sample with a small prototype overtopping discharge. 45
5.16 Statistical and spectral parameters (RMSE, PCC and H_{m0}) describing the quality of the wave conditions following the proposed validation process, for a protruding test sample with a small prototype overtopping discharge. 45
5.17 Measured average discharges and RMSE values when applying the uncalibrated model or CoastalFOAM for the estimation of the average overtopping discharge q, including a separation between protruding and non-protruding wave wall cases. 47

6.1 Spectral properties of the incoming measured/physical wave conditions for all considered cases. Based on the spectral wave height H_{m0}, the $H_{0.1\%}$ is found according to Battjes and Groenendijk (1999) used to construct the Composite Weibull distribution from which $\eta_{0.1\%}$ is derived and compared to the maximum $\eta_{measured}$ experienced during measurements. Additionally, for each case a degree of non-linearity has been given in terms of the Ursell number. 57
6.2 The overtopping volumes given for each focus location around the toe of the breakwater, considering a non-protruding wave wall case (A3W1T205). 61
6.3 Maximum overtopping volumes, including a comparison between the NewWave methodology and measured maximum overtopping volumes for protruding and non-protruding wave wall cases. The Ursell number describes the degree of non-linearity for each case. 63
6.4 RMSE values when comparing both NewWave approaches (original and updated roughness) with measurements, for non-protruding and protruding wave wall cases. In addition, the measured average discharges of the respective cases are given against which the RMSE values can be evaluated. 64

7.1 RMSE values of three proposed methods for the estimation of the average overtopping discharge q, including a separation between: protruding, non-protruding wave wall and overall. 68
7.2 Maximum overtopping volumes, including a comparison between the NewWave, the corrected EurOtop 2018 method and measured maximum overtopping volumes for protruding and non-protruding wave wall cases. The Ursell number describes the degree of non-linearity for each case. 71
7.3 RMSE and error values of two proposed methods for the estimation of maximum overtopping volume. 72
7.4 Reported errors when using the various methodologies to compute q compared to the measured average overtopping discharges. 74

8.1 Recommended mesh properties concerning the wave propagation in both numerical domains, according to the present research. 82

A.1 Hydraulic boundary conditions for all 54 experimental cases. First half containing cases with protruding wave wall, defined by the A1 code. The bottom half containing the cases without protruding wave wall element with code A3. The water depth is described by the T-code, where cases containing T1 are for a water depths of 0.80 m, T2 for 0.75 m and T3 for 0.70 m. 91

B.1 Statistical and spectral parameters describing the relation between the various OCW3D configurations. 95
B.2 Grading parameters for different subdivisions of the rubble mound breakwater, on laboratory and prototype scale. 96

1
Introduction

1.1. Importance of this research

In 2018, Typhoon Jebi passed through the Kansai region in Japan (JP) which flooded Kansai International Airport, as shown in Figure 1.1. A combination of land subsidence, storm surge and high tide resulted in overtopping of the sea defences. The Kansai region contributes for 19% (939$ billion) of the GDP of Japan, where the airport plays a key role receiving over 25 million passengers every year. The recorded economical damage was estimated around 66.4 million Euros (Kansai Airport, 2019). Ports situated at the coast or offshore are prone to increasing hydraulic conditions (sea level, waves, etc.). Nowadays, cargo transport (for inland or transfer purposes) processed and transmitted through seaports accounts for a noteworthy slice of the gross domestic product (GDP) of the hosting country. The Port of Rotterdam creates 384,500 jobs and is responsible for an added value (direct or indirect) of 45.6 billion euros, equal to 6.2% of the GDP of The Netherlands. The Port of Rotterdam is the largest port in Europe with a throughput of 469 million tonnes and lists in the top 10 seaports on global scale (10th) (Port of Rotterdam, 2018). The presented numbers demonstrate the importance of these ports in the current economy, clarifying the need for hydraulic structures to protect them against occurring risks. Given the economic importance, the consequences of damaging or disrupting the port activities are high and therefore the acceptable probability low. Ensuring a tolerable risk is achieved by setting strict safety standards (low probabilities of failure). The latter are continuously monitored and re-assessed to ensure that the port activities are well protected. Even more now, since current extreme wave conditions, used as design conditions for coastal defences, will occur more frequently caused by various climate change scenarios (Chini and Stansby, 2012). When the latter is considered in combination with the ageing of coastal defences and the ongoing growth of present ports, it leads to a high demand for the re-assessment of coastal defences. Considering this, consultants develop new efficient methods to cover this upcoming demand.

Figure 1.1: Kansai Airport (JP), flooded during the passage of Typhoon Jebi 2018. Figure printed from Business Insider Nederland.

1.2. Coastal structures

Coastal structures, e.g. breakwaters and revetments, find their main use in sheltering and protecting the hinterland. For instance, in case of seaports, breakwaters are used to reduce the incoming wave conditions. So that, within the harbour, no loss of loading/unloading time is encountered as it would lead to economic damage. Different type of breakwaters exist, for example: submerged, emerged, vertical or floating. The choice between the various types depends on various parameters, e.g. site conditions, hydraulic boundary conditions and material/labour costs. A frequently encountered breakwater type is the Conventional Multi-layered rubble mound BreakWater (CMBW) with a superstructure, referred to as wave wall, placed on top. The former typically mainly consists of a porous core made out of rock. On top of the core, protective layers (filter layers) are placed avoiding internal erosion. The armour layer, i.e. most external layer, is dimensioned to withstand the incoming waves and currents protecting both the filter layer and the core. The stability of the rocks placed on the exposed slope depends on the ratio between load and strength, i.e. wave height versus rock size and the relative density of the elements (Verhagen and Van den Bos, 2018). Multiple failure mechanisms exist for rubble mound breakwaters, e.g. damage to the armour layer which exposes the filter and the core, toe erosion, wave overtopping, slip circle and wave wall instabilities.

1.2.1. Wave overtopping

Wave overtopping is defined as the passing of water over the crest of a rubble mound breakwater due to excessive wave run-up. Wave overtopping is one of the aforementioned failure mechanisms and will be studied more closely during this research. Extreme wave overtopping over coastal defences could lead to coastal flooding which may cause significant damage to domestic and industrial infrastructure (see Figure 1.1). In addition, it may threaten life in vulnerable coastal communities, particularly where residents are unaware of the risks posed by overtopping (Allsop et al., 2003). In current practice, average overtopping discharges over breakwaters and coastal revetments are key elements in determining the required crest elevation, berm or slope of these structures in order to reduce the overtopping amounts to acceptable levels. Due to increased loads caused by global warming and lowering of the resistance owed to the ageing of coastal defences (Geeraerts et al., 2007), these acceptable levels are often exceeded. This leads to re-evaluating current and recommend new designs where needed. Designing new coastal defences can be done using multiple methods, ordered in increasing degree of accuracy and costs: empirical methods, neural networks, numerical models and physical laboratory experiments.

1.2.2. Design process

The current design process for rubble mound breakwaters can be schematized as shown in Figure 1.2. The choice of the combination between the visualized tools will depend on multiple factors, e.g. on the complexity of the structure, the available time and budget. The design formulas, upper part in Figure 1.2, are usually semi-empirical methods that are themselves based on physical model tests or field measurements. Using these formulas outside their validity ranges, which is frequently encountered during a design process as the complexity of the design increases, introduces errors. On the left hand side the physical laboratory experiments are schematized. These are widely used to test, adapt and re-evaluate produced designs, reducing the inaccuracy of the applied empirical formulas. Within Royal HaskoningDHV, in case of rubble mound breakwaters, roughly 70% of the physical laboratory experiments evaluate wave overtopping quantities, showing how important consultants and contractors esteem the accurate assessment of wave overtopping. However, physical laboratory experiments, apart from being accurate, are significantly

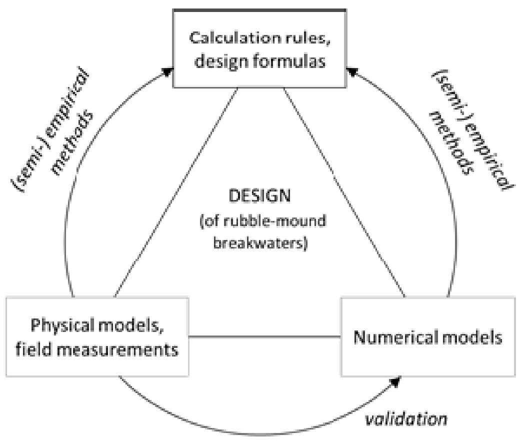

Figure 1.2: The structure and various tools of the current design process adopted by consultants and contractors to obtain a final design. Figure printed from Van den Bos et al. (2015).

more expensive than their alternatives. Consequently, the right hand side was introduced as an alternative solution. Over the past decade notable research progress has been made in the capabilities of numerical models, making these suitable for design purposes. Numerical models are introduced and applied as a way between empirical formulas and physical model tests, considering accuracy and costs. Nonetheless, numerical models are only worthwhile if the results can be trusted, i.e. the numerical model is sufficiently accurate to represent the process at hand.

1.3. Numerical models

Various numerical model types exist and are used to simulate wave-structure interactions which fall under Computational Fluid Dynamics (CFD) models. These numerical models may be separated in two main categories: the nonlinear shallow water equations models (NLSW) and the Navier Stokes equations models (NS). The Navier-Stokes (NS) differential equations represent the most complete flow description in three dimensions. Solving for pressure, the three dimensional flow velocity components in time and space using numerical methods makes them computationally expensive compared to other models. Nowadays, a frequently used form of the Navier-Stokes differential equations are the Reynolds-Averaged Navier-Stokes equations (RANS) with resistance terms (due to presence of breakwater skeleton) combined with the volume of fluid method (VOF). RANS codes have already been developed and validated for a wide range of coastal engineering applications (e.g. overtopping, wave loads, armour stability, toe stability, wave-structure interaction etc.). Multiple CFD codes applying RANS are found in the community to model coastal processes: IH-3VOF (Lara et al., 2012a,b), COBRAS (Hsu et al., 2002; Lin and Karunarathna, 2007), IHFOAM (Higuera et al., 2013, 2014a,b), OpenFoam (Jensen et al., 2014; Higuera et al., 2014a). The latter, provided as open source tool and accessible at both the TU Delft and Royal HaskoningDHV, will be used during this research.

1.4. Problem definition and description

Currently, empirical methods, e.g. EurOtop 2018 (Van der Meer et al., 2018), are used for the assessment of average overtopping discharges either in a deterministic way or in a probabilistic way. However, when designing complex geometrical structures, often the derived formulas are applied outside their range of validity, introducing significant errors. Instead, physical laboratory experiments are used, which apart from being more accurate are significantly more expensive than their alternatives. Therefore, numerical models are suggested to replace the aforementioned applications.

Numerical modelling of wave overtopping has already been validated for different situations (vertical seawalls, vertical breakwaters, impermeable dikes, rubble mound breakwaters etc.) (Losada et al., 2008; Jensen et al., 2014; Karagiannis et al., 2015; Castellino et al., 2018). A first attempt to validate the average overtopping discharges over rubble mound breakwaters with a wave wall on top, using the numerical package proposed by Jacobsen et al. (2018), was done in Boersen et al. (2019). Nevertheless, Boersen et al. (2019) adopted a non-calibrated model which showed discrepancies in terms of modelled surface elevations. The quality of the incident and reflected wave conditions together with the reflection of the structure were not addressed. Consequently, the aim of the present research is to widen the applicability of the numerical model (recommended by Jacobsen et al. (2018); capable of modelling forces on the wave wall), through presenting a systematic validation considering the wave overtopping of a rubble mound breakwater and its basic hydraulic parameters: incoming waves, reflected waves and the bulk reflection of the structure.

Numerical models are gaining importance as engineering design tool, as a result of a wide range of validation studies which were done over the past years and which still continue. However, an important set-back is computational time. Applying the numerical model as design tool requires multiple simulations to find the optimal design iteratively and therefore a high amount of computational time. To reduce the computational time the present research proposes a different approach to the current design methods. Instead of designing based on average overtopping discharges, extreme events will be considered. Van der Meer et al. (2018) mentions a trend towards replacing average overtopping discharges with maximum overtopped volumes for design purposes. This approach follows from the idea that storms containing one extreme event could result in similar average overtopping discharges as storms with multiple small events. However, the first storm could result in more damage and this can not be captured from just looking at average overtopping discharges. Accordingly, a method applying the concept of wave focusing will be proposed in the presented research to simulate isolated overtopping events caused by extreme wave events. This method will be validated by comparing the modelled volumes with the volumes obtained from full time series measurements.

1.5. Research objective and questions

This research should give insight on the capability of the numerical model to simulate the average overtopping discharges and maximum overtopping volumes over rubble mound breakwaters with or without protruding wave wall placed on top. At the same time, it should give more insight on the sensitivities of different used input parameters on the wave conditions in front of the structure and consequently on the average/extreme overtopping discharges over the considered structure. Furthermore, it should consider the trade-off between accuracy and time consumption, by comparing full measured time series extreme events against modelled isolated extreme events. This different design approach is validated for rubble mound breakwaters, but expectedly can be extended to consider other coastal structures. All this can be summarised in the following research objective:

> ”Demonstrate that CFD (Computational Fluid Dynamics) can be applied to accurately and efficiently simulate two-dimensional overtopping of rubble mound breakwaters, in terms of average overtopping discharges and individual overtopping volumes.”

The following sub-research questions are extracted from the main research objective:

1. Which methods do exist and to what extent are they able to accurately assess average overtopping quantities over rubble mound breakwaters with protruding and non-protruding wave wall?

2. Can the proposed numerical model accurately capture small to large average overtopping discharges whilst considering 500 incident waves, replacing empirical methods in the preliminary design stages of rubble mound breakwaters?

3. Can a methodology be developed which accurately captures the maximum overtopping volume and average overtopping discharge by modelling only a couple of incident waves, therefore reducing computational time?

1.6. Research methodology

A methodology is proposed in order to answer the main research objective and sub-questions in a structured way (see Figure 1.3). The eight considered steps are the respective chapters of this thesis.

- Chapter 1 introduces the importance of this work, the problem definition, the research objective and main questions, as well as its scope and methodology. A literature study is carried out on: numerical modelling, computational fluid dynamics, RANS-VOF models, design methods considering average discharges or maximum overtopped volumes and rubble mound breakwaters.

- The physical laboratory experiments used for the calibration and validation of the numerical model are explained in Chapter 2.

- In Chapter 3 multiple empirical methods are elaborated and compared with measured outcomes. The shortcomings (if any) of state of the art empirical formulas are highlighted. The most accurate empirical method is selected and will be compared with numerical outcomes.

- Chapter 4 describes the adopted numerical model; framework, theoretical aspects, mathematical equations, coupling and set-up of the numerical model.

- In Chapter 5 a calibration procedure is carried out in which various aspects are analysed: surface elevations, the coupling between adopted numerical models, the induced reflection by the breakwater, the instant and cumulative overtopping curves and concluded by a sensitivity analysis. The calibrated model is than used to validate small and large overtopping cases.

- At this point, the research shifts from average overtopping discharges towards individual overtopping volumes. In Chapter 6 the numerical model is applied to simulate extreme overtopping events. Two methodologies are presented to efficiently assess the maximum overtopping volume and the average overtopping discharge given the wave conditions at the toe of the breakwater.
- Chapter 7 compares the numerical model outcomes from Chapters 5 and 6 with the selected empirical methods from Chapter 3, demonstrating if the numerical model shows improved accuracy compared to the considered empirical methods.
- Finally, in Chapter 8 the results are discussed, a conclusion is formulated regarding the outcomes of this study and recommendations for future research are given.

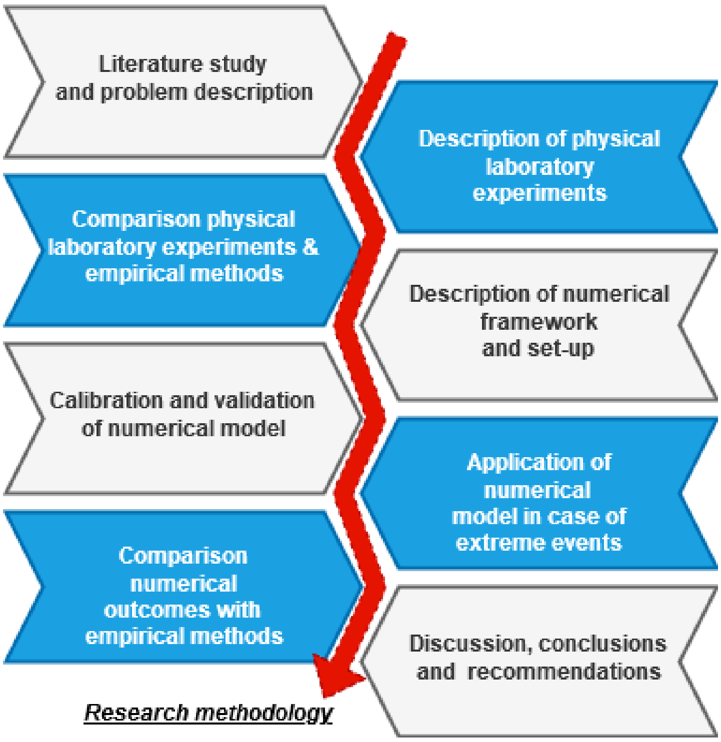

Figure 1.3: Proposed research methodology, in eight steps.

2
Physical experiments

2.1. Introduction

Over the past decade numerical modelling has often been used within the design process of coastal structures. Following this upcoming trend, the Joint Industry Project (JIP) CoastalFOAM was founded by the following engineering companies: Royal HaskoningDHV, Boskalis Westminster, van Oord and Deltares. The goal of the JIP was to develop and validate a numerical model (OpenFOAM/waves2Foam) capable of accurately modelling the wave-structure interaction of permeable structures (e.g. rubble mound breakwaters). The model was validated by van Gent et al. (2017) for the design of open filters in case of rubble mound breakwaters. More recently, Jacobsen et al. (2018) used the numerical model to validate forces on protruding wave wall elements. In this chapter the physical experiments used by Jacobsen et al. (2018) for the validation of forces acting on protruding wave wall are described. Conducted in the Scheldt flume at Deltares and provided within the JIP CoastalFOAM, these experiments will be used in the presented research for the validation of wave overtopping. Primarily, the geometry of the coastal structure, a double rock layered breakwater, is illustrated. Subsequently, for the 54 performed experimental cases the incoming wave climate parameters are provided. Further, a substantiated reason is given for selecting specific cases for the purpose of validating the wave overtopping using the numerical model.

2.2. Geometry

The physical geometry of the rubble mound breakwater is both used for the physical as well as for the numerical wave flume. A scale factor of 36 is used compared to prototype. The geometry of the hydraulic structure is shown in Figure 2.1. All dimensions are given in meters.

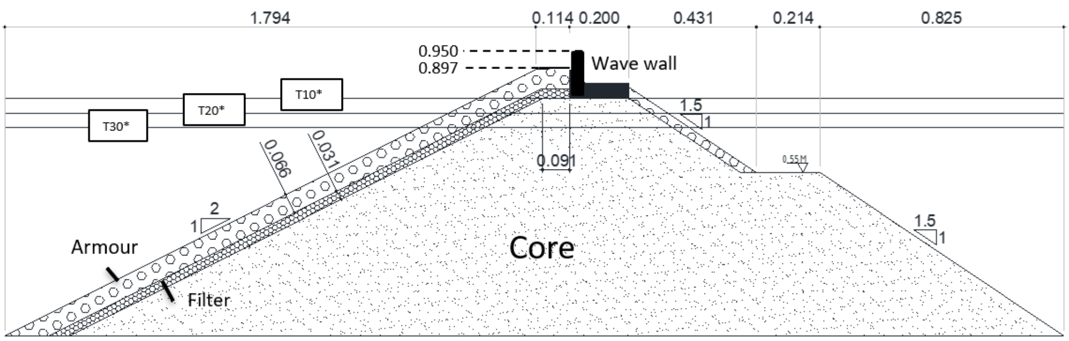

Figure 2.1: Sketch representing the geometry of the rubble mound breakwater in the numerical and physical flume. The dimensions are given in meters. The water level is varied along the 54 cases and represented by T-codes: 0.70 m (T30*), 0.75 m (T20*) and 0.80 m (T10*).

The structure is a breakwater with an armour layer protecting the under layer (filter) from wave impacts, which in turn covers the core. These layers are characterised by their rock grading curves. The median nominal diameter (D_{n50}) is the value for which 50% of the mass of the considered rock grading has passed (see Equation 2.1). For the core a D_{n50} of 0.007 m is chosen, which is covered by a filter layer with a D_{n50} value of 0.017 m. On top a double rock armour layer is placed with a D_{n50} of 0.036 m. The aforementioned numbers were used in Jacobsen et al. (2018) and will be re-assessed in the calibration part.

$$D_{n50} = (\frac{M_{50}}{\rho_{rock}})^{\frac{1}{3}} \tag{2.1}$$

Details concerning the length, height, layer thicknesses, width of the crest and slopes of the breakwater are given in Figure 2.1 in meters. Important to note is that for half of the performed cases the wave wall does not protrude the armour layer but reaches the same height (0.897 m from the bed), given the code A3 (for example A3W1T205). For the other half the wave wall protrudes the armour layer and reaches a height of 0.95 m from the bed, given the code A1. The Scheldt Flume at Deltares has a width of 1 m and a height of 1.2 m. The breakwater was placed 41.5 m from the wave paddle. The paddle is a piston-type wave paddle and is equipped with active reflection compensation. For validation purposes in the flume five wave gauges were placed at x_1 = 35.74 m, x_2 = 38.73, x_3 = 39.38 m, x_4 = 39.83 m, x_5 = 40.10 m to compare the experimental surface elevation with the numerical surface elevation. The overtopping was measured using an overtopping tray with a width of 0.2 m which collected the overtopping water. Additionally, during these experiments pressure sensors were placed on the wave wall, sensors which Jacobsen et al. (2018) used for the validation of forces acting on the protruding wave wall.

2.3. Wave parameters

In the 54 performed physical model tests several input parameters were varied, from wave conditions to geometries (protruding or non-protruding wave wall element). Each incoming surface elevation time series is characterised by its variance density spectrum ($E(f)$). The latter can be described by spectral moments using Equation 2.2.

$$m_n = \int_{\infty}^{0} f^n E(f) df \quad for \quad n = ..., -2, -1, 0, 1, 2, ... \tag{2.2}$$

Various spectral properties are used to describe wave spectra, e.g. the spectral wave height $H_{m0} = 4 \cdot \sqrt{m_0}$, where $m0$ is the zero order moment. In deep water the spectral wave height equals the significant wave height which is the average value of the highest one third of the waves. Furthermore, various spectral wave periods can be defined, e.g. the period containing the highest energy in the spectrum T_p or the average wave period $T_{m-1,0}$ defined as m_{-1}/m_0. The waves break as they interact with the rubble mound breakwater. The type of wave-breaking can be characterised by the Irribarren number, calculated using Equation 2.3, where $L_{m-1,0}$ is the spectral wave length in deep water using $T_{m-1,0}$. This number is computed for all 54 cases and ranged from 2.35-3.76 [-], labeled as non-breaking or surging waves.

$$\xi_{m-1,0} = \frac{tan(\alpha)}{\sqrt{H_{m0}/L_{m-1,0}}} \tag{2.3}$$

Properties such as R_c the wave wall freeboard, A_c the armour layer freeboard, G_c the width of the crest, $cot(\alpha)$ the front slope, h_t water depth above toe, h_t water depth and B_t the width of the berm are depicted in Figure 2.2.

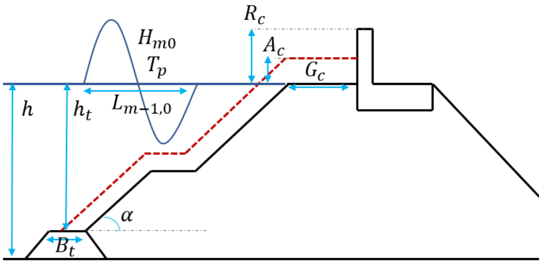

Figure 2.2: Hydraulic and geometrical parameters used in this research.

The ranges in which the hydraulic and geometrical boundary conditions lie for the 54 cases are listed in the following Table 2.1.

Armor type	No. Data	H_{m0} [m]	$T_{m-1,0}$ [s]	R_c [m]	A_c [m]	G_c [m]	$cot\alpha$	h_t [m]	h [m]	B_t [m]
Rock (2 L)	54	0.078–0.171	1.120–2.807	0.097–0.250	0.097–0.197	0.114	2	0.70-0.80	0.70–0.80	0.000

Table 2.1: Ranges of hydraulic and geometrical boundary conditions in which the 54 test samples lie.

As no berm and no toe were used in the physical flume, the toe depth (h_t) is equal to the water depth (h) and berm width (B_t) is zero. Table 2.1 will be used in Chapter 3 to show that the experiments lie within the ranges for which most empirical formulas are derived. The case specific hydraulic and geometrical boundary conditions are provided in Appendix A (see Table A.1).

2.4. Validation cases

It would be interesting to study all of the 54 provided test samples for the validation of the numerical model. Yet, the computational time it would require would be too large. Therefore, only six cases are investigated: three protruding wave wall cases and three non-protruding wave wall cases. The selection considered various aspects: the prototype overtopping discharges (q_{proto}), the reflection coefficients (K_r) and the degree of non-linearity of the incoming wave conditions (Ursell number). First, the selection contains cases with limited to no and significant prototype overtopping discharges (e.g. T204, T205 and T206). By doing this, a wide range of validation is created, showing the strength (or weakness) of the numerical model. All selected cases have a water depth of 0.75 m (T20*), so that the variability of the water depth on the bulk reflection is left for future validation works. The number of waves range from 1077 to 1250 to simulate a fully developed sea state. Second, as the bulk reflection of the structure is expected to influence overtopping quantities, cases with varying reflection coefficients are selected (so as T205 and T209). This is done to prove that the numerical model is able to correctly capture the varying bulk reflection of the rubble mound breakwater. The reflection coefficient is given by Equation 2.4.

$$K_r = \frac{H_{m0,r}}{H_{m0,i}} \tag{2.4}$$

Where $H_{m0,r}$ is the reflected spectral wave height and $H_{m0,i}$ the incoming spectral wave height. The reflection coefficient is plotted against the prototype overtopping discharge for all non-protruding wave wall cases with a water depth of 0.75 m, as shown in Figure 2.3a.

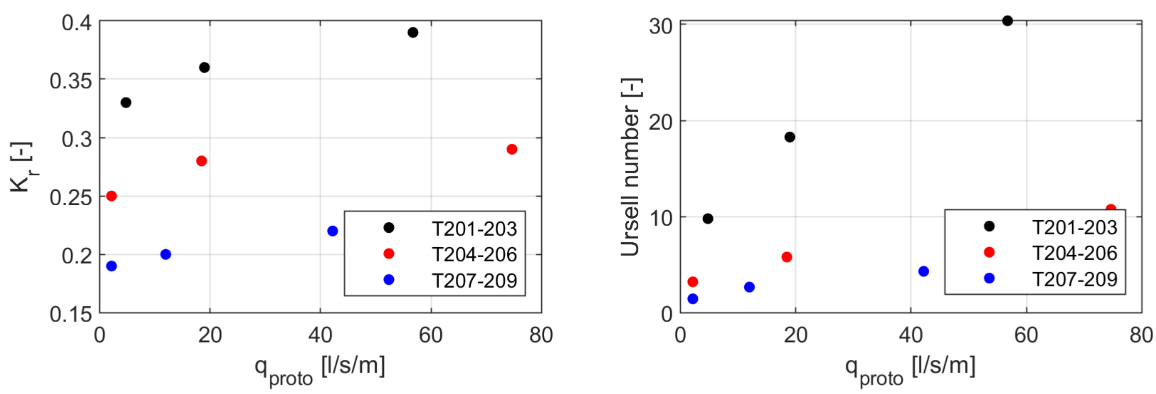

(a) Reflection coefficient.

(b) Ursell number.

Figure 2.3: (a) Reflection coefficient plotted against the prototype overtopping discharge for each T20* case. (b) Ursell number plotted against the prototype overtopping discharge for each T20* case.

Third, the non-linearity of the measured wave conditions is another important aspect to consider as waves are propagating in intermediate water (0.05 < h/L < 0.5) and interact with the porous structure. In the present research the Zelt and Skjelbreia (1992) technique with five wave gauges is used as reflection analysis method. This technique uses the linear wave theory (LWT). The higher the amount of wave gauges the more accurate the method becomes. As the technique is based on LWT, non-linearities are filtered out. The non-linearity of the incoming wave conditions can be characterised by the Ursell number ($H_{m0}L^2/h^3$), where an increase represents a higher degree of non-linearity. The Ursell number is plotted against the prototype overtopping discharge in Figure 2.3b. Cases T201-203 and T206 show the highest degree of non-linearity and are therefore not selected as precaution. Finally, considering all the above mentioned: small to large overtopping discharge, varying reflection coefficient and low degree of non-linearity cases T204, T205 and T209 are chosen, represented in bold in Appendix A (see Table A.1).

3

Empirical Methods

3.1. Introduction

This chapter introduces and deals with the first design technique, used at the beginning of the design cycle for coastal structures, i.e. the empirical approach. Firstly, a description is given of the various empirical formulas applicable for the design of a rubble mound breakwater considering failure due to average overtopping quantities. Explanations are provided when empirical methods are disregarded. Secondly, a method by Molines and Medina (2015) is introduced and applied to improve the state of the art methods. Finally, a comparison is given between the outcomes of the mentioned empirical methods and the physical laboratory experiments.

3.2. Average overtopping formulas

Currently the engineer is limited to past experiences, empirical overtopping design formulas or neural networks for the preliminary stages of a breakwater design. However, using empirical formulations outside their range of validity reduces their applicability, considerably increasing the error between measured and predicted values. In this chapter, several empirical overtopping formulas, applicable in case of rubble mound breakwaters with wave wall on top (protruding/non- protruding), will be compared with the available measurements. A short description of the empirical formulas, in chronological order, and their range of applicability will be given in the following paragraphs. It is not the scope of this research to assess all possible overtopping formulas that have been derived in past works for rubble mound breakwaters. Only the methods that are used nowadays within consultancy firms and at the TU Delft are reported here.

3.2.1. Rock Manual 2007

The Rock Manual (CIRIA et al., 2007a) recommends to use the TAW method (TAW, 2002) for the assessment of average overtopping quantities over a rough permeable slope. Two formulas were proposed (without berm on armoured slope): one for breaking waves ($\xi_{m-1,0} < \cong 2$), where wave overtopping increases for increasing breaker parameter; and one for non-breaking waves ($\xi_{m-1,0} > \cong 2$), where maximum overtopping is achieved. In this research non-breaking waves are studied. Therefore, the maximum overtopping formula will be used for comparison with experimental data, as shown in Equation 3.1.

$$\frac{q_{end}}{\sqrt{g \cdot H_{m0}^3}} = C \cdot exp\left[-D\frac{R_c}{H_{m0} \cdot \gamma_f \cdot \gamma_\beta}\right] \tag{3.1}$$

Where γ_f and γ_β are influence factors considering the roughness of the armoured slope and the obliquity of the incoming waves respectively. The Rock Manual uses the roughness influence factors which were derived by Pearson et al. (2004), for $\xi_{m-1,0} < \cong 2$. When $\xi_{m-1,0} > \cong 2$ the roughness factors are increased linearly up to 1 when $\xi_{m-1,0}$ reaches 10. Coefficients C and D were derived representing the average trend through the studied data set, and for the purpose of comparing the empirical method with experimental results values 0.20 and 2.30 were proposed. For the influence of the wave wall placed on top of the structure, the Bradbury et al. (1988) approach is proposed, where the dimensionless average overtopping discharge is obtained using Equations 3.2, 3.3 and 3.4.

$$F^* = \left(\frac{R_c}{H_s}\right)^2 \cdot \sqrt{\frac{s_{0m}}{2\pi}} \tag{3.2}$$

$$Q^* = a \cdot (F^*)^{-b} \tag{3.3}$$

$$q = Q^* \cdot T_m \cdot g \cdot H_s \tag{3.4}$$

Where, R_c is the free-board compared to SWL, H_s the significant wave height of the incoming waves (mean wave height of the highest one third of the waves), g the gravitational constant, s_{0m} the fictitious wave steepness (L_0/T_m) based on T_m (the mean wave period of the incoming waves) and L_0 (the deep water wave length using linear wave theory), Q^* dimensionless overtopping discharge and F^* a factor accounting for the presence of the wave wall. For the protruding cases Equation 3.2 will be used to compute the average overtopping discharges. Coefficients a and b are based on studies by Aminti and Franco (1988) and Bradbury et al. (1988) to account for the presence of the wave wall, and are found to be $1.7 \cdot 10^{-7}$ and 2.41 respectively. Moreover, the influence of the armoured crest width on top of the breakwater on the average overtopping discharge (protruding and non-protruding) has not been implemented directly in the Rock Manual 2007. It was improved in the EurOtop 2007 guidelines (see Section 3.2.2). As a consequence, the Rock Manual 2007 results are not listed in the comparison.

3.2.2. EurOtop 2007

For armoured rubble slopes and mounds the EurOtop 2007 (Pullen et al., 2007) presents empirical formulas based on the European Crest Level Assessment of Coastal Structures (CLASH) data base. It is able to quantify average overtopping values for various types of armoured slopes as shown by Equations 3.5 and 3.6 herebelow.

Mean value approach

$$\frac{q_{fr}}{\sqrt{g \cdot H_{m0}^3}} = 0.2 \cdot exp\left[-2.6\frac{R_c}{H_{m0} \cdot \gamma_f \cdot \gamma_\beta}\right] \tag{3.5}$$

Design and assessment approach

$$\frac{q_{fr}}{\sqrt{g \cdot H_{m0}^3}} = 0.2 \cdot exp\left[-2.3\frac{R_c}{H_{m0} \cdot \gamma_f \cdot \gamma_\beta}\right] \tag{3.6}$$

Where q_{fr} is the average overtopping discharge expressed in m^3/s/m at the front of the crest, H_{m0} the spectral wave height, γ_f the roughness coefficient and γ_β is the reduction coefficient when waves approach under a different angle than shore normal. The roughness coefficients were derived by Bruce et al. (2009) for rock slopes and different type of armour units on sloping permeable structures. Important to note: in case of a wave wall element placed on top of the breakwater, the height of the wave wall (R_c) should be used in Equations 3.5 and 3.6. For comparisons with laboratory experiments, Pullen et al. (2007) mentions to use the mean value approach, Equation 3.5. Equation 3.6 does not vary much from Equation 3.5. Yet, includes a standard deviation for safety and is advised for the deterministic design or safety assessment approach. Moreover, for armoured crests, a reduction factor is applied which is multiplied with the calculated average overtopping at the front of crest (q_{fr}), accounting for energy dissipation and leaking of water through the crest, using Equations 3.7 and 3.8 (Besley, 1999).

$$C_r = 3.06 \cdot exp\left(-1.5 \cdot \frac{W_{crest}}{H_{m0}}\right) \quad \text{with maximum} \quad C_r = 1 \tag{3.7}$$

$$q_{end} = C_r \cdot q_{fr} \tag{3.8}$$

Where C_r is the reduction coefficient accounting for the dissipation along the armoured crest, W_{crest} the width of the crest until reaching the wave wall and q_{end} the average overtopping discharge measured at the end of the crest. In cases W_{crest} < 0.75·H_{m0} no reduction (C_r = 1) is applied. Finally, the results obtained using this method are not reported as the method was improved in the EurOtop 2018 guidelines (see Section 3.2.6).

3.2.3. Overtopping neural network

The Neural Network (NN) by van Gent et al. (2007) may also be applied to assess the average overtopping quantities. Neural networks find their use for solving difficult modelling problems, e.g. for modelling coastal processes for which the relationship of the individual input parameters is unclear, but where enough experimental data is available to identify correlations. The CLASH data base was primarily created as the foundation for a generic overtopping prediction method based on artificial neural networks. The developed tool can be found on the Deltares web page[1] and is open source. The Neural Network uses 15 input parameters. The relation between all of them, described as a black box, is unclear.

3.2.4. Molines and Medina 2015

Molines and Medina (2015) re-calibrated the roughness coefficients, γ_f, for non-breaking waves interacting with rubble mound breakwaters. This was done for the EurOtop 2007 (Pullen et al., 2007) and Neural Network (van Gent et al., 2007), making use of the best available overtopping data (selected cases from the CLASH data base). The bootstrap method (sampling data set with replacement) was applied, which resulted in 10%, 50% and 90% values for each type of roughness coefficient (e.g. rocks, blocks or other type of revetments) and empirical overtopping formula. Molines and Medina (2015) selected 555 cases from the CLASH data base to re-calibrate the roughness coefficient (double rock layer placed on top of a permeable core), which was applied to the following ranges, shown in Table 3.1.

Armour type	No. Data	H_{m0} [m]	$T-1,0$ [s]	R_c [m]	A_c [m]	G_c [m]	$cot\alpha$	h_t [m]	h [m]	B_t [m]
Rock (2 L)	555	0.051–0.203	0.800–2.560	0.062–0.370	0.010–0.300	0.000–0.360	1.33–4.00	0.087–0.730	0.138–0.730	0.000–0.140

Table 3.1: CLASH data base ranges for which the roughness coefficient (double rock layer) was re-calibrated.

The experimental data (see Chapter 2 Table 2.1) lies within the ranges for which the roughness coefficient was re-calibrated. Therefore, the method is expected to perform well. The median values of the roughness factors, $\gamma_{f,50\%}$, are used to estimate the mean overtopping discharges.

3.2.5. Molines and Medina 2016

Molines and Medina (2015) found that the overtopping Neural Network with reassessed roughness coefficients performed best in assessing average overtopping quantities under different circumstances (555 cases with varying geometries and hydraulic boundary conditions). However, the tool is a black box, not showing how it computes average overtopping discharges with according confidence bounds. Therefore, Molines and Medina (2016) created a new and explicit overtopping formula that provides estimates in case of conventional mound breakwaters with or without a toe, in non-breaking wave conditions. The derived formula is able to predict average overtopping quantities as accurately as the neural network, as well as the relations between all input parameters. By mutually studying all environmental and structural variables which affect overtopping in case of conventional mound breakwaters, Molines and Medina (2016) found Equation 3.9.

$$\frac{q_{end}}{\sqrt{g \cdot H_{m0}^3}} = exp\left[\lambda_2 \cdot \lambda_3 \cdot \lambda_4 \cdot \lambda_5 \cdot \lambda_6 (a_1 + b_1 \cdot \frac{R_c}{H_{m0}} \cdot \frac{1}{\gamma_f \cdot \gamma_\beta})\right] \tag{3.9}$$

Where

$$\lambda_2 = a_2 + b_2 \cdot \left(\xi_{m-1,0} \cdot \sqrt{\frac{R_c}{H_{m0}}}\right) \tag{3.10}$$

$$\lambda_3 = a_3 + b_3 \cdot \exp\left(c_3 \frac{R_c}{h}\right) \tag{3.11}$$

[1]The Neural Network tool can be found on the Deltares web page, www.deltares.nl/en/software/overtopping-neural-network.

$$\lambda_4 = \max\left[c_4; a_4 + b_4 \cdot \frac{W_{crest}}{H_{m0}}\right] \tag{3.12}$$

$$\lambda_5 = a_5 + b_5 \cdot \frac{A_c}{R_c} \tag{3.13}$$

$$\lambda_6 = d_6 \tag{3.14}$$

The left term of Equation 3.10 can be computed by filling in the needed hydraulic boundary conditions at the toe of the conventional breakwater accompanied by the structural parameters. The values of the constant parameters a_j, b_j, c_j and d_j can be found in Table 3.2. The roughness factor, γ_f, for the latter method is equal to 0.48.

Subscript	a_j	b_j	c_j	d_j
1	-1.6	-2.6	0	0
2	1.20	-0.05	0	0
3	1.0	2.0	-35	0
4	0.85	0.13	0.95	0
5	0.85	0.15	0	0
6	1.2	-0.5	1	1

Table 3.2: Parameters reported in Molines and Medina (2016) to compute the dimensionless overtopping discharge.

3.2.6. EurOtop 2018

The EurOtop 2018 by Van der Meer et al. (2018) is widely renowned as the state of the art work and is used as design tool for various coastal structures (e.g. dikes, sea walls and rubble mound breakwaters). In the following section the improvements introduced compared to version 2007 (Pullen et al., 2007) will be discussed and an explanation will be given on how the overtopping discharge is obtained according to the modern EurOtop guidelines. Being the EurOtop 2018 approach, an improved version of the previous manual, the results concerning the EurOtop 2007 can be disregarded.

Overtopping at low to zero freeboard conditions have often been overlooked in physical model studies, leading to a gap in available data on which empirical formulas were fitted. However, low to zero freeboard conditions are often encountered, e.g. breakwaters under construction, low-free board breakwaters, etc. The EurOtop 2007 used a straight-line approach (see Equation 3.15), on log-linear paper, which in the low to zero free board region ($R_c/H_{m0} < 0.5$) often over-estimates the average overtopping. Where coefficients a and b are fitted, which depend on the type of coastal structure the formula is describing, e.g. dikes or rubble mound breakwaters. van der Meer and Bruce (2013) re-analysed old works providing a prediction to zero freeboard, which the EurOtop 2007 formula was not designed for. A curved line was proposed, introducing an exponent c, making the formula (see Equation 3.16) applicable to the full data range $R_c/H_{m0} > 0$. The formula widens the application area, but is very similar in the area with $R_c/H_{m0} > 0.5$, and has been introduced in the new EurOtop guidelines.

EurOtop 2007 approach

$$\frac{q_{fr}}{\sqrt{g \cdot H_{m0}^3}} = a \cdot exp[-b\frac{R_c}{H_{m0}}] \tag{3.15}$$

EurOtop 2018 approach

$$\frac{q_{fr}}{\sqrt{g \cdot H_{m0}^3}} = a \cdot exp[-(b\frac{R_c}{H_{m0}})^{\mathbf{c}}] \tag{3.16}$$

The presented breakwater (see Chapter 2) is a rubble mound breakwater superimposed by a vertical wave wall (protruding or non-protruding). The guidelines presented in the EurOtop for the latter case can be found in Chapter 6 (Armoured rubble slopes and mounds), where the formulas are based on Equation 3.16. When comparing model outcomes and measurements with empirical outcomes, the EurOtop advises to use Equation 3.17. On the other hand, when considering the design of the breakwater, Equation 3.18 is suggested, where a standard deviation is added to account for uncertainties.

Mean value approach

$$\frac{q_{fr}}{\sqrt{g \cdot H_{m0}^3}} = 0.09 \cdot exp[-(1.5\frac{R_c}{H_{m0} \cdot \gamma_f \cdot \gamma_\beta})^{1.3}] \tag{3.17}$$

Design and assessment approach

$$\frac{q_{fr}}{\sqrt{g \cdot H_{m0}^3}} = 0.1035 \cdot exp[-(1.35\frac{R_c}{H_{m0} \cdot \gamma_f \cdot \gamma_\beta})^{1.3}] \tag{3.18}$$

Where the used parameters have the same meaning as explained before in Section 3.2.2. The above mentioned Equations 3.17 and 3.18 are applicable for slopes ranging from 1:2 to 1:4/3, which are satisfied by the experimental cases in this research. As was done in Section 3.2.2 a coefficient for energy dissipation (C_r) is introduced to account for energy losses which reduce the average overtopping quantities at the end of the crest (see Equations 3.7 and 3.8). With regard to the effect of the protruding wave wall on the average overtopping value, Van der Meer et al. (2018) states that for the R_c value (see Equation 3.17) the height of the wave wall compared to the SWL should be used. In case the wall does not protrude and is equal to the height of the armour layer, the Equation 3.17 reported above can be applied.

3.3. Comparison

In this section a comparison is made between the considered empirical methods and the outcomes of the 54 performed physical laboratory experiments. The comparison is expressed in terms of the root mean squared error, following Equations 3.19. The Irribarren number for all the cases is higher than 2.5 (see Chapter 2) regarded as non-breaking or surging waves. In case of non-breaking waves, the EurOtop uses figures such as Figure 3.1 to compare empirical outcomes (using input parameters; see Table 3.3) with experimental results. The dimensionless mean overtopping ($q/\sqrt{gH_{m0}^3}$) is plotted against the relative freeboard (R_c/H_{m0}). Applying the EurOtop 2018 guidelines without the re-calibrated roughness coefficients by Molines and Medina (2015), induce under-estimations in the order of a factor 2-273x (see Figure 3.1). It is worth noting that the original EurOtop 2018 method induces errors ranging between **2-30x** for non-protruding wave wall cases and **14-273x** for protruding cases.

$$RMSE = \sqrt{\frac{\sum_{i=1}^{N}(q_{i,emp} - q_{i,mes})^2}{N}} \tag{3.19}$$

Input parameters	Symbol	Value	Unit
Crest width	W_{crest}	0.114	m
Front slope	$tan(\alpha)$	0.5	-
Gravitational constant	g	9.81	m^2/s
Roughness coefficient - EurOtop 2018 (original)	γ_f	0.40	-
Roughness coefficient - Molines and Medina (2015) - EurOtop 2007	γ_f	0.53	-
Roughness coefficient - Molines and Medina (2015) - Neural Network	γ_f	0.49	-
Roughness coefficient - Molines and Medina (2016)	γ_f	0.48	-
Obliquity coefficient	γ_β	1	-
Free board	R_c	0.097-0.250	m
Spectral wave height	H_{m0}	0.078 - 0.171	m
Water level	d	0.70-0.80	m

Table 3.3: Input parameters for the previous empirical methods.

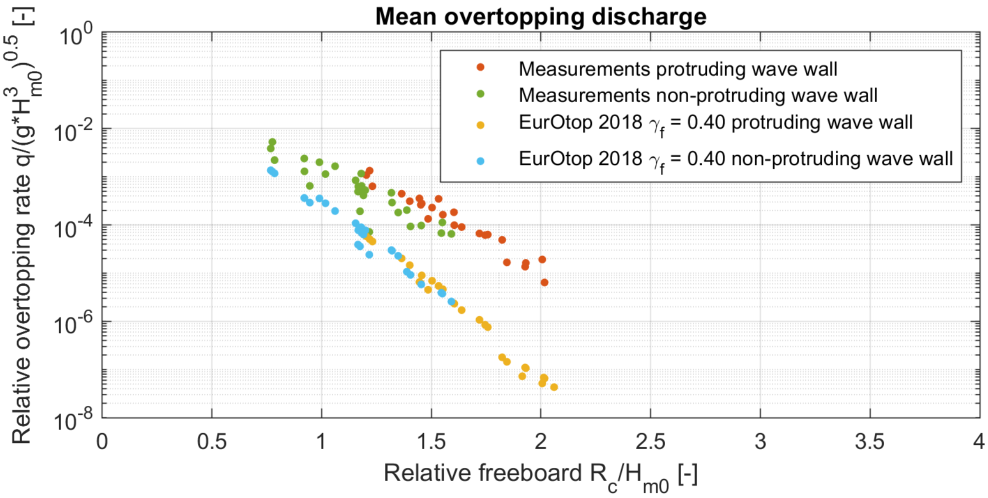

Figure 3.1: Mean overtopping discharges for 54 physical laboratory experiments, including a comparison between physical laboratory measurements and the EurOtop 2018 guidelines (γ_f = 0.40).

Molines and Medina (2015) reassessed the used roughness coefficients by considering a portion of the CLASH data base. It should be noted that Molines and Medina (2015) did not calibrate the roughness coefficient for the EurOtop 2018 formula, but only for the EurOtop 2007 method. Nonetheless, the roughness coefficient is calibrated in the present research for the EurOtop 2018 approach, based on the 54 available physical laboratory experiments. The roughness coefficients are computed for each case so that the EurOtop 2018 overtopping discharge equals the measurement. The case specific roughness coefficients, considering all the non-protruding and protruding wave wall cases, are subsequently averaged and have a mean of 0.53 and a standard deviation of 0.05. The found roughness coefficient (mean value of 0.53) is equal to what was reported by Molines and Medina (2015) for the EurOtop 2007 approach (see Table 3.3 above). Consequently this research agrees with Molines and Medina (2015) that the original EurOtop 2018 roughness (γ_f = 0.40) under-estimates the average overtopping discharges compared to measurements. The re-calibrated roughness coefficients for all considered methods, according to Molines and Medina (2015), are reported in Table 3.3. Applying the re-calibrated roughness coefficient (γ_f = 0.53, based on the 54 available physical experiments) within the EurOtop 2018 approach is referred to as ”the updated EurOtop 2018 method” and is used from this point onwards. When the updated empirical methodology is compared with measurements, an improvement can be observed, as shown in Figure 3.2.

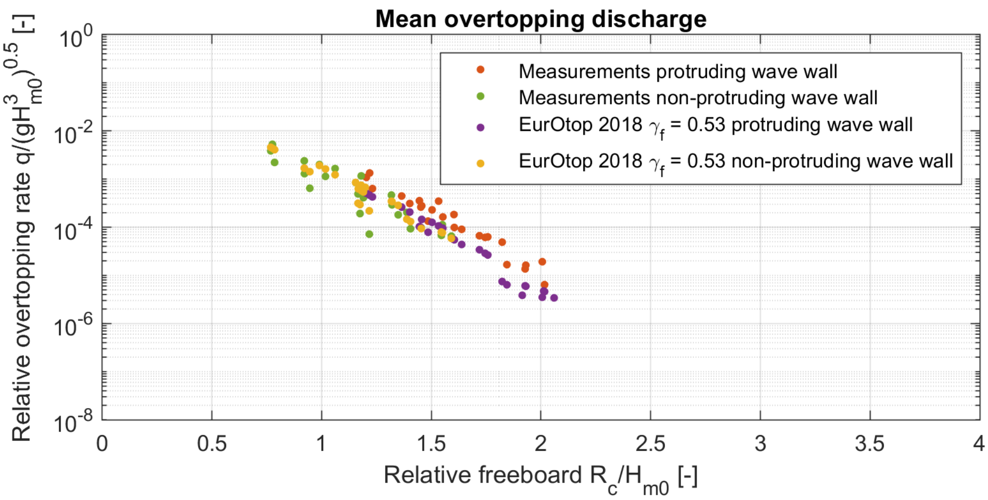

Figure 3.2: Mean overtopping discharges for 54 physical laboratory experiments, including a comparison between physical laboratory measurements and the updated EurOtop 2018 guidelines (γ_f) = 0.53.

In Figure 3.2 the EurOtop 2018 cloud of data points is shifted upwards, compared to Figure 3.1, since the roughness coefficient is changed from γ_f = 0.40 to γ_f = 0.53. The NN and Molines and Medina 2016 approaches are not shown as the reported errors in Table 3.4 were higher compared to the EurOtop 2018 (updated) approach.

Geometry	Mean measured value [m^3/s/m]	Empirical method	RMSE [m^3/s/m]
Protruding	$3.39 \cdot 10^{-5}$	EurOtop 2018 - Molines	$3.19 \cdot 10^{-5}$
		Neural Network - Molines	$3.60 \cdot 10^{-5}$
		Molines and Medina 2016	$3.30 \cdot 10^{-5}$
Non-protruding	$14.56 \cdot 10^{-5}$	EurOtop 2018 - Molines	$6.86 \cdot 10^{-5}$
		Neural Network - Molines	$8.60 \cdot 10^{-5}$
		Molines and Medina 2016	$11.30 \cdot 10^{-5}$

Table 3.4: Root mean squared errors compared to measurements, including a comparison between: the EurOtop 2018, the Neural Network and Molines and Medina 2016. The mean measured average overtopping discharges over the respective 27 cases (non-protruding or protruding) are reported to interpret the magnitude of the reported errors (RMSE).

Concluding, the EurOtop 2018 approach with the re-calibrated roughness coefficient performed best in case of a protruding wave wall with a RMSE value of $3.19 \cdot 10^{-5}$ (m^3/s/m). Also, for the non-protruding wave wall cases the EurOtop 2018 resulted in the lowest RMSE value, equal to $6.86 \cdot 10^{-5}$ (m^3/s/m).

3.4. Provisional conclusions

When comparing the results of the presented overtopping formulas with the available measurements it can be concluded that: the original (non-calibrated) empirical method (EurOtop 2018) shows shortcomings. Considering the non-protruding wave wall test samples, the dimensionless overtopping discharges undermine the measurements (a factor ranging between 2 and 30x). The discrepancies are noticeably higher for protruding wave wall cases (a factor a factor ranging between 14 and 273x). This reveals that for increasing structural complexity (protruding wave wall) the EurOtop 2018 approach becomes less reliable. On the other hand, while considering the re-calibrated roughness coefficients, applicable in the considered data range (see Section 2.3), the updated EurOtop 2018 shows improved results and is compared to other empirical approaches (NN and Molines and Medina 2016). For both protruding and non-protruding wave wall the updated EurOtop 2018 showed the highest accuracy. The updated (γ_f = 0.53) approach will therefore be compared with model outcomes in Chapter 7.

4

Numerical Model

4.1. Introduction

In this chapter the framework, the mathematical equations, several theoretical aspects and the set-up of the numerical model are examined. First, the numerical framework, consisting of multiple software packages which, when compiled together, solve complex wave-structure interactions, is briefly discussed. Thereafter, a description of the mathematical model is given. Aspects such as the Reynolds-Averaged Navier-Stokes equations (RANS), the porous flow model, turbulence and the Volume Of Fluid (VOF) approach are touched upon. Thereafter, the wave generation toolbox and the relaxation zone technique are examined. The applied methodology to avoid air entrapment in 2D numerical simulations, referred to as "the ventilated boundary" technique, is briefly discussed next followed by the adopted method by the numerical model to capture the overtopping over the breakwater. Finally, the numerical set-up is discussed.

4.2. Numerical framework

The numerical model used in the present research is the OpenFOAM/waves2Foam. Various packages are compiled together (see Figure 4.2). For the sake of simplicity in the present research the total of these packages is referred to as "CoastalFOAM". The input used by Jacobsen et al. (2018) for the validation of forces acting on a protruding wave wall will be applied as starting point in this research. The model will be validated considering average overtopping discharges for protruding and non-protruding wave walls as explained in Chapter 1. The core of the numerical framework consists of the open-source model OpenFOAM (Weller et al., 1998). This is an open-source library consisting of C++ libraries and codes which have the ability to solve CFD problems using finite volume discretization. The library contains pre and post-processing tools and is able to run simulations in parallel, increasing numerical efficiency. Moreover, OpenFOAM is capable of handling two phase flows by linking the RANS equations to a Volume Of Fluid (VOF) method (see Section 4.3.5) in order to capture the free surface.

Additionally, the waves2Foam library (Jacobsen et al., 2012) was released as a plug-in toolbox to the OpenFOAM package and is used to generate and absorb free surface water waves. The method thereto applies the relaxation zone technique (see Section 4.4.1). The toolbox was extended with the possibility of modelling flow through porous media, e.g. rubble mound breakwaters (Jensen et al., 2014). The extension was achieved by volume averaging the momentum equation, which introduced extra terms. These additional terms describe the frictional forces caused by the presence of the flow disturbing structure characterised by its skeleton. The frictional forces are described by an extended form of the Forchheimer equation.

In this research the waves are generated by the relaxation zone placed at the inlet of the OpenFOAM domain. The boundary conditions (waves) used as input for the inlet relaxation zone (applied to transfer the wave conditions from the OceanWaves3D to the OpenFOAM domain as further explained in Section 4.4.1) are generated with a potential flow solver called OceanWave3D (Engsig-Karup et al., 2009). The numerical wave flume therefore consists of an OpenFOAM model nested within an OceanWave3D (OCW3D) model (see Section 4.4), as visualised in Figure 4.1.

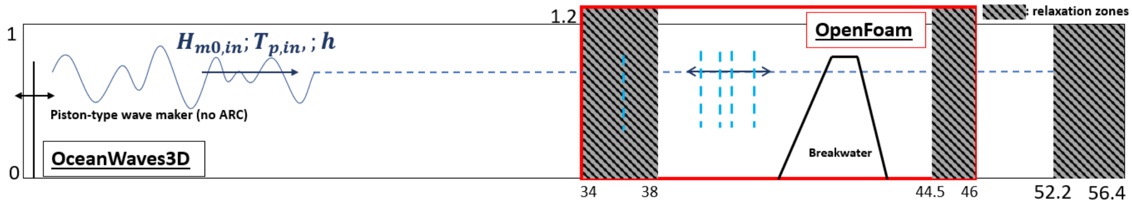

Figure 4.1: Sketch showing the nested OpenFOAM domain within the OceanWaves3D domain, dimensions reported in meters.

The OpenFOAM model is coupled with an OceanWaves3D model because:

- OceanWaves3D uses steering files as input to produce the desired wave conditions. These steering files contain the exact wave paddle velocity time series which were saved during the performed physical laboratory experiments, resulting in comparable wave conditions between the numerical and physical flumes.
- The OpenFOAM domain from the wave paddle to a couple of wave lengths in front of the rubble mound breakwater can be replaced by a combination of an inlet relaxation zone and OceanWaves3D. The latter is numerically more attractive to use (potential flow solver) compared to NS solvers (computationally very heavy) in regions where the potential flow assumption is valid. Combining both models increases numerical efficiency.

The coupling between OpenFOAM and OceanWaves3D was done by Paulsen et al. (2013) and is referred to for further details.

Lastly, numerous validation studies using CoastalFOAM have been performed before and during the period of the JIP CoastalFOAM (2015-2019). Examples of such validation areas are: formation and development of a breaker bar under regular waves, wave reflection, transformation, damping, induced set-up, forces and sediment transport in open filters (Jacobsen and Fredsoe, 2014; Jacobsen et al., 2015; van Gent and Wolters, 2015; Jacobsen et al., 2017). Developments and improvements during the period of the JIP, such as tools and processing utilities, are added to the numerical framework by compiling the JIPCoastalFOAM toolbox (version 10) to the waves2Foam package. The ventilated boundary, introduced by Jacobsen et al. (2018), is an example of such developments and will be used in this research (see Section 4.5).

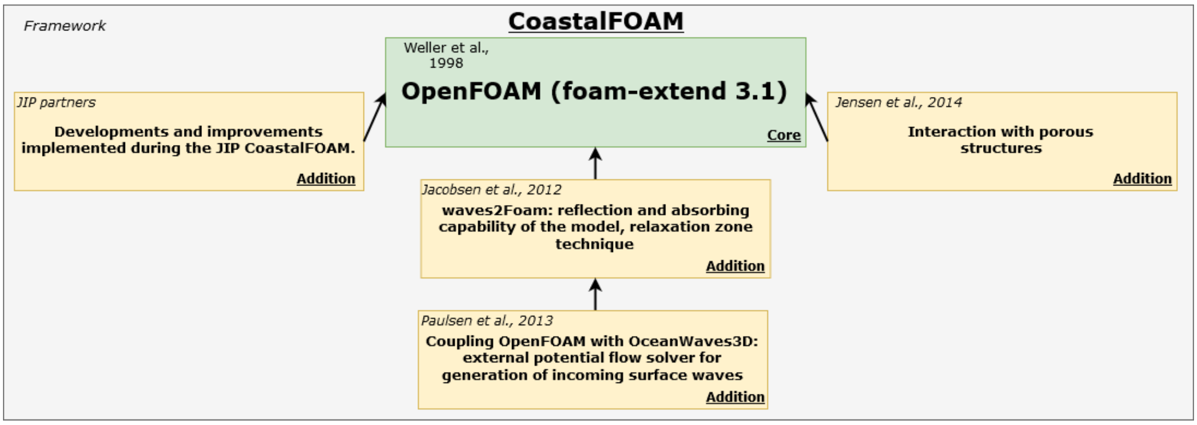

Figure 4.2: The numerical model OpenFOAM with the various additional packages (Waves2Foam, OceanWaves3D and JIP CoastalFOAM improvements) for ease of reference in this report globally referred to as "CoastalFOAM".

4.3. Mathematical model

After having described in Section 4.2 the numerical framework used in this research, the mathematical equations used in the numerical wave flume are addressed below. Important theoretical aspects that require more attention are examined and discussed along the way.

4.3.1. Hydrodynamic model

The hydrodynamic model is based on the Reynolds Averaged Navier-Stokes (RANS) equations, discussed in Section 4.3.2. As mentioned in Section 4.2, Jensen et al. (2014) presented these equations in a way to account for permeable coastal structures. The RANS model uses the continuum approach. Therefore, Jensen et al. (2014) defined the velocity as the filter velocity in the Navier-Stokes equations (see Equations 4.1 and 4.2; mass and momentum conservation respectively).

$$\nabla \cdot \mathbf{u} = 0 \tag{4.1}$$

$$(1 + C_m) \cdot \frac{\partial}{\partial t}\frac{\rho \mathbf{u}}{n_p} + \frac{1}{n_p} \cdot \nabla \frac{\rho}{n_p} \mathbf{u}\mathbf{u}^T = -\nabla p^* + g \cdot \mathbf{x} \cdot \nabla \rho + \frac{1}{n_p} \cdot \nabla \mu_u \cdot \nabla \mathbf{u} - \mathbf{F}_p \tag{4.2}$$

Where C_m is the added mass coefficient, t is the time, ρ is the density of the fluid, $\mathbf{u}$ is the filter velocity expressed in Cartesian coordinates, p^* is the excess pressure, $\mathbf{x}$ is the Cartesian coordinate vector ([x, y, z]), μ_u is the dynamic viscosity of the velocity field and $\mathbf{F}_p$ is the resistance induced on the flow by the presence of permeable coastal structure (see 4.3.3). It is worth mentioning that the sign in front of the gravitational term was mis-typed in Jensen et al. (2014) and has been corrected by Jacobsen et al. (2018). The excess pressure is defined as $p^* = p - \rho g \cdot \mathbf{x}$, p being the total pressure. The system of equations is closed by considering the incompressibility of the fluid, given by the continuity equation (see Equation 4.1). In the present research turbulence is not modelled for outside the structure. However, inside the breakwater turbulence will be accounted for by calibrating the dimensionless porous flow coefficients. The reason for this assumption is explained in Section 4.3.4. Tracking of the free surface in the OpenFOAM domain is performed with the VOF method and the MULES advection algorithm, a standard method available in the OpenFOAM package (see Section 4.3.5).

4.3.2. Reynolds-averaged Navier-Stokes model

The model used in this research is a Reynolds Averaged Navier Stokes (RANS) model, using time-averaged equations of the motion of fluid, introducing mean and fluctuating components. The transformation from Navier Stokes to RANS creates an extra term referred to as Reynolds stress which allows for turbulence modelling. This Reynolds stress term demands additional modelling to close the RANS equations for solving and therefore requires a turbulence closure model, as the number of unknowns (pressure, velocity and turbulence upon closure) is higher than the number of equations. Multiple closure models do exist, e.g. $k - \epsilon$ and $k - \omega$. Therefore, RANS models find their use in describing turbulent flows, giving approximated time-averaged solutions to the Navier-Stokes equations. The influence of porous flow is implemented by introducing resistance terms (F_p) in the flow equations (see Equation 4.2), which is described by the Darcy-Forchheimer resistance equation, explained in more detail in Section 4.3.3. The porous media (e.g. armour, filter layers and core), consisting of a skeleton with pores, are represented as a continuum.

4.3.3. Flow resistance

The flow resistance, induced by the presence of the permeable structure, is described by two terms. First, the added mass coefficient C_m, which accounts for inertial effects caused by the presence of the porous skeleton as defined by van Gent (1995) and shown in Equation 4.3.

$$C_m = \gamma_p \frac{1 - n_p}{n_p} \tag{4.3}$$

Where γ_p is an empirical constant, which is set to 0.34 in the present research. Second, the parameterisation of van Gent (1995) is used to outline the flow resistance term, described by the Darcy-Forchheimer resistance equation (see Equation 4.4).

$$\mathbf{F}_p = a\rho\mathbf{u} + b\rho||\mathbf{u}||_2\mathbf{u} \tag{4.4}$$

Where the first linear term dominates linear flow regimes and the second non-linear term dominates turbulent regimes. The closure coefficients a and b are evaluated based on the parametrisation of van

Gent (1995) using Equation 4.5.

$$a = \alpha \frac{(1-n_p)^2}{n_p^3} \frac{\nu}{D_{n50}^2} \quad \text{and} \quad b = \beta (1 + \frac{7.5}{KC}) \frac{1-n_p}{n_p^3} \frac{1}{D_{n50}} \tag{4.5}$$

Where D_{n50} is the nominal diameter of the permeable layer (e.g. core, filter or armour layer in case of a breakwater), KC is the Keulegan-Carpenter number (e.g. for stones) and α and β are closure coefficients. Jacobsen et al. (2015) used standard values based on the recommendations by van Gent (1995) as follows: α = 1.000 and β = 1.1. However, various combinations can be used for the closure coefficients in order to obtain the same results (Jensen et al., 2014). Indeed, not only one combination exist and wide ranges of closure coefficients can be found in literature (Losada et al., 2016). The d_{50} (mean rock size for which 50% of the rocks are smaller) is often used in the formulas (Jensen et al., 2014). However it is the D_{n50} as defined in van Gent (1995) that is applied here. The KC number for stones is not an easy parameter to estimate, due to rapid damping of waves through the permeable structures. As a consequence, a temporal and spatial varying KC number should be used in the model, as done in IHFOAM (Higuera et al., 2013, 2014a,b). However, a simplified approach will be used in this research, where the KC number will be estimated based on the incoming wave field and the shallow water wave theory as described in the following Equation 4.6.

$$KC = \frac{H_{m0}}{2} \sqrt{\frac{g}{h}} \frac{1.1 T_{m-1,0}}{D_{n50}} \tag{4.6}$$

Where $T_{m-1,0}$ is considered the most appropriate wave period in case of wave reflection (Dekker et al., 2007) and in wave overtopping studies (van Gent, 1999). It is therefore used to calculate KC.

4.3.4. Turbulence modelling

Both Jensen et al. (2014) and Jacobsen et al. (2015) showed the possibility to correctly represent the bulk hydrodynamics (free surface elevation, wave absorption and reflection) without directly accounting for turbulence. In Jacobsen et al. (2015) wave breaking played little or no role and hardly any production of turbulence was experienced outside of the breakwater. Therefore, including turbulence models - RNG or $k-\epsilon$ - would increase computational time without increasing the accuracy of the outcomes. Nevertheless, inside the breakwater turbulence will be produced. The amount of turbulence will depend on the dimensions of the stones composing the layers and the magnitude of the incoming waves. Jensen et al. (2014) pointed out that the obtained resistance coefficients by van Gent (1995) were calibrated taking into account the dissipative effects of turbulence inside the breakwater. Forces have been validated following this approach (Jacobsen et al., 2018), thus not accounting for turbulence outside the breakwater. The same approach will be used for the present validation of the wave overtopping over the rubble mound breakwater. No turbulence will be modelled outside the structure (ξ > 2.5-3 resulting in surging waves). However, inside the breakwater turbulence will be accounted for by calibrating the α, β and KC resistance coefficients.

4.3.5. Volume of fluid (VOF)

At the interface between waves and coastal structures the flow is expected to be highly non-linear (e.g. due to wave breaking and reflection) and therefore assumptions such as potential flow theory (OCW3D) are not applicable. To correctly model these cases a two-phase incompressible Navier-Stokes solver was introduced to the RANS model, addressing flow of water and air. The free surface waves are captured/tracked with an extended VOF equation (see Equation 4.7) as explained in detail in Berberović et al. (2009). The VOF method has been used in numerical studies to capture various complex coastal processes, e.g. wave reflection, wave transformation over a shoal, wave damping, wave set-up, wave overtopping and forces in 2D and 3D (Higuera et al., 2013, 2014a,b; Jacobsen et al., 2015). In order to obtain a non-diffusive solution, which is often the case when solving transport type equations (see Equation 4.7 herebelow), the numerical model (OpenFoam) uses the standard MULES (multidimensional limiter scheme) technique.

$$\frac{\partial \alpha}{\partial t} + \frac{1}{n_p} [\nabla \cdot \mathbf{u} \alpha + \nabla \cdot \mathbf{u}_r (1-\alpha)\alpha] = 0 \tag{4.7}$$

Where $1/n_p$ ensures that only the pores of the material can be filled with water (n_p being the porosity of the permeable structure), and where u is the velocity (bold as it is expressed in Cartesian coordinates), and u_r the relative velocity between both fluids. Using a two-phase approach induces smearing of the interface between two fluids, which is reduced with the last term on the left side of the equation sign. The term is activated when α lies between 0 and 1 (when addressing foam), a so-called indicator function. This is a scalar function, found by solving Equation 4.7 in each control volume (computational grid cell). By doing this the volume fraction of the fluid in each cell is obtained and is tracked for all cells. Empty cells (not containing any fluids) are represented by an indicator function α equal to 0, whereas wet cells are indicated by α equal to 1. Computational cells which contain some fluid have values between 0 and 1. The value of α is then used to evaluate properties such as densities and viscosities in each grid cell, using the Equations 4.8 and 4.9 herebelow.

$$\rho = \alpha \cdot \rho_w + \rho_a(1 - \alpha) \tag{4.8}$$

$$\mu = \alpha \cdot \mu_w + \mu_a(1 - \alpha) \tag{4.9}$$

Where subscripts a and w represent air and water respectively. The obtained viscosities and densities are used within the RANS equations, which give the time-averaged velocities in each grid cell. These velocities are then applied in Equation 4.7 to re-evaluate the indicator function in each grid cell. This process is repeated for each dynamic time step. The normal on the fluid interface is established where α changes most rapidly. Moreover, in order to obtain accurate results, a refinement is needed around the water level, otherwise the free-surface would not be defined sharply. The VOF method is a computational efficient way to track the free-surface by adding only one extra equation, the advection equation.

4.4. Wave generation

During this research a fully non-linear wave climate, computed with the wave transformation model OceanWaves3D (Engsig-Karup et al., 2009), will be imposed. The advantages of using OceanWaves3D were explained in Section 4.2. OceanWaves3D is a fully nonlinear and dispersive potential flow model which overcomes the limitations of most Boussinesq-type models (applicable to weakly non-linear and fairly long waves). Potential flow models neglect viscous terms - which become more important upon wave breaking - and assume irrotational flow ($\nabla \cdot\ u = 0$). OceanWaves3D was a key element for the prediction of wave forces acting on the front of the crest wall on top of the rubble mound breakwater (Jacobsen et al., 2018). Consequently, OceanWaves3D will also play a key role in the 2D overtopping validation, ensuring comparable surface elevations (between the numerical model and the physical laboratory experiments). Closer to the coastal structure potential flow is not valid anymore and the waves generated within the OceanWaves3D domain are transferred to the OpenFOAM domain applying the relaxation zone technique as explained in Section 4.4.1 below.

4.4.1. Relaxation zone

Wave generating and absorbing capabilities of the numerical model were improved with the waves2Foam toolbox presented in Section 4.2. This toolbox uses the relaxation zone technique as boundary condition to avoid reflection of the waves at boundaries and waves reflecting internally which could influence the wave maker at the boundary. Relaxation zones work by weighing the computed solution (velocity and indicator function) and the target solution (based on the imposed wave theory, i.e. the solution modelled by OceanWaves3D). Both the velocity and the indicator function are solved each time step with the following Equations 4.10 and 4.11.

$$\phi = \alpha_R \cdot \phi_{computed} + (1 - \alpha_R) \cdot \phi_{target} \tag{4.10}$$

$$\alpha_R(\chi_R) = 1 - \frac{exp(\chi_R^{3.5}) - 1}{exp(1) - 1} \quad \text{for} \quad \chi_R \quad \in [0; 1] \tag{4.11}$$

Where ϕ is either the velocity $\mathbf{u}$ or the indicator function α. Important to note is that α_R is the relaxation function and is not equal to α, the indicator function mentioned in Section 4.3.5. χ_R is such that α_R is equal to 1 (χ_R is equal to zero) at the interface between the non-relaxed part of the computational domain and the relaxation zone, thus only the computed values remain. At the opposing side, χ_R is equal to 1 (α_R equal to zero) so that only the target values remain. Additionally, relaxation zones can fix the water level in the numerical flume, which is necessary in case of overtopping quantities to avoid undesired set-up due to trapped water.

4.5. Ventilated boundary

The numerical wave flume is two-dimensional. When waves run-up the structure and break against the protruding wave wall, the air within the enclosed pockets is not able to escape. This is called air entrapment. Waves in air-trapped closed cavities (2D) exert much larger forces on the structure than when small ventilation holes are present allowing air to escape, as it has been proved experimentally (Cuomo et al., 2009; Seiffert et al., 2015) and numerically (Bozorgnia et al., 2012; Hayatdavoodi et al., 2014; Jacobsen et al., 2015). Various solutions have been adopted, e.g. a small tube through which the entrapped air could escape (Bozorgnia et al., 2012; Seiffert et al., 2014). Nonetheless, this approach is numerically unattractive as the velocities generated through the tube could become very large inducing small dynamic time steps to ensure model stability. The model stability is indicated by the Courant number (see Equation 4.12), which during the run needs to be lower than a pre-defined value (e.g. 0.35). To reach numerical stability, the time step is set to be adaptive, so that the Courant number is kept below 0.35. Also, the Courant number is kept low to avoid smearing of the interface.

$$C_o = \frac{u \cdot \Delta t}{\Delta x} \tag{4.12}$$

Where u is the velocity, Δt the time step and Δx a fixed value based on pre and post processing meshing tools. Since the wave celerity cannot be altered, nor can the resolution of the grid during the run (fixed mesh is used), only time can be adapted ensuring a low Courant number. Time steps will vary along the simulation (so called dynamical time steps). To solve this time issue, Jacobsen et al. (2018) proposed to model the upper boundary of the cavity by means of a permeable boundary condition, referred to as ventilated boundary. The boundary is equipped with a certain degree of openness and is applied to the front wall of the concrete wave wall in this research. Jacobsen et al. (2018) found that computational time is reduced by a factor 20, compared with the small tubes through the wall approach. A 3% degree of openness was reported to provide the best results for the validation of forces and will therefore be adopted here.

4.6. Overtopping

The possibility to quantify wave overtopping has been added to the waves2Foam package. Overtopping discharges (q) and overtopping volumes (V) are captured by placing one or multiple overtopping faces over a group of cell faces. In the present research the dimensions of the overtopping face are chosen such to capture all the overtopped water over the protruding or non-protruding wave wall. Multiple overtopping faces can be defined along the crest width of the breakwater. To quantify the overtopping discharge the numerical model captures the flux of fluid going through each of the cell faces (f). Then, the overtopping discharge is calculated by summing up the face fluid fluxes through the respective cell faces over which the overarching overtopping face (ξ) is defined. Each of the face fluid fluxes is multiplied by the indicator function (see Section 4.3.5). The instantaneous directional overtopping discharge is then given by Equation 4.13 herebelow.

$$q = \sum_{f \in \xi} \phi_{F,f} \frac{S_f}{\parallel S_f \parallel^2} \tag{4.13}$$

Where q is the volume flux (discharge) in three directions, $\phi_{F,f}$ is the flux of fluid through a face f multiplied by the indicator function and this flux is positive in the direction of the dimensionless normal vector to the face S_f.

4.7. Numerical set-up

Having outlined the numerical framework, in this section the physical flume is reconstructed numerically. Multiple aspects are discussed: coupling between OpenFOAM and OceanWaves3D, geometry and mesh properties.

4.7.1. Model coupling

The numerical wave flume consists of an OpenFOAM model nested within an OceanWave3D model (see Figure 4.3). As OceanWaves3D is numerically attractive to use (potential flow solver) compared to OpenFOAM since it covers the domain from the wave paddle to a couple of wave lengths before the toe of the breakwater. As already mentioned, in this region the potential flow assumption is valid. Closer to the breakwater (highly energetic region due to wave-structure interaction) the potential flow assumption (irrationality and neglecting viscous terms) is not valid anymore. OpenFOAM is therefore applied closer to the breakwater. The assessment of the coupling quality is done by placing wave gauges at equal positions in both numerical models (light blue dotted lines in Figure 4.3). Figure 4.3 shows that the incoming waves are transferred from the OceanWaves3D domain to the OpenFOAM domain through the left relaxation zone. The latter has two functions: damping of the reflected waves due to the wave-structure interaction and transferring the incoming surface waves from the OceanWaves3D to the OpenFOAM domain.

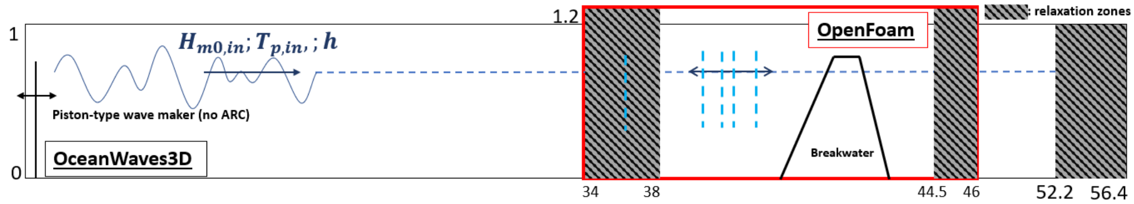

(a) OceanWaves3D domain.

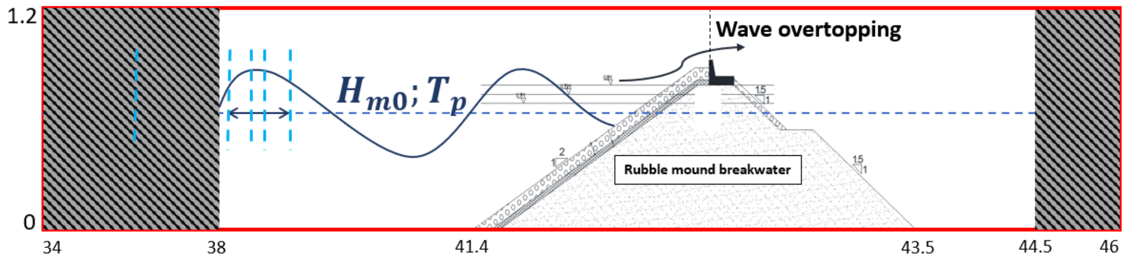

(b) OpenFOAM domain.

Figure 4.3: [NTS = not to scale] Sketch of the numerical wave flume: a) OceanWaves3D domain; b) OpenFOAM domain. Dimensions are given in meters

4.7.2. Geometry

The rubble mound breakwater is included in the numerical flume by applying the porous media concept. When water flows through the rubble mound breakwater it experiences resistance. Instead of considering the stones individually, a continuum approach is preferred where their spatially averaged effect is taken into account. This results in layers (sponge layers) consisting of multiple stones which overall induce resistance on the flow. As explained in Section 4.3.3, the parametrisation of van Gent (1995) is used to describe the induced resistance on the flow. The resistance is dependent on the D_{n50} (rock grading) and n_p (porosity) and thus varies for each layer (core, filter and armour). In the physical flume the porosities were not measured, yet an initial n_p = 0.4 is assumed for every layer in line with the work of Jacobsen et al. (2018). Considering the grading types, the D_{n50} values are 0.007 m, 0.017 m and 0.036 m for the core, filter layer and armour layer respectively. The thickness of the filter layer is 0.031 m and that of the armour layer is 0.066 m as shown in Chapter 2. Furthermore, to close the parametrisation of van Gent (1995) resistance coefficients (α, β and KC) are needed. Initially, the recommended values, i.e. α = 1,000 and β = 1.1 according to van Gent (1995), are applied for every layer. The KC is set to 10,000. The aforementioned parameters were adopted by Jacobsen et al.

(2018) and are therefore taken as starting position for this work.

4.7.3. Mesh properties

For the validation of OpenFOAM, a relatively fine mesh is used (see Figure 4.4). Square cells are used (Δx = Δy), which according to Jacobsen et al. (2012) give the most accurate results considering wave propagation towards the structure. The under-laying coarse mesh (Δx_1) contains cells of 1.25x1.25 cm. Around the water surface the mesh is refined by a factor 2 giving cells of 0.625x0.625 cm, which follows the rule of thumb suggesting that the wave height of interest should be divided into 10-20 points. Around the wave wall element a second refinement is performed which results in cell sizes of 0.3125x0.3125 cm (Δx_3). A ventilated boundary is then placed on the left boundary of the wave wall, defined by a certain degree of openness (3%), as explained in Section 4.5. The presented mesh follows from a sensitivity analysis performed by Jacobsen et al. (2018). In total, the domain consists of approximately 130,000 computational cells which become 180,000 after performing the above mentioned refinements.

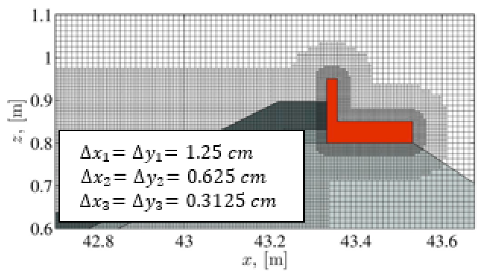

Figure 4.4: OpenFOAM mesh resolutions, from coarse to fine around wave wall (based on Jacobsen et al. (2018)).

4.7.4. OceanWaves3D

OCW3D makes use of the wave paddle velocity registered during the physical laboratory experiments as boundary condition. The active reflection compensation applied in the physical flume due to reflection is filtered out since OCW3D uses the relaxation zone technique at the end of the numerical flume (see Figure 4.3a above) to dampen out the incoming waves. The relaxation zone has the length of one peak wavelength (L_p), computed with linear wave theory. The length of the OCW3D domain should at least be equal to the length of the physical flume. This to ensure that the propagating waves travel the same distance in the physical and numerical flume. The OCW3D domain dimensions are given in Figure 4.3. A horizontal bathymetry is loaded in OCW3D. Furthermore, OCW3D uses a vertically clustered grid, characterised by an increased resolution towards the free water surface, which enhances the accuracy of the propagating waves. The mesh resolution used by Jacobsen et al. (2018) in OCW3D are 12 grid points in the vertical direction and approximately 80 grid points per peak wave length in the horizontal direction.

5
Model validation

5.1. Introduction

In the previous chapter the framework and set-up of the numerical model were explained. The next step is the validation of the average overtopping discharge over the rubble mound breakwater. This is done in two phases: the calibration phase and the evaluation phase. The calibration phase consists of multiple steps. First, the total surface elevation in front of the breakwater is compared with measurements, as the surface elevation closest to the structure directly affects the overtopping results. Second, the total surface elevation is decomposed in an incoming and reflective part using the Zelt and Skjelbreia (1992) technique, opening up the possibility to compare the incoming and reflected modelled and experimentally measured surface elevations. Discrepancies in modelled and measured incoming signals are visualized, located and corrected. Third, the reflection coefficients induced by the presence of the structure in both the numerical and the experimental flume are studied. Here, the influence of the porous flow parameters (according to the parametrisation of van Gent (1995)) on the reflection coefficient is elaborated. The influence of various model input parameters on the wave overtopping over the breakwater is studied in a sensitivity analysis based on a specific case. Once the model has been calibrated and the numerical settings fixed, in the evaluation phase the average overtopping values can be assessed to validate the numerical model for small to large overtopping discharges.

5.2. Calibration case and procedure

Calibration of the numerical model is done for one out of the six previously picked cases. Assuming the numerical model can represent the selected case accurately, the other five cases will be modelled using the same procedure and implemented improvements. Case A3W1T205 (non-protruding wave wall, medium overtopping) is chosen to build up the calibration methodology and show if the numerical model can quantify the average overtopping precisely. According to Romano et al. (2015) considering 500 waves is enough to accurately assess the average overtopping discharge and is therefore chosen as threshold duration for upcoming runs. A non-protruding sample is studied first, reducing geometric complexity.

The designated case (A3W1T205) can be visualised with the hydraulic and geometrical parameters shown in Figure 5.1 and Table 5.1. The validation procedure, consisting of multiple calibration and evaluation phases, can be outlined as follows:

- Comparison of the total surface elevation at the wave gauge closest to the toe of the rubble mound breakwater, wave gauge 5, in terms of spectral properties (H_{m0}).
- Reflection analysis using the method by Zelt and Skjelbreia (1992) is adopted with 5 gauges, resulting in incoming and reflected surface elevations.
- Comparison of incoming surface elevation at wave gauge 5 in terms of spectral properties ($H_{m0,i}$).
- Calibration of incoming surface elevation at wave gauge 5.

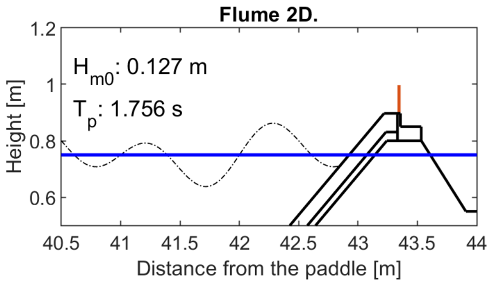

Water level	h	0.75 m
Wave height	H_{m0}	0.127 m
Peak period	T_p	1.76 s
Reflection coefficient	K_r	0.28 [-]
Geometry	$A3$	non-protruding
Model scale q	q_{meas}	0.0853 l/s/m
Prototype q	q_{proto}	18.43 l/s/m

Figure 5.1 and Table 5.1: Summary of parameters describing a non-protruding wave wall test sample with a medium prototype overtopping discharge. Red line showing where the modelled wave overtopping is captured above the protruding wave wall. Note that the water level and structure levels are given relative to the bottom of the flume. The bottom of the flume is not shown.

- Comparison of the modelled and measured reflection coefficients induced by the presence of the rubble mound breakwater (K_r).
- Calibration of the modelled reflection coefficient at wave gauge 5.
- Evaluation of the total surface elevation at wave gauge 5 following the calibration of the incident waves and the reflection coefficient of the structure.
- Evaluation of the average and individual overtopping discharges respectively. First for a non-protruding wave wall case and after for a protruding wave wall case.
- Sensitivity analysis is carried out for a couple of parameters, which influence the overtopping results.

5.3. Calibration of numerical model

Starting point of the calibration/validation work for case A3W1T205 is formed by a rerun of the model set-up by Jacobsen et al. (2018) without making any changes to the numerical settings. This run is referred to as non-calibrated (B1). The surface elevation in front of the structure (wave gauge 5, x = 40.10 m) is depicted in Figure 5.2a. It can be deduced that the modelled wave heights are low compared to the measurements. Figure 5.2b shows the comparison between measured and modelled (B1) surface elevation spectra, where an under-estimation of the modelled wave energy around the peak can be deduced. When comparing H_{m0} to measurements a **13%** under-estimated total wave height is found in wave gauge 5, which was also found by Boersen et al. (2019). The measured total spectral wave height ($H_{m0,meas}$) is 0.134 m and the modelled total spectral wave height ($H_{m0,mod,B1}$) equals 0.116 m.

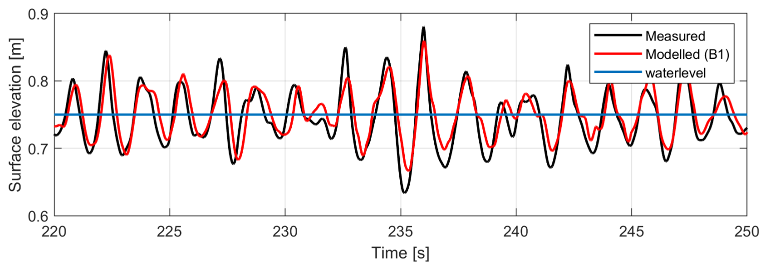

(a) Surface elevation time series.

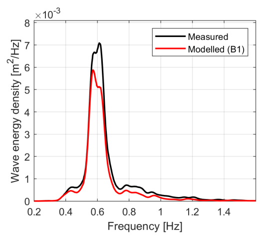

(b) Surface elevation spectrum.

Figure 5.2: (a) Surface elevation captured at wave gauge closest to structure (No. 5), x = 40.10 m, showing the discrepancy in the modelled surface elevation (extreme event) compared to measurements. (b) Comparison between modelled and measured surface elevation spectra, over 500 waves.

CoastalFOAM captures the overtopping quantities over the non-protruding crown wall, as shown in Figure 5.1. When assessing the average overtopping discharge ($q_{mod,B1}$ = 0.073 l/s/m), which is the total captured volume divided by the duration of the time series, a **33%** under-estimation is found compared to what was reported in Chapter 2. A comparison is made between the measured and modelled (B1) cumulative overtopping curves (see Figure 5.3 below), where a model spin-up time of approximately 80 s is taken. The modelled and measured cumulative overtopping curves are compared from the spin-up time onwards, which is done for all further cases. It can be deduced that around 235 to 245 s the largest overtopping event is not modelled. The total modelled surface elevation around this time interval is shown in Figure 5.2a. A discrepancy results in the total modelled surface elevation, under-estimating the wave troughs and crests.

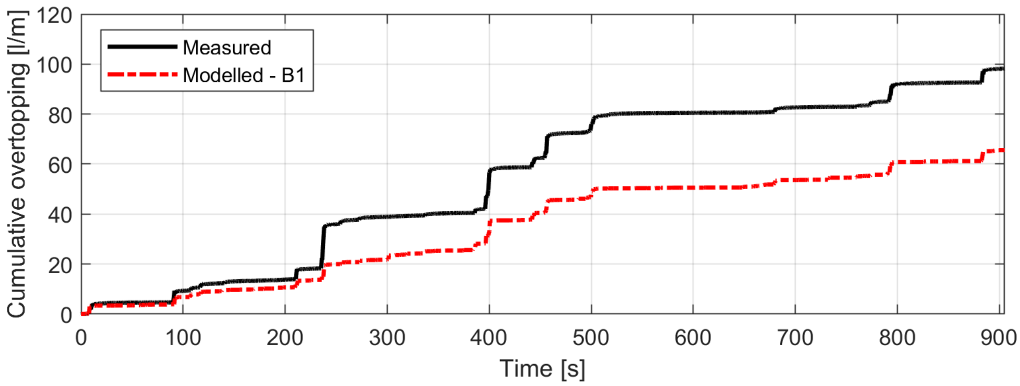

Figure 5.3: Cumulative overtopping results for a non-protruding wave wall and medium overtopping, including a comparison between: physical laboratory measurements and the initial model (B1). Figure based on Boersen et al. (2019).

To understand the cause of the discrepancy of the modelled wave height (influencing the overtopping), the incoming and reflected surface elevations are studied herebelow.

5.3.1. Incoming surface elevation

The 13% under-estimated total spectral wave height can be caused by an under-dimensioned incoming wave height combined with and/or by an erroneously induced reflection by the structure. Therefore, the Zelt and Skjelbreia (1992) method has been used to carry out a reflection analysis and decompose the total modelled surface elevation time series in an incoming and reflective part. The calculated incoming surface elevation is generated using an exterior model, OceanWaves3D (OCW3D; see Section 4.4). However, when comparing (after decomposition) the incoming surface elevation in OpenFOAM with the measured incoming surface elevation time series, multiple discrepancies were identified. The proposed and adopted solutions for the established discrepancies are elaborated in Appendix B. Each discrepancy and solution is given a code A* (A1-A4) and is discussed below. Adopting the proposed solutions to the numerical settings and performing a rerun in OpenFOAM results in four different A* modelled wave conditions. The simulations run for 300 waves (528 seconds, T_p = 1.76 s), enough to compare spectral wave properties.

- (A1) Time shift: the OceanWaves3D files start modelling at 0 s. However, measurements were started when according to the laboratory mechanic the wave conditions were fully developed and started to interact with the structure. The MATLAB "finddelay" function (returning an estimate of the delay via cross correlation between two signals) was used to determine ΔT_{shift}. This was around 30 seconds after the wave paddle motion was initiated. This correction was already applied in Figure 5.2 so that modelled and measured total surface elevations could visually be compared.

- (A2) Time lag: the time steps for which the steering velocities are written out in the physical flume are coarse (0.04 s). Small differences between physically simulated time steps (for example, 0.0401 s) and time steps for which the velocities of the paddle are saved (0.04 s) induce noticeable errors over 1,800 simulated seconds (equaling 45,000 time steps and the induced error over all time steps becomes 45,000*(0.0401-0.0400) = 4.5 s). The MATLAB "finddelay" function was used to determine T_{lag}. The time lag (T_{lag}) was approximately 2·T_p and was corrected by reducing every time step by a small margin $\Delta T = T_{lag}/N_{steps}$. The time lag issue is shown in Figure 5.4, where for increasing modelled seconds the lag between model and measurements increases.

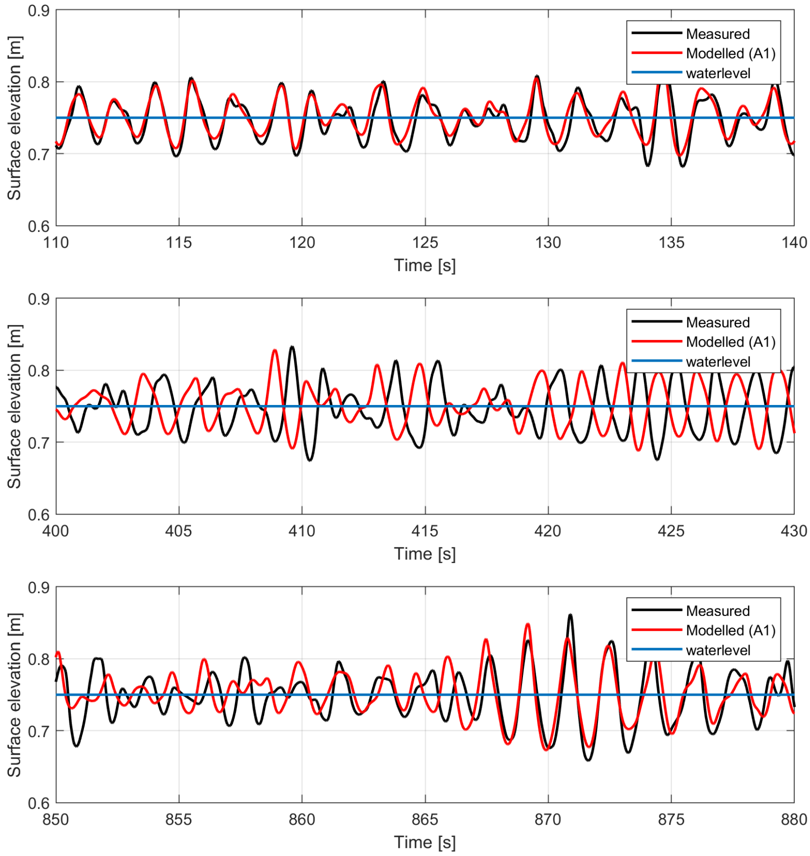

Figure 5.4: Modelled (A1) surface elevation captured at wave gauge (No. 5), x = 40.10 m. Upper plot: no time lag is experienced at 125 s. Middle plot: T_{lag} = 0.85 s is found at 415 s. Lower plot: the lag is enhanced as the simulation is carried further, around 865 s the lag T_{lag} equals 1.72 s.

The A1 and A2 improvements were added to make the modelled signal comparable with measurements.

- (A3) Amplification steering file: as the incoming wave conditions are under-dimensioned compared to the measured incoming wave conditions (difference >5%), the steering file is amplified. In this research a frequency dependent amplification factor is used. This is done because the goal of this research is to validate the overtopping rather than the wave height.

The incoming wave conditions are generated in OceanWaves3D. When comparing the incoming wave conditions of a non-amplified steering file (raw, $H_{m0,i,raw}$ = 0.117 m) in OceanWaves3D with the incoming wave conditions of the measurements ($H_{m0,i,meas}$ = 0.127 m), an under-estimation of 8% is found. It is assumed that for that reason Jacobsen et al. (2018) amplified the steering file with a constant factor ($H_{m0,i,Jacob}$ = 0.121 m). However, in the present research a frequency dependent amplification factor (A3) is applied to the raw steering file, achieving an improved comparability in terms of incoming spectral wave height ($H_{m0,i,A3}$ = 0.127 m). It is important to note that the A1 and A2 modelled wave conditions are adopting the imposed amplification by Jacobsen et al. (2018).

- (A4) OceanWaves3D and OpenFOAM coupling: the coupling between OceanWaves3D and OpenFOAM showed discrepancies in modelling large events, as seen in Figure 5.5. This issue is enhanced when the steering files are amplified, as the modelled wave heights are increased. Increasing the resolution in propagating direction (x-direction) within OceanWaves3D improved the coupling.

The A4 modelled wave conditions contain all the implemented improvements. Now modelled (A4) and measured signals can be compared by means of RMSE (Root mean squared error) and PCC (Pearson correlation coefficient) values.

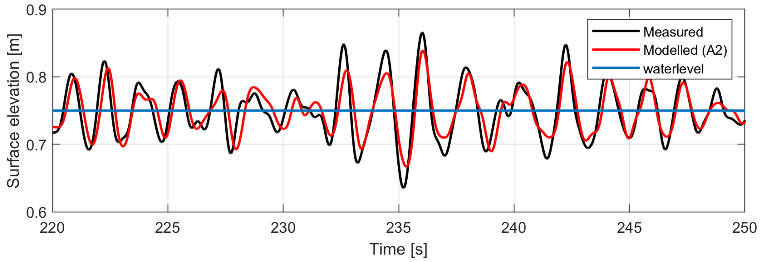

(a) Surface elevation time series.

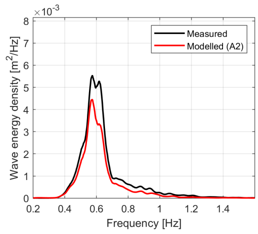

(b) Surface elevation spectrum.

Figure 5.5: (a) Incoming surface elevation captured at wave gauge (No. 5), showing the discrepancy in the modelled (A2) surface elevation (extreme event) compared to measurements. (b) Comparison between modelled (A2) and measured incoming surface elevation spectra, over 300 waves.

Intermezzo - RMSE and PCC

The root mean squared error is a statistical parameter, used to quantify the magnitude of the error between two signals. In this research, the RMSE value is obtained between the numerical modelled and the experimental measured surface elevations. Compared signals are identical when the calculated RMSE is equal to zero.

$$\textbf{RMSE} = \sqrt{\frac{\sum_{i=1}^{N}(y_{i,mod} - y_{i,exp})^2}{N}} \tag{5.1}$$

Where N is the number of data points, $y_{i,mod}$ the numerical model output and $y_{i,meas}$ the experimental measured value at the specified data point. The Pearson correlation coefficient describes the correlation between two signals (random variables). The PCC value is obtained between the numerically modelled and the experimentally measured surface elevations. A PCC (ρ) equal to 1 shows that both signals are fully (linearly) correlated.

$$\textbf{PCC} = \frac{\text{cov}(X_1, X_2)}{\sigma_{X_1} \cdot \sigma_{X_2}} \tag{5.2}$$

Where cov is the covariance between two random variables (surface elevations or overtopping discharges) and σ the standard deviation of the studied random variable.

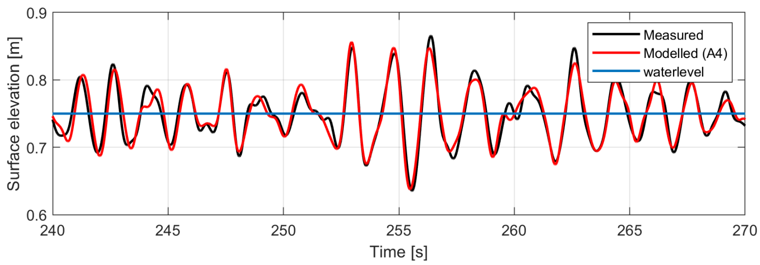

(a) Surface elevation time series.

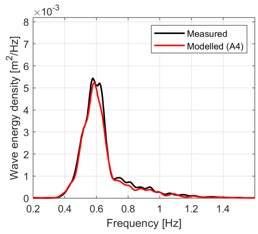

(b) Surface elevation spectrum.

Figure 5.6: (a) Incoming surface elevation captured at wave gauge closest to structure (5), x = 40.10 m, showing the improved (A4) modelled wave conditions. (b) Comparison between modelled (A4) and measured incoming surface elevation spectra, over 300 waves.

Before, due to time lags, the signals could only be compared by means of spectral properties. The modelled (A2 and A4) and measured incoming surface elevation time series and spectra are compared in Figures 5.5 and 5.6. The spectral and statistical comparison is made in Table 5.2.

Type	Total			In			Reflected		
Case	RMSE [m]	PCC [%]	H_{m0} [%]	RMSE [m]	PCC [%]	H_{m0} [%]	RMSE [m]	PCC [%]	H_{m0} [%]
A2	0.0177	88.59	-12.60	0.0160	88.94	-15.38	0.0061	78.89	5.76
A4	0.0146	92.08	-1.14	0.0118	93.61	-4.93	0.0056	85.23	17.14

Table 5.2: Statistical and spectral parameters (RMSE, PCC and H_{m0}) describing the quality of the wave conditions at wave gauge 5, including a comparison between: the original and improved numerical model (A2 and A4) in terms of total, incoming and reflected wave conditions.

The most important addition to the calibration procedure of the numerical model is the improvement in incident surface elevation ($H_{m0,i}$), as a result of the introduced A3 (amplification of steering file) and A4 (improved coupling between OceanWaves3D and OpenFOAM) corrections. This means that the under-estimation decreases from **15%** to about **5%**.

5.3.2. Reflected surface elevation

The reflected spectral wave height represents the amount of wave energy which is reflected back due to the presence of the structure in the physical or numerical flume. Table 5.2 shows that the reflected spectral wave height is over-estimated by 17% compared to the measurements. The aforementioned improvements (A1-A4) increased the accuracy of the model considering the incoming surface elevation. The magnitude of induced reflection by the presence of the structure can be quantified by the reflection coefficient. The reflection coefficient ($K_{r,mod}$ = 0.34 [-]) of the structure is **21%** too high compared to the measured one ($K_{r,meas}$ = 0.28 [-]). The bulk reflection of the rubble mound breakwater depends on various parameters, e.g. Iribarren number, the angle of the slope and the porous flow properties. Since the first two factors cannot be altered as they are set by the geometry of the structure and the incident wave conditions, a closer look is given to the parametrisation by van Gent (1995). Section 4.3.3 described the various equations which are solved every time step to describe the resistance the flow experiences due to the presence of the rubble mound breakwater. The higher the resistance exerted by the skeleton on the incoming flow (waves), the higher the reflected waves ($H_{m0,r}$) will be and therefore the higher the reflection coefficient. The lower the resistance, the more wave energy is transmitted through the breakwater and the lower the reflected waves become. Resistance coefficients a and b (see Equation 4.5, Chapter 4), depend on a set of parameters of which four (n (porosity), α, β and KC) can be adapted with substantiated research. These four parameters are discussed in the upcoming sections.

Porosity

Increasing the porosity lowers both resistance coefficients (a and b), reducing the reflection coefficient. The porosity of all layers in the numerical model initially had been set at 0.40. However, these values were assumed by Jacobsen et al. (2018) and not measured in the physical flume. In this research the approach by the Rock Manual 2007 (CIRIA et al., 2007b) is used (see Equations 5.3 and 5.4 below), providing a methodology to predict the average porosity for different gradings and shape characteristics. The method applies to all bulk-placed granular materials (core, filter and armour). The porosity is estimated based on the grain size distribution parameters, such as the uniformity index n_{RRD} of the Rosin-Rammler (Ros-Ram) curve.

$$n_v = \frac{1}{90} \cdot (e_0) \cdot \arctan(0.645 \cdot n_{RRD}) \cdot \frac{180}{\pi} \tag{5.3}$$

$$n_v = \frac{e}{1+e} \tag{5.4}$$

Where e is the void ratio (volume of voids divided by the volume of solids), e_0 the void ratio associated to the single-size particles of different shapes and n_v the bulk porosity of the granular material. For typically mechanical crushed rock the single-size void ratio (e_0) ranges between 0.92-0.96 and is taken as 0.94 (middle value) here (CIRIA et al., 2007b). The followed procedure and intermediate results can be found in Appendix B. Following the above mentioned methodology, the average bulk porosity of the granular materials is estimated to be:

- n_{Armour} = **0.416** [-]
- n_{Filter} = **0.432** [-]
- n_{Core} = **0.425** [-]

The resulting modelled reflection coefficient ($K_{r,mod}$ = 0.34) differs from the measured reflection coefficient ($K_{r,meas}$ = 0.28). Consequently, other parameters are altered to reduce the bulk reflection of the structure in the numerical flume.

α, β and KC

According to laboratory experiments for stationary and oscillating flow performed by van Gent (1995), the coefficients α and β should be set as 1000 and 1.1 respectively. Furthermore, these coefficients rely on several aspects, e.g. grading, shape, aspect ratio and orientation of the stones. Therefore, it is worth considering different sets of coefficients (α and β). van Gent (1995) reported ranges in which the coefficients should lie (0 to 2780 for α and 0.36 to 1.33 for β).

On the other hand, Losada et al. (2008) mention that under oscillatory flow conditions and waves propagating and breaking over slopes, the α and β values mentioned in literature may not be valid. This is due to the conditions from which these parameters were derived, not considering the wave-structure interaction correctly. Therefore, Losada et al. (2008) compared free surface and pressure time series for waves interacting with a high-mound breakwater considering different α and β values. This approach resulted in the following results: α = 200 and β = 0.8 for the breakwater core, α = 200 and β = 1.1 for the filter layer and α = 200 and β = 0.7 for the armour layer.

Moreover, in OpenFOAM Jensen et al. (2014) addressed the issue by comparing experimental data sets with numerical model outcomes. Different flow regimes and ranges of dimensionless coefficients (α and β) were defined. The Darcy flow regime (laminar) $1 < Re_p < 10$, the Forchheimer flow regime $10 < Re_p < 150$, the transitional flow regime $150 < Re_p < 300$ and the fully turbulent flow regime $300 < Re_p$. The regimes were determined based on the porous Reynolds number and reconstructed with different test configurations. For each of the last three flow regimes a graph was presented, displaying the errors introduced by the numerical model when compared with measured surface elevations, for different combinations of coefficients (see Appendix B). According to Jensen et al. (2014), the set α = 500 and β = 2.0 performed best considering all flow regimes and is therefore tested in the present research. Nonetheless, other sets of coefficients (lying in low error regions) will be selected and tested (see Table 5.3). Both Jensen et al. (2014) and Losada et al. (2008) noticed that in case of turbulent flow the dependency on the turbulent coefficient β is high.

Furthermore, Jacobsen et al. (2018) set the KC parameter to 10,000 eliminating the second term in the equation to determine β (see Section 4.3.3). The influence of KC (oscillating flow) was thus almost completely removed from the porous flow model. However, as the model addresses the interaction between waves and structure, the number is re-introduced in this research. The KC number is calculated according to Equation 4.6 (see Section 4.3.3). The KC values for the non-protruding medium overtopping case are equal to 13.11, 25.04 and 66.78 for armour, filter layer and core respectively.

All the above mentioned sets of coefficients are tested in CoastalFOAM. The simulations performed in OpenFoam are still based on the initial model (B1), which is more efficient to run as the resolution in OceanWaves3D is coarse. This set-up gives insight on how much certain changes/parameters influence the bulk reflection of the structure. The simulations run for 300 waves. The initial case is used as reference case, where the porosity of all layers is set to 0.40, the initial estimated D_{n50} for armour, filter and core according to (Jacobsen et al., 2018) is used and α and β coefficients are set to 1000 and 1.1 respectively. The reference case has a reflection coefficient $K_{r,modelled}$ of 0.35, which is ~ 25% too high ($K_{r,measured}$ = 0.28). Table 5.3 shows the modelled reflection coefficients for various set-ups. It can be concluded that when lowering α or β coefficients the reflection coefficient lowers. This is noticed when comparing the Vanneste and Troch (2015) run with the Losada et al. (2008) run. The KC value is kept constant and α and β (except for the core) are lowered, resulting in a decreased bulk reflection coefficient. On the contrary lowering KC, increases the importance of the second term in determining β and results in an increase of the reflection coefficient. Therefore, when lowering KC from 10,000 to the computed values (different for each case) the other dimensionless coefficients have to be lowered as well. This to ensure that overall the reflection coefficient is reduced.

Losada et al. (2016) performed an extensive literature study on previously performed numerical and experimental studies which tried to capture the porous flow through rubble mound breakwaters. They provided a table which shows that considerable efforts have been made over the past years to understand the porous flow characteristics between waves and structures. However, the wide range of α and β coefficients shows that even today there is still room for improvement when considering the determination of the porous flow dimensionless coefficients. This supports the conclusion that no exact set of coefficients exist, as can also be seen in Table 5.3. The same reflection coefficient can be obtained with different combinations of α, β and KC. The dimensionless coefficients applied by Losada et al. (2008) presently performed best in correctly representing the measured bulk reflection ($K_{r,measured}$ = 0.28) of the structure. This can be inferred from the reported reflection coefficient ($K_{r,mod}$ = 0.28) in Table 5.3, using the set of coefficients proposed by Losada et al. (2008). Combining these coefficients with the adjusted porosities results in the configuration that will be adopted for the evaluation runs.

	Armour			Filter			Core			Total
Case	α [-]	β [-]	KC [-]	α [-]	β [-]	KC [-]	α [-]	β [-]	KC [-]	K_r [-]
Jacobsen et al. (2018)	1,000	1.1	10,000	1,000	1.1	10,000	1,000	1.1	10,000	0.35
Jacobsen et al. (2018) (good coupling)	1,000	1.1	10,000	1,000	1.1	10,000	1,000	1.1	10,000	0.34
Jensen et al. (2014)	500	2.0	10,000	500	2.0	10,000	500	2.0	10,000	0.35
Re-evaluated porosity and D_{n50}	1,000	1.1	10,000	1,000	1.1	10,000	1,000	1.1	10,000	0.35
Losada et al. (2008)	200	0.7	13.11	200	1.1	25.04	200	0.8	66.78	**0.28**
Jensen et al. (2014) (adapted)	0.001	1.1	13.11	0.001	1.1	25.04	250	0.75	66.78	0.29
Vanneste and Troch (2015)	305	1.27	13.11	305	1.27	25.04	1007	0.63	66.78	0.36

Table 5.3: Multiple sets of dimensionless resistance coefficients used in the parametrisation of van Gent (1995), showing that the desired bulk reflection can be obtained using different sets of coefficients.

Degree of openness of wave wall

The influence of the degree of openness of the wave wall on the bulk reflection is also considered. The ventilated boundary (see Chapter 4, Section 4.5) is applied to the front of the wave wall to compensate the over-predictive lift forces. Altering the degree of openness makes the wave wall less/more open and reflects more/less wave energy back. The reference case is simulated with a degree of openness of 0.5% and 3%. This resulted in an difference of less than 1% for the reflection coefficient of the structure. Therefore, this factor is neglected as possible improvement of the overall reflection coefficient.

5.3.3. Total surface elevation

A final simulation (A5) is performed with all the aforementioned improvements (A1-A4 and re-assessed porosities and porous flow dimensionless coefficients). The final modelled wave conditions (A5), intermediate wave conditions (A4) and the initial wave conditions (A2) are compared with measurements, showing that the introduced changes improved the overall wave conditions (total, incoming and reflected). Results are presented in Table 5.4. The reflected wave conditions still show differences higher than 5%, yet they are improved in terms of statistical parameters (PCC and RMSE) and can therefore be accepted.

Type	Total			In			Reflected		
Case	RMSE [m]	PCC [%]	H_{m0} [%]	RMSE [m]	PCC [%]	H_{m0} [%]	RMSE [m]	PCC [%]	H_{m0} [%]
A2	0.0177	88.59	-12.60	0.0160	88.94	-15.38	0.0061	78.89	5.76
A4	0.0146	92.08	-1.14	0.0118	93.61	-4.93	0.0056	85.23	17.14
A5	0.0137	92.94	-3.33	0.0113	94.08	-3.78	0.0048	85.82	-7.00

Table 5.4: Statistical and spectral parameters (RMSE, PCC and H_{m0}) describing the quality of the wave conditions at wave gauge 5, including a comparison between: the numerical model (A2, A4 and A5) in terms of total, incoming and reflected wave conditions.

5.4. Evaluation of medium overtopping cases

5.4.1. Non-protruding wave wall case

The instantaneous overtopping discharge is captured above the non-protruding wave wall. Running the A5 model configuration results in the below presented cumulative overtopping curve (see Figure 5.7). The A5 configuration shows excellent agreement with measurements. The red solid line follows the black line, both increasing simultaneously. Furthermore, the A5 configuration does not miss the large overtopping event between 235-245 s. The reference case ($q_{mod,B1}$ = 0.073 l/s/m) and measurements (q_{meas} = 0.109 l/s/m) are added for comparison. The final modelled average overtopping discharge per meter width ($q_{mod,A5}$) for approximately 500 waves equals 0.108 l/s/m, which is **1%** lower compared to measurements. Furthermore, the obtained reflection ($K_{r,mod}$ = 0.27) is slightly lower (3.6%) than what was measured ($K_{r,meas}$ = 0.28) during the performed experiments.

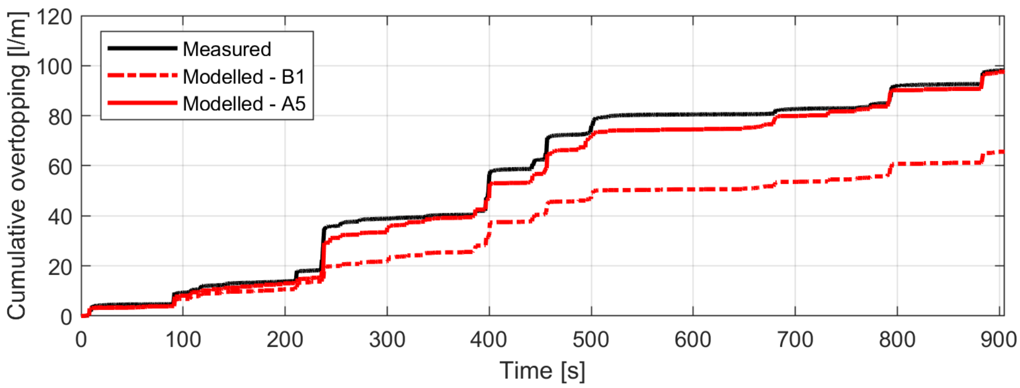

Figure 5.7: Cumulative overtopping results for a non-protruding wave wall and medium overtopping, including a comparison between: physical laboratory measurements, the improved numerical model (A5) and the initial model (B1) set-up.

5.4.2. Protruding wave wall case

The non-protruding wave wall case showed excellent comparison between the measured and modelled average overtopping discharge. Consequently, for the same wave and water level conditions, also a good comparison is expected when adding a protruding wave wall on top of the breakwater. The numerical model parameters are now fixed and the presented calibration procedure is followed. A summary of parameters is given in Figure 5.8 and Table 5.5.

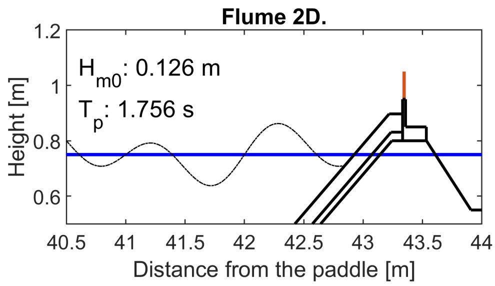

Water level	h	0.75 m
Wave height	H_{m0}	0.126 m
Peak period	T_p	1.756 s
Reflection coefficient	K_r	0.28 [-]
Geometry	$A1$	protruding
Model scale q	q_{meas}	0.0248 l/s/m
Prototype q	q_{proto}	5.37 l/s/m

Figure 5.8 and Table 5.5: Summary of parameters describing a protruding wave wall test sample with a medium prototype overtopping discharge. Red line showing where the modelled wave overtopping is captured above the protruding wave wall.

The quality of the modelled wave conditions (A5) is compared to the physical laboratory experiments in Table 5.6 below. Comparing the obtained results from Table 5.6 with the non-protruding wave conditions in Table 5.4, it can be concluded that the presence of the protruding wave wall has increased the reflected spectral wave height ($H_{r,mod}$). The under-estimation of the reflected spectral wave height decreased from -7% to -5.7%.

Type		Total			In			Reflected	
Case	RMSE [m]	PCC [%]	H_{m0} [%]	RMSE [m]	PCC [%]	H_{m0} [%]	RMSE [m]	PCC [%]	H_{m0} [%]
A5	0.0149	91.68	-3.80	0.0123	93.14	-4.01	0.0049	85.97	-5.73

Table 5.6: Statistical and spectral parameters (RMSE, PCC and H_{m0}) describing the quality of the wave conditions at wave gauge 5, including a comparison between: the improved numerical model (A5) in terms of total, incoming and reflected wave conditions.

When considering the incoming wave conditions, one would expect that the incident wave height would be equal in both cases (as an identical steering file is used). However, a small dissimilarity is seen. The non-identical total surface elevation combined with the adopted reflection analysis method can introduce such small differences. The total modelled spectral wave height decreased, which is mainly caused by the reduction of the incoming wave conditions from -3.8% to -4.0%.

Figure 5.9 shows the comparison between the A5 modelled cumulative overtopping curve and measurements. Between 0 and 500 seconds an excellent comparability is found, represented by almost matching lines. However, the difference between the measured (q_{meas} = 0.033 l/s/m) and modelled overtopping quantities ($q_{mod,A5}$ = 0.043 l/s/m) is larger compared to the non-protruding case. The measured average overtopping discharge is over-estimated by **27.7%**. It can therefore be concluded that the cause lies in some overtopping events which have been modelled, but not measured (see Figure 5.9). Additionally, the obtained reflection ($K_{r,mod}$ = 0.28) can be considered equal to what was measured ($K_{r,meas}$ = 0.28) during the performed experiments.

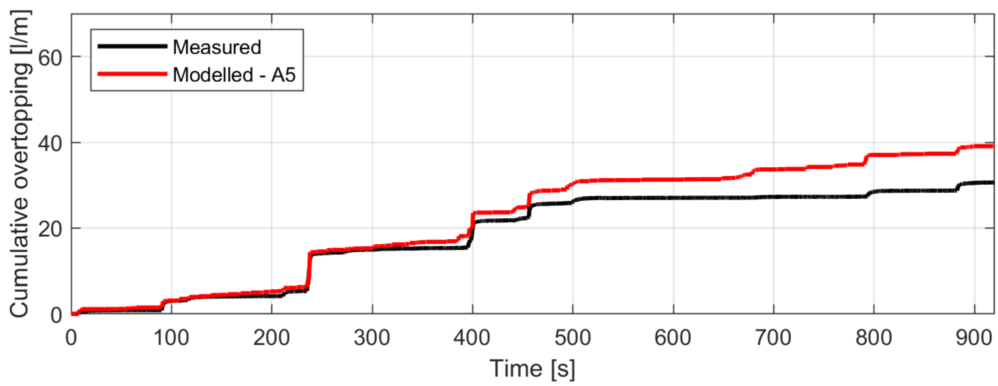

Figure 5.9: Cumulative overtopping results for a protruding wave wall and medium overtopping, including a comparison between: physical laboratory measurements and the improved numerical model (A5).

Over the whole considered time series small overtopping events, referred to as overtopping discrepancies, are captured within the numerical model, resulting in sloping lines instead of horizontal lines (e.g. between 120-240 s and 240-400 s). Several causes can be identified:

- Wave conditions: discrepancies between modelled and measured total surface elevation time series at wave gauge 5, caused by a combination of:
  - The incoming surface elevation time series, generated using the exterior OceanWaves3D model. The frequency dependent amplification factor applied to the incoming wave conditions (see the calibration procedure in Section 5.3.1) improved the comparison in terms of incoming spectral wave height ($H_{m0,i}$) between the model and measurements. However, small differences still arise between the measured and modelled incoming surface elevation time series (see Figure 5.6a, Section 5.3.1).
  - The reflected surface elevation time series, which depends on the porous flow properties (reflection) of the breakwater. If the reflection induced by the breakwater is different from what is experienced in the physical flume, a different reflected surface elevation is captured at wave gauge 5.

Differences in the captured total surface elevation at wave gauge 5 could result in dissimilarities in overtopping discharges.

- Porous flow coefficients: the chosen coefficients (n (porosity), α, β and KC) in Section 5.3.2 directly influence the overflow, wave breaking patterns and therefore the overtopping. The influence on the overtopping is studied in Section 5.5.2. Nevertheless, the porous flow coefficients were chosen based on a comparison of modelled and measured reflection coefficients (based on spectral wave heights H_{m0}), not considering overflow over the breakwater.

- Degree of openness of the wave wall: a ventilated boundary is applied to the front of the wave wall, characterised by a degree of openness. A low degree of openness means that the wave wall is less permeable. As a consequence more water is pushed in upward and backward direction, which results in more wave overtopping and an increase in bulk reflection. The influence of the openness of the wave wall on the average overtopping discharge is discussed in Section 5.5.3.

- Numerical diffusion in the overtopping region due to grid size: small overtopping events can be over-estimated when a coarse grid is applied in the capturing region (above wave wall). Small drops of water can be stretched out over the coarse cell, over-estimating the initial volume of the drop. This cause is further elaborated in Section 5.5.4.

However, without flow measurements over the crest of the breakwater the first cause can not be substantiated and is left for future research. The last three are addressed in the sensitivity analysis. It is worth noting that the first two causes and the last cause also apply to the non-protruding wave wall cases.

5.4.3. Evaluation of individual overtopping events

In previous sections the cumulative overtopping curves were compared in terms of average discharges. Here, the individual modelled and measured overtopping events for both non-protruding and protruding wave wall samples are compared; results are shown in Tables 5.7 and 5.8. The six largest measured individual overtopping events (O1-O6; see Figure 5.10) are compared in magnitude with model outcomes.

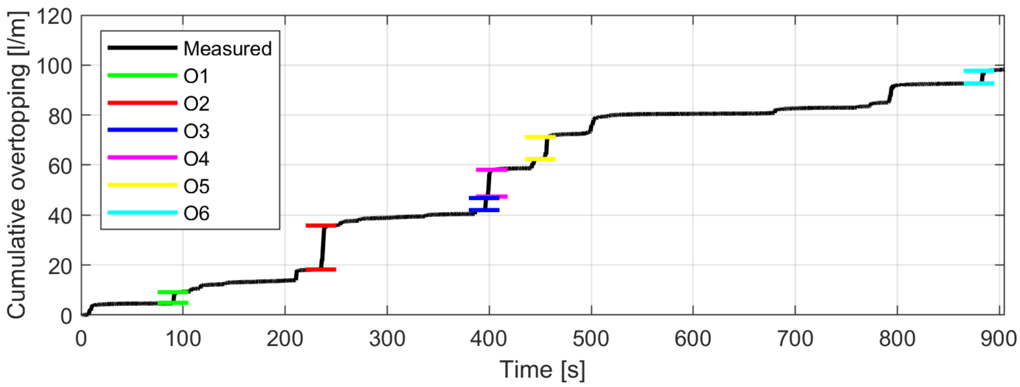

Figure 5.10: Cumulative measured overtopping results for a non-protruding wave wall and medium overtopping, showing the six considered individual overtopping events.

Non-protruding wave wall

The A5 configuration shows improved results compared to the initial B1 configuration in case of a non-protruding wave wall (see Table 5.7). The individual volumes are under-estimated (**14%**) in the non-protruding wave wall case. Yet, the average overtopping discharge (see Section 5.6) showed excellent agreement with the measurements. In regions where the measurements show no overtopping events, the model captures very small overtopping events (overtopping discrepancies), which compensate the under-estimated individual volumes.

Event	$T_{interval}$ [s]	$V_{measured}$ [l/m]	$V_{mod,B1}$ [l/m]	Error [%]	$V_{mod,A5}$ [l/m]	Error [%]
O1	91 - 95	4.4	2.4	-45.5	3.8	-13.6
O2	237 - 241	12.6	4.5	-64.3	11.3	-10.3
O3	396 - 399	5.2	2.9	-44.2	3.6	-30.8
O4	399 - 402	9.5	5.8	-38.9	5.8	-38.9
O5	455 - 459	6.2	3.8	-38.7	5.6	-9.7
O6	882 - 886	5.1	3.5	-31.4	6.0	+17.6
Mean	-	-	-	**-43.8**	-	**-14.3**
Std	-	-	-	**±10.2**	-	**±17.9**

Table 5.7: Individual overtopping volumes (O1-O6) for the non-protruding wave wall with medium prototype overtopping case, including a comparison between: the measurements, the initial model (B1) and the improved model (A5) set-up.

Protruding wave wall

The A5 configuration shows good comparability with measurements, under-estimating the individual volumes by **4%** (see Table 5.8). The protruding wave wall average overtopping discharge was over-estimated (see Section 5.4.2). This over-estimation is caused by a combination of under-estimated individual volumes which are compensated by small overtopping discrepancies, as discussed for the non-protruding wave wall case. However, the relative importance of these small overtopping discrepancies increases as the average overtopping discharge decreases due to the presence of the protruding wave wall. Consequently, the average overtopping discharge for the protruding wave wall case is over-estimated.

Event	$T_{interval}$ [s]	$V_{measured}$ [l/m]	$V_{mod,A5}$ [l/m]	Error [%]
O1	91 - 95	1.9	1.4	-26.3
O2	237 - 241	6.7	6.3	-6.0
O3	396 - 399	1.8	1.7	-5.6
O4	399 - 402	3.9	3.4	-12.8
O5	455 - 459	2.5	2.8	12.0
O6	882 - 886	1.3	1.5	15.4
Mean	-	-	-	**-3.9**
Std	-	-	-	**±14.2**

Table 5.8: Individual overtopping volumes (O1-O6) for the protruding wave wall with medium prototype overtopping case, including a comparison between: the measurements and the improved model (A5) set-up.

5.5. Sensitivity analysis

Each input parameter influences the overtopping results by a certain degree. Three uncertain parameters are studied below: the D_{n50} of the core of the breakwater, the porous flow resistance coefficients (α, β and KC) and the degree of openness of the wave wall. Additionally, the numerical diffusion in the overtopping region is addressed.

5.5.1. D_{n50} of the core

For the physical model construction, four different batches were used to built up the core of the breakwater in the physical flume. Each batch is characterised by a grading curve and a D_{n50} (see Figure 5.11), which relates to varying bulk reflections. Batches 1 and 4 represent both extremities: left and right compared to the average line. The nominal diameters (D_{n50}) for batches 1 and 4 are 5.7 mm and 7.5 mm respectively (D_{n50} = 0.84·D_{50} (CIRIA et al., 2007b)).

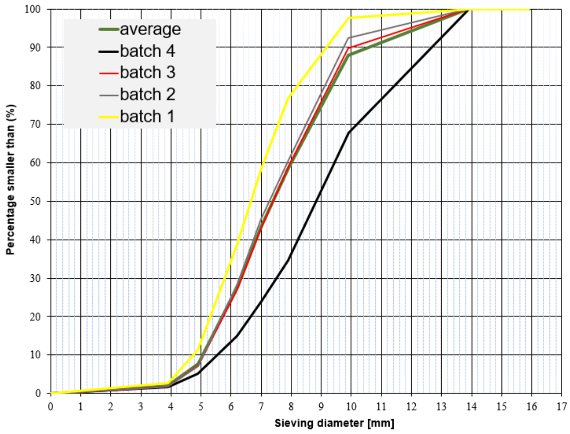

Figure 5.11: Four different batches were used to construct the core of the breakwater in the physical flume. All four sieve curves are plotted against each other. The gradings (D_{n50}) and porosities (n) of batches 1, 4 and average are modelled in OpenFOAM.

Using the same procedure as explained in Section 5.3.2 the found porosities are: n_{Batch1} = 0.430 and n_{Batch4} = 0.417. Three runs are performed in OpenFOAM: batch 1, batch 4 and batch average run. The found reflection coefficients are: $K_{r,average}$ = 0.28, $K_{r,batch1}$ = 0.28 and $K_{r,batch4}$ = 0.27. The average characteristics of the core were used for the calibration runs (see Section 5.3.2 above). The overtopping was modelled during these runs (300 waves). The sensitivity analysis reveals that the discharge is not affected by the value of n and D_{n50} of the considered batches (see Figure 5.12). However, the magnitude of the individual overtopping events showed differences along the three modelled runs.

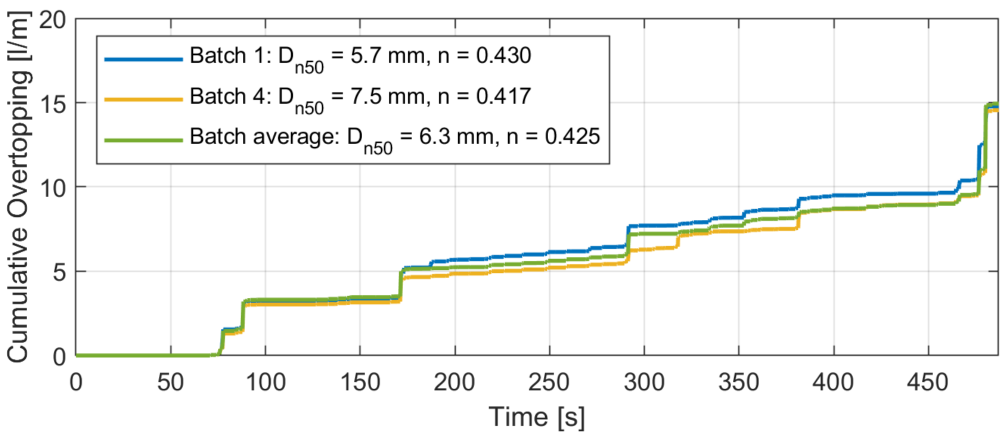

Figure 5.12: Cumulative overtopping results for a non-protruding wave wall and medium overtopping, including a comparison between three numerical model runs (batch 1, batch 4 and batch average) with varying core characteristics (D_{n50} and n).

5.5.2. Porous flow resistance coefficients

As shown earlier in Section 5.3.2 the dimensionless porous flow coefficients do influence the bulk reflection of the breakwater. Additionally, the wave and flow properties in front (e.g. wave breaking) and over the breakwater are also influenced by the choice of dimensionless porous flow coefficients. Numerous runs were done with varying dimensionless porous flow coefficients (see Section 5.3.2, Table 5.3 above). The cumulative overtopping curves of the performed runs are reported in Figure 5.13.

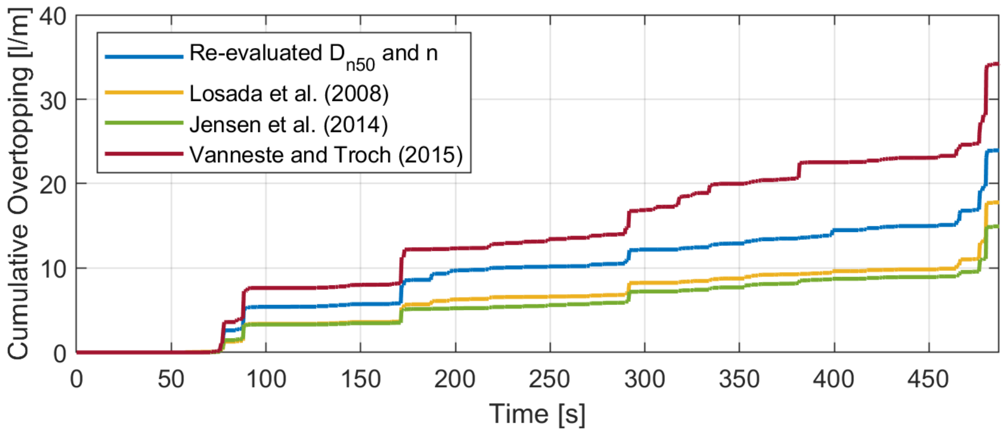

Figure 5.13: Cumulative overtopping results for a non-protruding wave wall and medium overtopping, including a comparison between four numerical model runs with varying porous flow coefficients (α and β) and KC).

The original Jacobsen et al. (2018) run was left out for comparison since no change was made to the dimensionless resistance coefficients compared to the re-evaluated D_{n50} and n run, where α = 1,000, β = 1.1 and KC = 10,000. The remaining runs (see Figure 5.13) were performed using varying α and β coefficients, keeping KC constant (which was calculated using Equation 4.6; see Chapter 4, Section 4.3.3). Comparing the Losada et al. (2008) run with the Vanneste and Troch (2015) run reveals the influence of changing α and β coefficients on the cumulative overtopping curve (as KC is unchanged). It can be deduced that for increasing bulk reflection of the breakwater (less permeable) the average overtopping discharge increases. The highest reflection coefficient was found using the proposed coefficients by Vanneste and Troch (2015) (K_r = 0.36), showing the highest average overtopping discharge ($q_{Vanneste}$ = 0.07 l/s/m). As the breakwater is made less permeable, the flow of water over the crest of the breakwater is less capable to seep through the armour, filter layer and the core, which results in higher overtopping quantities. The re-evaluated D_{n50} and n run (K_r = 0.35) has a similar bulk reflection to the Vanneste and Troch (2015) run. Nonetheless, the average overtopping discharge (q_{Dn50} = 0.05 l/s/m) is different. On the other hand, the Losada et al. (2008) and Jensen et al. (2014) runs show the same comparability in terms of bulk reflection and similar average overtopping discharges. This shows how sensitive the dimensionless porous flow coefficients are in correctly capturing the overflow and eventually the wave overtopping over breakwaters.

5.5.3. Openness of the wave wall

Here, the sensitivity of the degree of openness of the wave wall is analysed. The degree of openness of the wave wall was introduced by Jacobsen et al. (2018) to compensate the over-predicted lift forces due to air entrapment upon wave breaking (see Section 4.5). Jacobsen et al. (2018) performed the validation of forces using values ranging between 0.5-6% and concluded that the 3% performed best. Here, two protruding wave wall cases are modelled in OpenFOAM with varying degree of openness of the wave wall (lower limit 0.5% and the optimal 3%). Two cases were esteemed enough to test the sensitivity of this parameter on the cumulative overtopping curve. As shown in Figure 5.14 below, it can be concluded that a lower degree of openness (red line) results in a higher average overtopping discharge (42.7% higher). The front wall is made less permeable (from 3% to 0.5%), which pushes the water flow in upward direction as the flume is two dimensional. The latter causes the increase in individual overtopping volumes.

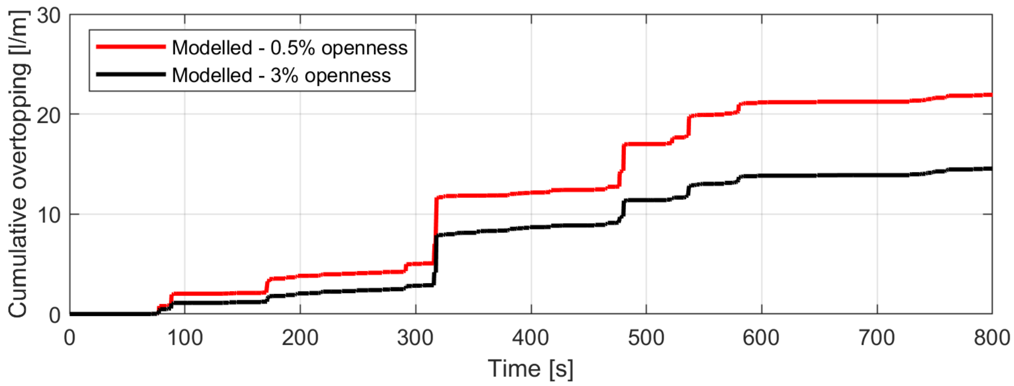

Figure 5.14: Cumulative overtopping results for a protruding wave wall and medium overtopping, including a comparison between two numerical model runs with varying degree of openness of wave wall (0.5% and 3% degree of openness).

5.5.4. Numerical Diffusion

Using coarse meshes (overtopping region) to model small (splashes) overtopping events can induce numerical diffusion. The water droplets are smaller than the considered grid cell and are stretched out over the cell. The relative importance of these overtopping discrepancies increases with: lower average overtopping discharges and protruding wave wall cases. The presence of the protruding wave wall, upon which the overflow impacts, generates splashes which are over-estimated due to the coarse grid. This increases the amount of small overtopping events compared to non-protruding wave wall cases and partly explains the over-estimations found for the protruding wave wall case compared to the non-protruding wave wall case. Considering all the aforementioned, a protruding small prototype overtopping case is expected to show the largest effect of this numerical diffusion. In this section an extra run is performed where the grid size resolution is increased (3x in the overtopping region, from 0.0125 m to 0.0016). From figure 5.15 below it can be inferred that, compared to measurements, the numerical model with refined overtopping region showed a reduction in overtopping discrepancies, visible between 100 and 200 seconds. However, the computational effort required to cope with the higher grid size resolution increased with a factor 2.3x (from 61 hours to 141 hours), which is not desired. Therefore, the aforementioned over-estimation of small overtopping events is accepted for medium and large prototype overtopping cases. To model small overtopping cases (both non-protruding and protruding) it is recommended to use an adequate grid in the overtopping region. Yet, due to time constraints, this was not carried out in the present research for the small overtopping cases.

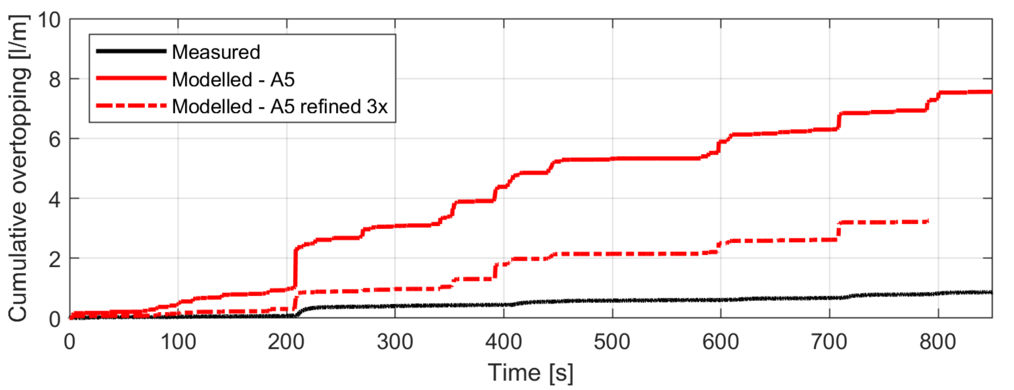

Figure 5.15: Cumulative overtopping results for a protruding wave wall and small overtopping, including a comparison between: the improved numerical model (A5) and the improved numerical model with an increased resolution (3x) in the overtopping region and measurements.

5.6. Evaluation of large overtopping cases

5.6.1. Non-protruding wave wall case

In Section 5.3 above a calibration procedure was proposed based on a medium non-protruding prototype overtopping discharge case. Here, the calibration procedure is evaluated for a large non-protruding wave wall prototype overtopping discharge case. The wave conditions and geometry are shown in Figure 5.16 and Table 5.9.

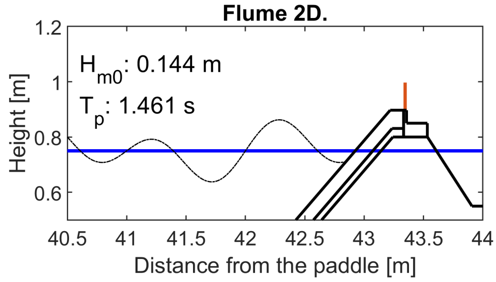

Water level	h	0.75 m
Wave height	H_{m0}	0.144 m
Peak period	T_p	1.461 s
Reflection coefficient	K_r	0.21 [-]
Geometry	$A3$	non-protruding
Model scale q	q_{meas}	0.194 l/s/m
Prototype q	q_{proto}	42.181 l/s/m

Figure 5.16 and Table 5.9: Summary of parameters describing a non-protruding wave wall test sample with a large prototype overtopping discharge. Red line showing where the modelled wave overtopping is captured above the non-protruding wave wall.

The comparison between modelled and measured wave conditions is given in Table 5.10. A comparable accuracy compared to the calibration case is attained, except for the reflected wave conditions which over-estimate the measurements. This is in line with the modelled reflection coefficient ($K_{r,mod}$ = 0.22), which is higher (4.8%) than measured ($K_{r,meas}$ = 0.21).

Type	Total			In			Reflected		
Case	RMSE [m]	PCC [%]	H_{m0} [%]	RMSE [m]	PCC [%]	H_{m0} [%]	RMSE [m]	PCC [%]	H_{m0} [%]
A5	0.0166	90.56	-1.77	0.0139	92.46	-2.90	0.0050	79.46	1.33

Table 5.10: Statistical and spectral parameters (RMSE, PCC and H_{m0}) describing the quality of the wave conditions following the proposed validation process, for a non-protruding test sample with a large prototype overtopping discharge.

The modelled average overtopping discharge per meter width ($q_{mod,A5}$) for approximately 500 waves equals 0.210 l/s/m, which is **2.5%** higher compared to measurements (q_{meas} = 0.205 l/s/m), as shown in Figure 5.17.

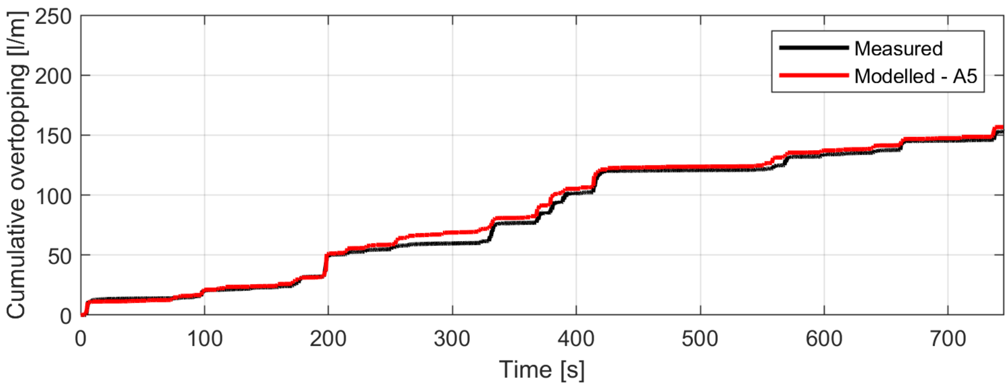

Figure 5.17: Cumulative overtopping results for a non-protruding wave wall and large overtopping, including a comparison between: physical laboratory measurements and the improved numerical model (A5).

From Figure 5.17 it can be inferred that the model is capable of modelling large prototype overtopping discharges for the breakwater with non-protruding wave wall. An excellent comparison is seen between the A5 configuration and the measured cumulative overtopping line over the whole time series, meaning that the individual events are well captured by CoastalFOAM. However, the model captures small overtopping events which are not measured between 220-320 seconds. As mentioned in Section 5.4.2 above these discrepancies can be caused by various factors. Being the influence on the overall result limited, this is accepted.

5.6.2. Protruding wave wall case

A protruding test sample with a large prototype overtopping discharge, characterised by the following geometrical and hydraulic parameters (see Figure 5.18 and Table 5.11) is presented and analysed herebelow.

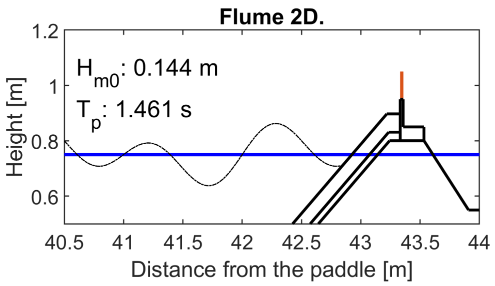

Water level	h	0.75 m
Wave height	H_{m0}	0.144 m
Peak period	T_p	1.461 s
Reflection coefficient	K_r	0.22 [-]
Geometry	$A1$	protruding
Model scale q	q_{meas}	0.052 l/s/m
Prototype q	q_{proto}	11.32 l/s/m

Figure 5.18 and Table 5.11: Summary of parameters describing a protruding wave wall test sample with a large prototype overtopping discharge. Red line showing where the modelled wave overtopping is captured above the protruding wave wall.

The statistical and spectral comparison between model and measurements is reported in Table 5.12.

Type	Total			In			Reflected		
Case	RMSE [m]	PCC [%]	H_{m0} [%]	RMSE [m]	PCC [%]	H_{m0} [%]	RMSE [m]	PCC [%]	H_{m0} [%]
A5	0.0173	89.87	-2.04	0.0145	91.55	-3.10	0.0049	80.16	2.22

Table 5.12: Statistical and spectral parameters (RMSE, PCC and H_{m0}) describing the quality of the wave conditions following the proposed validation process, for a protruding test sample with a large prototype overtopping discharge.

The modelled reflection coefficient ($K_{r,mod}$ = 0.22) is equal when compared to measurements ($K_{r,meas}$ = 0.22). An increase in reflected spectral wave height, caused by the protruding wave wall, is seen in Table 5.12. The under-estimation of the total spectral wave height increased as the incoming spectral wave height further reduced, which weights more than the increase in reflected spectral wave height. One would expect that the incident wave height would be equal in both cases (as an identical steering file is used). However, a non-identical total surface elevation combined with the adopted reflection analysis method (using LWT in intermediate water) can introduce such small differences.

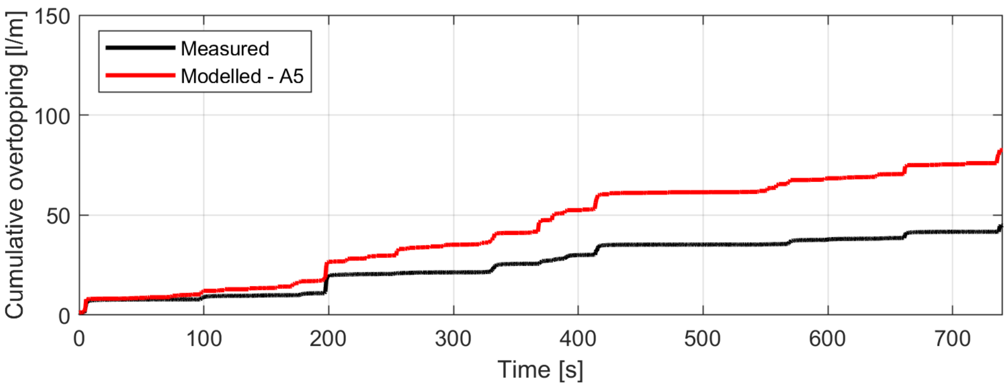

Figure 5.19: Cumulative overtopping results for a protruding wave wall and large overtopping, including a comparison between: physical laboratory measurements and the improved numerical model (A5).

The modelled average overtopping discharge per meter width ($q_{mod,A5}$; see Figure 5.19 above) for approximately 500 waves equals 0.110 l/s/m, which is **85.1%** higher compared to measurements

(q_{meas} = 0.059 l/s/m). The modelled cumulative overtopping line shows good agreement with the measurements. However, the previously addressed erroneous overtopping events between 220 to 320 s are also visible in this case. It is worth noting that their relative importance and number increased by the presence of the protruding wave wall, as previously discussed in Section 5.5.4, and eventually leads to the seen over-estimation of the average overtopping discharge.

5.7. Evaluation of small overtopping cases

5.7.1. Non-protruding wave wall case

In this section the calibration procedure is carried out for a small non-protruding wave wall prototype overtopping discharge case, characterised by the following geometrical and hydraulic parameters (see Figure 5.20 and Table 5.13).

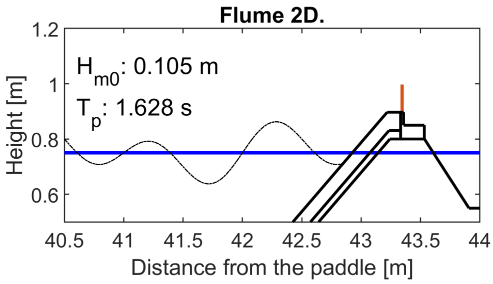

Water level	h	0.75 m
Wave height	H_{m0}	0.105 m
Peak period	T_p	1.628 s
Reflection coefficient	K_r	0.25 [-]
Geometry	$A3$	non-protruding
Model scale q	q_{meas}	0.052 l/s/m
Prototype q	q_{proto}	2.11 l/s/m

Figure 5.20 and Table 5.13: Summary of parameters describing a non-protruding test sample with a small prototype overtopping discharge. Red line showing where the modelled wave overtopping is captured above the non-protruding wave wall.

The quality of the modelled wave climate compared to measurements is reported in Table 5.14.

Type	Total			In			Reflected		
Case	RMSE [m]	PCC [%]	H_{m0} [%]	RMSE [m]	PCC [%]	H_{m0} [%]	RMSE [m]	PCC [%]	H_{m0} [%]
A5	0.0093	95.10	-5.58	0.068	96.61	-4.90	0.0032	87.85	-6.60

Table 5.14: Statistical and spectral parameters (RMSE, PCC and H_{m0}) describing the quality of the wave conditions following the proposed validation process, for a non-protruding test sample with a small prototype overtopping discharge.

The modelled reflection coefficient ($K_{r,mod}$ = 0.25) is equal than what was measured ($K_{r,meas}$ = 0.25) during the performed experiments. The incoming wave condition is under-estimated by 5%, the accepted limit. The under-estimated reflected and incoming spectral wave height resulted in an overall under-estimated total spectral wave height (-5.6%).

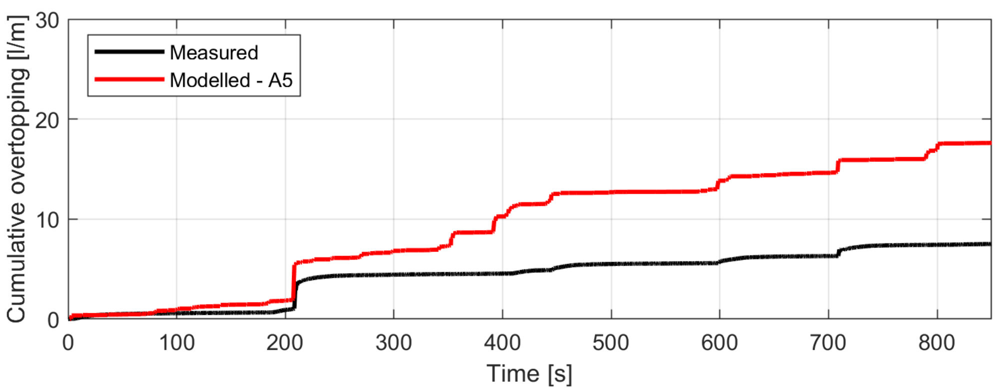

Figure 5.21: Cumulative overtopping results for a non-protruding wave wall and small overtopping, including a comparison between: physical laboratory measurements and the improved numerical model (A5).

The modelled average overtopping discharge per meter width ($q_{mod,A5}$) for approximately 500 waves equals 0.021 l/s/m, which is **110.0%** (approximately x2) higher compared to measurements (q_{meas} = 0.010 l/s/m). It can be inferred that the numerical model (under the A5 configuration) is less capable of modelling small prototype overtopping discharges for non-protruding wave wall cases compared to medium and large non-protruding wave wall overtopping cases, as shown in Figure 5.21 above. A closer look at the cumulative overtopping line shows that the model captures, over the whole time series, multiple overtopping events which are not measured. The lesser capability of the calibrated numerical model in case of small overtopping discharges is mainly caused by the modelled overtopping discrepancies (over the whole time series) rather than large events (modelled correctly around 210 s). It is expected that in the last case (small overtopping with protruding wave wall), the over-estimation will be of larger magnitude as the average overtopping discharge is further reduced and the wave wall protrudes the armour layer (see Section 5.5.4).

5.7.2. Protruding wave wall case

For a protruding small prototype overtopping discharge case, as described by Figure 5.22 and Table 5.15, the comparison between modelled and measured wave conditions is reported in Table 5.16.

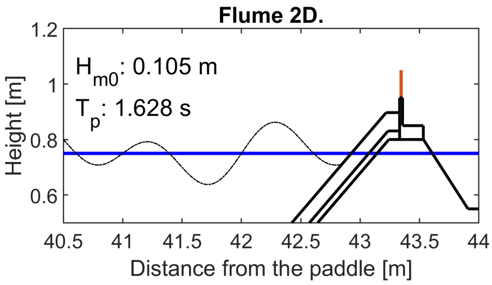

Water level	h	0.75 m
Wave height	H_{m0}	0.105 m
Peak period	T_p	1.628 s
Reflection coefficient	K_r	0.25 [-]
Geometry	$A1$	protruding
Model scale q	q_{meas}	0.0014 l/s/m
Prototype q	q_{proto}	0.30 l/s/m

Figure 5.22 and Table 5.15: Summary of parameters describing a protruding test sample with a small prototype overtopping discharge. Red line showing where the modelled wave overtopping is captured above the protruding wave wall.

Type	Total			In			Reflected		
Case	RMSE [m]	PCC [%]	H_{m0} [%]	RMSE [m]	PCC [%]	H_{m0} [%]	RMSE [m]	PCC [%]	H_{m0} [%]
A5	0.0103	92.54	-5.06	0.0086	93.43	-4.35	0.0036	84.95	-5.28

Table 5.16: Statistical and spectral parameters (RMSE, PCC and H_{m0}) describing the quality of the wave conditions following the proposed validation process, for a protruding test sample with a small prototype overtopping discharge.

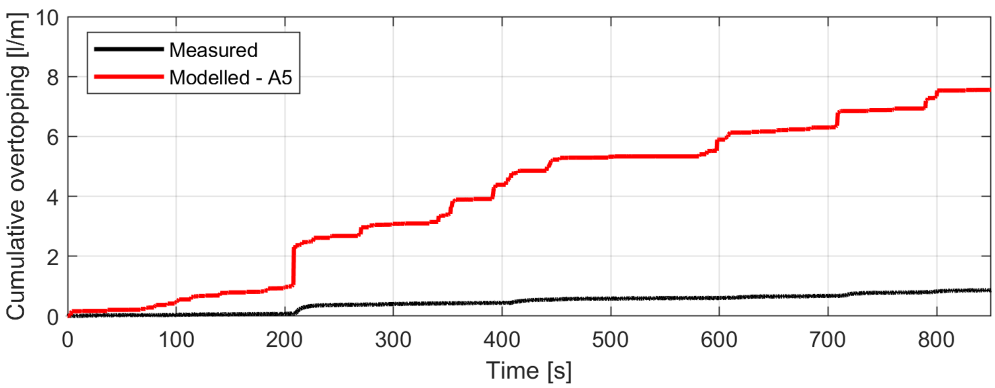

Figure 5.23: Cumulative overtopping results for a protruding wave wall and small overtopping, including a comparison between: physical laboratory measurements and the improved numerical model (A5).

The modelled reflection coefficient ($K_{r,mod}$ = 0.25) is equal to what was measured ($K_{r,meas}$ = 0.25) during the performed experiments. The final modelled average overtopping discharge per meter width ($q_{mod,A5}$; see Figure 5.23 above) for approximately 500 waves equals 0.009 l/s/m, which is **800.0%**

(approximately a factor 9) higher compared to measurements (q_{meas} = 0.001 l/s/m). It can be deduced from the above that the numerical model (under the A5 configuration) is least capable of modelling small prototype overtopping discharges for protruding cases, as Figure 5.23 shows above. The modelled cumulative overtopping curve captures overtopping events where the measurements do not (straight line). As expected, the over-estimation is the most pronounced in this case; the small protruding wave wall overtopping case amounts the lowest average overtopping discharge and is characterised by the presence of the wave wall. The effect of numerical diffusion for this case was illustrated in Figure 5.15 (see Section 5.5.4 above), where the estimated average overtopping (under the A5 - 3x refined configuration) discharge amounted 0.004 l/s/m, which is 311% higher than measured. This is an improvement compared to the earlier mentioned 800%. However, the run is disregarded for future comparison since it consisted of a different grid in the overtopping region compared to other runs and did not account for 500 waves. Nonetheless, from the foregoing it can be concluded that an increased grid resolution is required to accurately model small overtopping protruding wave wall cases at the cost of computational time.

5.8. Summary

Herebelow a summary is given of the obtained numerical model results (CoastalFOAM; considering 500 waves), which are compared with measurements. To compare the results the EurOtop 2018 proposes to plot the relative overtopping rate ($q/(gH_{m0}^3)^{0.5}$) against the relative freeboard (R_c/H_{m0}). The format of Figures 5.24 and 5.25 is based on Figure 6.7 of the EurOtop manual 2018. For the spectral wave height (H_{m0}) the measured incident spectral wave height is used, since the difference in incident spectral wave height between the calibrated numerical model and measurements was minimal.

Non-protruding wave wall

For the non-protruding wave wall cases (see Figure 5.24), CoastalFOAM showed good agreement with measurements.

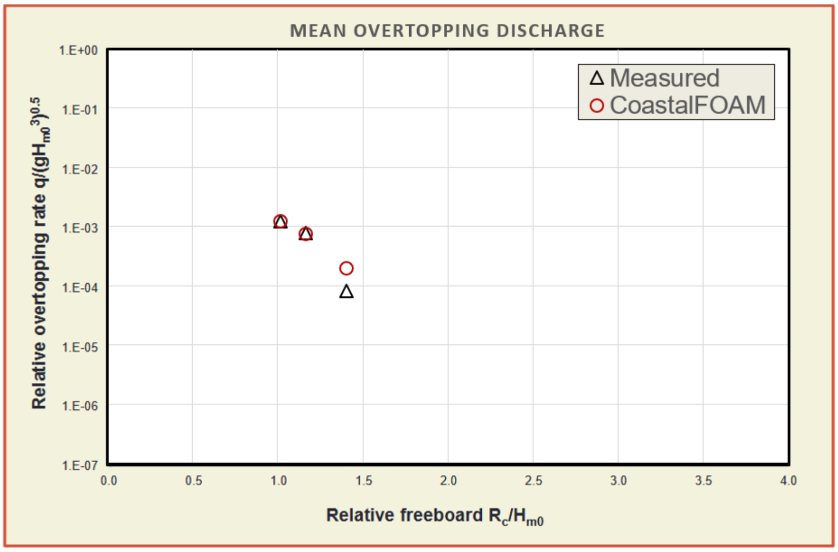

Figure 5.24: Mean overtopping discharge for non-protruding wave wall cases in terms of relative overtopping rate and relative freeboard, including a comparison between: physical laboratory measurements, the improved numerical model (CoastalFOAM).

The calibration procedure from the original model configuration (B1) to the A5 configuration showed improved results in terms of wave conditions, overtopping discharges and individual overtopping volumes for both the medium and large overtopping case. All this resulted in improved comparability with measurements for the medium and large overtopping cases (two left data points) compared to the small overtopping case.

Protruding wave wall

When considering the protruding wave wall cases (see Figure 5.25 below), it can be deduced that CoastalFOAM over-estimated the measurements for all cases. For two (medium and large overtopping) out of three cases the model showed good agreement with measurements. Two causes were worked out for the over-estimated model outcomes compared to measurements:

- The overtopping discrepancies (see Section 5.5.4 above), which became more frequent for protruding wave wall cases and relatively more important for decreasing average overtopping discharge (to the right in Figure 5.25).
- The degree of openness of the wave wall, which has a significant influence on the average overtopping discharge, as seen in Section 5.5 above.

Therefore, when modelling small overtopping with protruding wave wall cases, it is recommended to increase the resolution of the grid in the overtopping region.

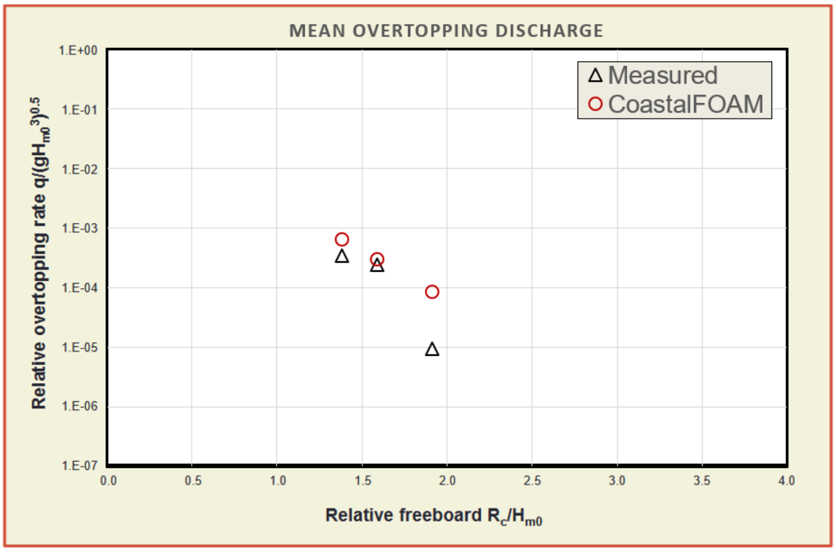

Figure 5.25: Mean overtopping discharge for protruding wave wall cases in terms of relative overtopping rate and relative freeboard, including a comparison between: physical laboratory measurements and CoastalFOAM.

Finally, the accuracy of the calibrated model (CoastalFOAM; A5 model set-up) is evaluated against the accuracy achieved by the uncalibrated version of the numerical model, applied by Boersen et al. (2019), considering the average overtopping discharge as evaluation criterion. Eight overtopping cases were selected and modelled by Boersen et al. (2019). Out of the eight cases, six are selected here for the comparison (small, medium and large overtopping with non-protruding and protruding wave wall cases). The cases modelled by Boersen et al. (2019) are not equal to the ones modelled in this research, hence the reported difference in measured average overtopping discharges in Table 5.17. The comparison is done (see Table 5.17) in terms of RMSE (l/s/m) relative to the measured averages, where the calibrated model shows improved results for both non-protruding and protruding wave wall cases. The RMSE values relative to the measured averages are lower for CoastalFOAM (non-protruding = 0.07, protruding = 0.97) compared to the uncalibrated model (non-protruding = 0.16, protruding = 1.67) for both geometries.

	Non-protruding	Protruding
	[l/s/m]	
Measured average (Boersen et al., 2019)	0.106	0.027
Measured average	0.108	0.031
	RMSE [l/s/m]	
Uncalibrated (Boersen et al., 2019)	0.017	0.045
CoastalFOAM	0.008	0.030

Table 5.17: Measured average discharges and RMSE values when applying the uncalibrated model or CoastalFOAM for the estimation of the average overtopping discharge q, including a separation between protruding and non-protruding wave wall cases.

6

Model application

6.1. Introduction

In this chapter the focus shifts from average overtopping discharges (q), validated in Chapter 5, to maximum overtopping volumes (V_{max}). First, the definitions of extreme wave and overtopping events adopted in the present research are given. Second, the reasoning and the advantages of the proposed shift are explained. Third, a theory is elaborated where the surface elevation of extreme wave events is reconstructed based on spectral wave properties of a given sea state. The following topics will be addressed for clarification: wave focusing, the NewWave theory, its application in the coastal engineering domain and the first order wave generation. Finally, two methodologies are presented in which the NewWave theory is applied numerically (using CoastalFOAM) to assess: maximum overtopping volumes and average overtopping discharges based on the spectral wave properties at the toe of the breakwater.

6.1.1. Extreme wave and overtopping events

In the present research an extreme wave event is defined as: a train of waves containing the highest wave of the considered sea state, which is characterised by its spectral parameters (H_{m0}, T_p and the peak enhancement factor γ). The waves prior to the highest wave are also considered to be part of the extreme wave event. These preceding waves "warm-up" the rubble mound breakwater, i.e. running up and down the slope which reduces the roughness (filling of pores armour or filter layer) for upcoming waves. Furthermore, an extreme overtopping event is defined as: the wave overtopping volume captured during the interaction between the extreme wave event and the rubble mound breakwater.

6.2. Importance of the maximum overtopping volume

In Chapter 5 the numerical model was validated for the reproduction of average overtopping discharges over rubble mound breakwaters. Nevertheless, the average overtopping discharge as a quantity is not capable of identifying extreme overtopping events. It gives the total overtopped volume over the considered period. However, extreme events are likely to cause most of the damage to coastal structures, as suggested by Franco et al. (1994), using the largest individual overtopping volume instead of an average value for design. The EurOtop 2018 manual mentions that most damage close to the hydraulic structure is caused by the largest overtopping volumes. For a given mean overtopping discharge, small waves will produce small overtopping volumes. On the other hand, large waves carry many cubic meters of overtopping water in one wave. Therefore, tolerable limits should also be based on overtopping volumes and not only on tolerable mean discharges.

To highlight this further, the 54 performed laboratory experiments for a protruding and non-protruding wave wall on top of a rubble mound breakwater are shown in Figure 6.1.

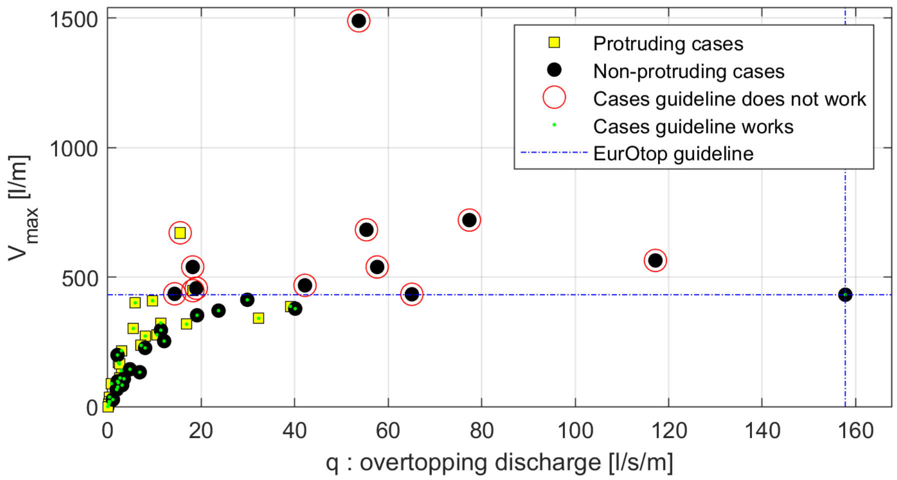

Figure 6.1: Maximum volumes plotted against the average discharges for the respective cases, 27 protruding wave wall cases and 27 non-protruding wave wall cases.

For each case, the measured maximum overtopped volume is plotted against the measured average overtopping discharge. The former is estimated from the available measured cumulative overtopping curves. The maximum vertical increment over a period of $1{\cdot}T_p$ is defined as the maximum overtopping volume (see Figure 6.2).

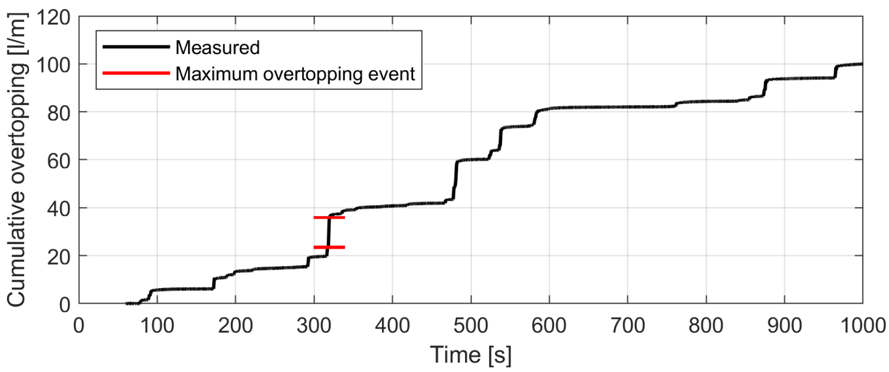

Figure 6.2: Technique to estimate the maximum overtopped volume from the measured cumulative overtopping curves.

According to the EurOtop 2018 guidelines the highest average overtopping discharge would be used to evaluate the height of the rubble mound breakwater. In Figure 6.1, the case with the highest overtopping discharge is visualised by the intersection of the blue dotted lines and is characterised by a H_{m0} = 0.123 m, T_p = 2.26 s with a water level equal to 0.80 m (case A3W1T103 in Table A.1). Nonetheless, the last mentioned case does not contain the highest overtopped volume. Cases with higher maximum overtopped volumes, compared to case A3W1T103, are circled in red as the EurOtop does not consider them for design purposes. Yet, the red circled cases could induce more damage to the rubble mound breakwater.

Two situations can be distinguished when designing a rubble mound breakwater: the Serviceability Limit State (SLS) and the Ultimate Limit State (ULS). The SLS is the design to ensure that the structure is suitable for its use, whereas the ULS is the design to ensure that the structure is safe and does not fail under high loads. In both approaches, the maximum overtopping volume can be used as design standard, admitting that the ULS probably has a higher (acceptable) overtopping volume than the SLS. For the ULS the overtopping volume required to damage the breakwater would be considered. On the other hand, for the SLS the overtopping volume (hydrodynamics) causing pedestrians' their instability when walking over a breakwater can be used, as done by Arrighi et al. (2017) for floodwaters. Instead of looking at a full sea state to assess the individual overtopping volumes (see Chapter 5 above), compact extreme wave and overtopping events will be reproduced and compared with empirical methods and measurements. From a numerical point of view, simulating compact extreme wave events is an attractive solution as it would reduce simulation times. This opens up the possibility to increase the amount of set-ups that could be tested. The generation of extreme wave events is discussed next.

6.3. Focused wave group

Extreme wave events arise due to four different processes: wave-current interaction, wave-bottom interaction (shoaling), wave-wind interaction and wave-wave interaction (i.e. linear superposition and phasing of multiple wave components). The latter process will be considered as wave focusing. The surface elevation can be expressed as a linear superposition of multiple independent harmonic components (see Equation 6.1), at any point in space and time.

$$\zeta(x,t) = \sum_{n=1}^{N} a_n cos(k_n x - \omega_n t + \phi_n) \tag{6.1}$$

Where N is the number of wave components considered to recreate the focused wave group, x is the horizontal distance from the wave paddle, t is time, a_n is the wave amplitude, k_n the wave number, ω_n the angular frequency and ϕ_n the phase of the n^{th} component. In case of an irregular sea state, for each wave component the ϕ_n would be randomly distributed between 0 and 2π. However, in formulating a focused wave group this phase is not random. When the waves are focused at a certain location x_f and time t_f, the phase ϕ_n of each component satisfies Equation 6.2. Combining Equations 6.1 and 6.2 results in Equation 6.3.

$$\phi_n = -k_n x_f + \omega_n t_f + 2m\pi, \qquad m = 0, \pm 1, \pm 2, ... \tag{6.2}$$

$$\zeta(x,t) = \sum_{n=1}^{N} a_n cos(k_n(x - x_f) - \omega_n(t - t_f)) \tag{6.3}$$

Upon focusing, constructive interference occurs among the considered wave components, which results in a large energetic event (extreme wave event). The focusing only occurs at 1 location, namely x_f; at other locations the maximum surface elevation is less. For that reason, the choice of the focus location will be substantiated as it is expected to have a significant influence on the overtopping results.

6.4. The NewWave theory

The NewWave theory by Tromans et al. (1991) opens up the possibility to define the extreme wave event from a wave spectrum. The surface elevation of the extreme wave event created with the NewWave theory is referred to as: NewWave profile. A NewWave profile is consistent with the mathematical description of the expected shape of extreme wave events in a linear random sea, as shown by Jonathan and Taylor (1995).

The underlying statistical theory originates from Lindgren (1970), who described the expected (most probable) shape near an arbitrary crest with a non-linear relation. However, when the crest height is increased (extreme wave events) the Lindgren profile converges to a linear relation, $a \cdot r_i$, which is the scaled auto-correlation function and where r_i is the autocorrelation function for the Gaussian surface in time and a the surface elevation.

This asymptotic solution is applied in this research. The theory is valid when the wave amplitude of the NewWave profile is large compared to the standard deviation of the considered process (surface deviation). According to the NewWave theory the profile is given by the normalised auto-correlation function pre-multiplied with crest height of interest (η_{goal}). The crest-focused NewWave profile time series is given by Equation 6.4 herebelow.

$$\zeta(t) = \eta_{goal} \frac{\sum_n S_n(\omega) \Delta\omega_n cos(\omega_n(t - t_f))}{\sum_n S_n(\omega) \Delta\omega_n} \tag{6.4}$$

Where η_{goal} is the desired amplitude of the NewWave profile at focus location which can be extracted from a wave height distribution fit to measured data, S_n is the variance spectral density of the modelled underlying wave energy spectrum (JONSWAP, Pierson Moskowits or others) and $\Delta\omega_n$ the angular frequency resolution. In Equation 6.4 the numerator is the auto-correlation function, given by the inverse Fourier transform of the underlying spectrum. The denominator is the normalising factor, which is the variance of the considered wave spectrum. By combining Equations 6.3 and 6.4 the individual wave amplitudes a_n can be derived (see Equation 6.5) to obtain a desired NewWave profile at focus location. Filling in these individual wave amplitudes in Equation 6.3 gives the crest-focused NewWave profile time series (see Equation 6.6).

$$a_n = \frac{\eta_{goal} S_n(\omega)\Delta\omega_n}{\sum_n S_n(\omega)\Delta\omega_n} \tag{6.5}$$

$$\zeta(t) = \sum_{n=1}^{N} a_n cos(\omega_n(t - t_f)) = \sum_{n=1}^{N} \frac{\eta_{goal} S_n(\omega)\Delta\omega_n}{\sum_n S_n(\omega)\Delta\omega_n} cos(\omega_n(t - t_f)) = \eta_{goal} \frac{\sum_n S_n(\omega)\Delta\omega_n cos(\omega_n(t - t_f))}{\sum_n S_n(\omega)\Delta\omega_n} \tag{6.6}$$

Several input parameters are therefore needed for the creation of a NewWave event at x_f. The wave amplitudes are based on the underlying spectrum properties. The essential parameters to recreate a NewWave are listed below:

- η_{goal}: the desired surface elevation at focusing point [m]
- γ: peak enhancement factor [-]
- T_p: peak period [s]
- x_f: location of focusing [m]
- t_f: time of focusing [m]
- f_{LC}: lower cut-off frequency [Hz]
- f_{HC}: higher cut-off frequency [Hz]

6.4.1. The NewWave theory in coastal engineering

The NewWave profile has been applied as design wave in the coastal engineering domain. Offshore conditions (wave spectrum) are analyzed and transformed nearshore using numerical models (e.g. SWAN). The nearshore spectral wave properties are used as input for the NewWave theory, generating the NewWave profile. The latter is modelled numerically to study which responses coastal structures (e.g. quay walls; Antonini et al. (2017)) give under extreme conditions. Hofland et al. (2014) created multiple NewWave profiles. They extracted η_{goal} from the probability of exceedance curve of the measured wave heights. The captured overtopping volumes were compared with the measured overtopping volumes. The NewWave profiles caused overtopping volumes which lied within a factor 2 compared to measurements.

Recently Whittaker et al. (2016) demonstrated that the NewWave profile can be adopted in intermediate and shallow waters. However, as waves in intermediate water depth are non-linear, adjustments are added to the NewWave profile, referred to as second order corrections.

Whittaker et al. (2018) studied extreme overtopping events over an inclined seawall on a sloping foreshore. The overtopping due to a NewWave group showed a strong dependence on the focus location, the linear amplitude and the phase of the group at focus.

6.4.2. First order wave generation

The desired NewWave profile at focus location is given by Equation 6.4, while the amplitudes of the wave components in order to recreate the profile by Equation 6.5. Still, as the NewWave profile is to be generated in OceanWaves3D (as input for CoastalFOAM), a wave paddle signal (horizontal velocity time series) is needed to recreate the desired profile. The NewWave profile is transformed to the paddle position with linear wave theory. Thereafter, a first order (linear) wave-maker theory is used to generate the horizontal paddle displacement time series. The followed process is shown in Figure 6.3. A detailed description of the linear wave-maker theory is given by Dean and Dalrymple (1991) and is referred to for more details.

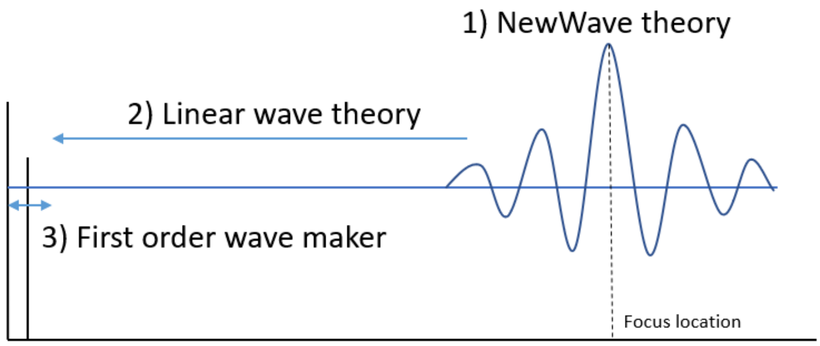

Figure 6.3: Process to achieve the desired NewWave profile at focus location, including: the NewWave theory to compute the NewWave profile at focus location, the linear wave theory to transform the NewWave profile to the paddle and a first order wave generation to produce the necessary steering file.

6.5. Application of the NewWave theory

In the present research the NewWave theory is applied in two different ways:

- (i) methodology to assess the maximum overtopping volume given the spectral properties at the toe of the breakwater.
- (ii) methodology to assess the average overtopping discharge using the maximum overtopping volume as input.

These two applications are explained in the upcoming sections.

6.6. Methodology to assess the maximum overtopping volume (V_{max})

In the presented methodology the NewWave theory is used to create a NewWave profile based on spectral properties at the toe of the breakwater, addressed in Section 6.6.1. The NewWave profile represents the largest event in a given sea state, characterised by its wave spectrum and parameters. The methodology assesses the maximum overtopping volume caused by the interaction of that NewWave profile with the hydraulic structure. The measured incoming spectral properties are used as input parameters for the NewWave profile. This to ensure that the obtained overtopping volumes are comparable with the maximum measured overtopping volumes for validation purposes. The methodology is applied to 18 cases; non-protruding and protruding wave wall with a water depth (h) of 0.75 m (A3W1T201-A3W1T209 & A1W1T201-A1W1T209; see Appendix A). The required input parameters (see Section 6.4 above) for the NewWave profile are derived from the measurements. After this, the NewWave profile is modelled in OCW3D, where a comparison is made between the theoretical profile and the NewWave profile generated in OCW3D. Several iterations are required to ensure that the η_{goal} and the focus location x_p obtained in OCW3D are equal to the desired input values. Finally, the NewWave profile is modelled in CoastalFOAM to account to model the overtopping over the breakwater.

The followed methodology is summarized in a flowchart (as shown in Figure 6.4), and can be applied in cases where the designer chooses the maximum overtopping volume as design criterion (first step). All the proposed steps on the left and right of the orange box are steps required to recreate a NewWave profile which can be validated with measurements. The orange box represent the reproducable methodology, where the input parameters for the NewWave profile are derived and chosen and the maximum overtopping volume is obtained as output. To guide the reader trough the methodology, the respective steps are illustrated below in different sections.

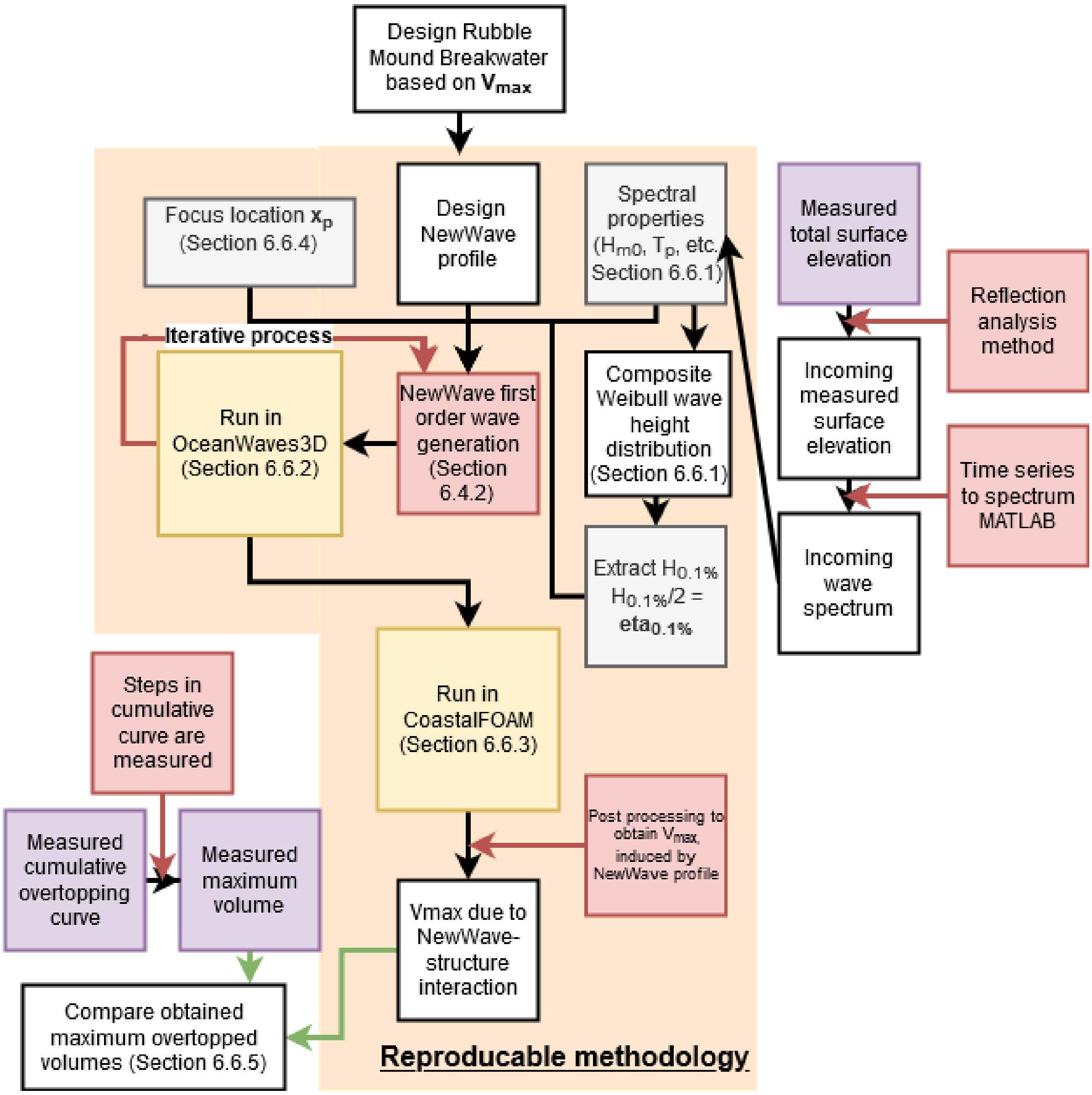

Figure 6.4: Flowchart representing the followed methodology in order to obtain $V_{max,NewWave}$ for each case which is compared to $V_{max,measured}$. Red colour representing MATLAB procedures, yellow numerical modelling in CoastalFOAM, purple measurements and gray input parameters for the NewWave model.

6.6.1. Input parameters

The NewWave profile will be constructed for nine cases, each based on the measured incoming wave conditions. The latter are obtained using the Zelt and Skjelbreia (1992) reflection analysis method, with 5 wave gauges. The incoming surface elevation time series are transformed to wave spectra, from which spectral properties, such as H_{m0}, T_p, f_{LC} and f_{HC}, can be extracted (see Figure 6.5).

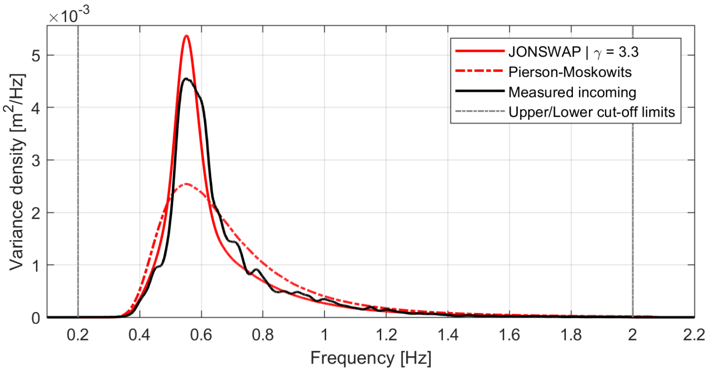

(a) Spectrum of incoming wave signal.

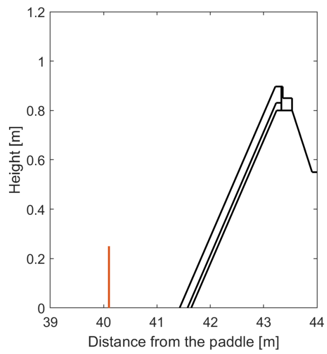

(b) Location of interest.

Figure 6.5: (a) Showing two possible spectrum fits applied to the incoming wave spectrum, where the JONSWAP (γ = 3.3) showed a good comparison with the measured incoming spectrum. Grey lines showing the threshold cut-off limits f_{LC} and f_{HC}. (b) Location where the incoming measured wave spectrum was captured (wave gauge 5).

The peak enhancement factor is one of the required input parameters for the NewWave theory. It can be inferred that the JONSWAP fit shows good resemblance with the incoming surface elevation spectrum (case A3W1T205; see Appendix A). This resemblance is seen for all cases (see Section C.1, Appendix C). Therefore, a peak enhancement factor equal to 3.3 is chosen to construct the NewWave profiles (JONSWAP type), creating a wider extreme event compared to a Pierson-Moskowits spectrum (see Figure 6.6).

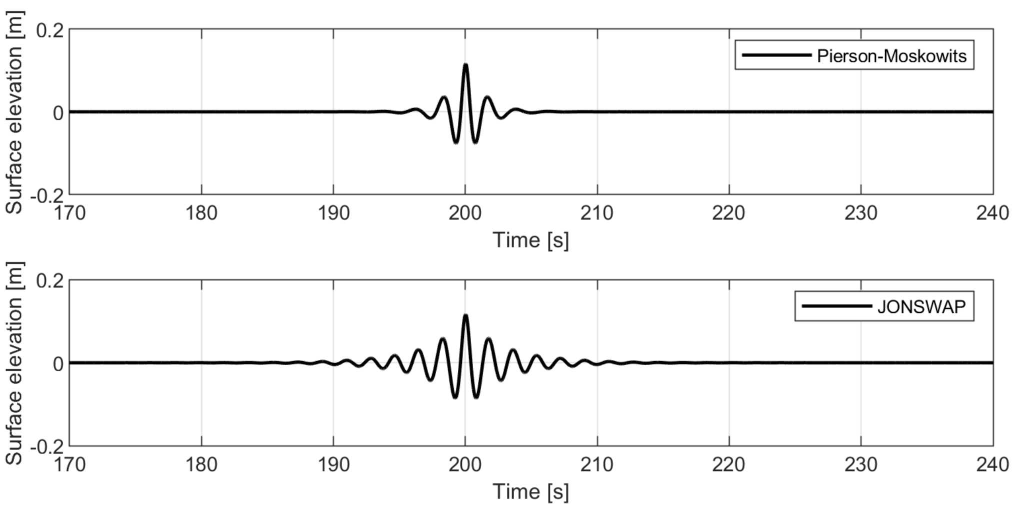

Figure 6.6: Comparison between two possible NewWave events depending on which enhancement factor (γ) is used and where the Pierson Moskowits NewWave profile shows an improved capacity of focusing compared to the JONSWAP NewWave profile.

This can be clarified by the groupiness of the wave energy around the peak period T_p which is stronger in case of a JONSWAP spectrum, focusing the energy around a limited amount of discrete frequencies available to reconstruct the NewWave group, as explained in Section 6.3 above. Combining a limited amount of wave components, which do not vary much in wave celerity (energy focused around peak), results in a reduced capacity of focusing. Therefore the JONSWAP NewWave profile is characterised by a larger wave group compared to the Pierson-Moskowits NewWave profile. The cut-off frequency limits are chosen as 0.2 Hz (lower cut-off) and 2 Hz (upper cut-off) for all cases, as the wave energy lies within these limits and the peak periods can be extracted from the measured incoming wave spectra. Important to note is that measurements have been carried out for approximately 1000 waves (ranging from 1094 to 1223 over nine cases). Therefore, the highest wave has a probability of exceedance of 1/1000 = 0.1%. In this research a comparable NewWave profile is modelled ($\eta_{goal} = \eta_{0.1\%}$), making the obtained measured $V_{max,measured}$ comparable with the NewWave profile induced overtopping volumes ($V_{NewWave}$). The presented methodology is based on the assumption that no surface elevation time series are available; therefore, $\eta_{0.1\%}$ needs to be estimated based on spectral properties. This is done so that the developed method can be reproduced in lack of surface elevation time series. The $\eta_{0.1\%}$ is obtained from a Composite Weibull distribution fit based on spectral properties as suggested by Battjes and Groenendijk (1999) and is therefore coupled to the wave spectrum. A Composite Weibull distribution is chosen since the limited water depth (intermediate water depth), which could induce wave-breaking for wave heights above the threshold value (see Figure 6.7). In these cases the Rayleigh distribution is not valid anymore.

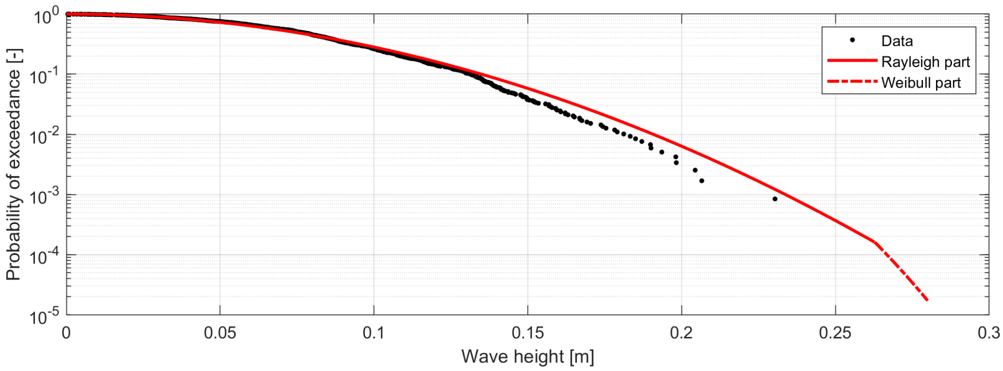

Figure 6.7: Composite Weibull exceedance curve for incoming wave heights considering case T205, showing a Rayleigh distribution (red line) until the threshold wave height and from there a Weibull distribution (red dotted line).

Data points are given as comparison, ensuring that values comparable to the measurements are extracted from the fitted distribution. As a result, the comparison between CoastalFOAM-NewWave and measurements can be done. The proposed procedure to extract the $H_{0.1\%}$ based on spectral properties was developed by Battjes and Groenendijk (1999) and is briefly explained below. Three input variables are of importance:

- water depth: h
- slope angle: α
- spectral wave height: H_{m0}

Two out of these three variables (h and H_{m0}) can be extracted from an offshore nearshore transformation using SWAN or other numerical models. In this research the spectral wave height (H_{m0}) is derived from the reconstructed measured incoming spectrum after application of the reflection analysis method. The slope angle can be retrieved from bathymetry profiles, yet for the studied cases the bottom is flat and therefore α is taken as a very large value (close to flat). The wave height which determines the transition between the Rayleigh part ($H < H_{tr}$) and the Weibull part ($H > H_{tr}$) of the Composite Weibull distribution is called the transitional wave height and is determined by Equation 6.7. In case of a flat slope the second term can be discarded, as $\tan\alpha$ becomes zero. Furthermore, the root means squared wave height is determined using Equations 6.8 and 6.9.

$$H_{tr} = (0.35 + 5.8 \cdot \tan\alpha) \cdot h \tag{6.7}$$

$$H_{rms} = (2.69 + 3.24 \cdot \Psi)\sqrt{m_0} \tag{6.8}$$

$$\Psi = \frac{\sqrt{m_0}}{h} \tag{6.9}$$

Now, the ratio between H_{tr} and H_{rms} determines the non-dimensional transitional wave height ($\tilde{h}_{tr}$), needed to determine $\tilde{H}_1$ and $\tilde{H}_2$, using Table 7.1 in Appendix C as explained by Battjes and Groenendijk (1999). The aforementioned non-dimensional values are in turn used to obtain H_1 and H_2, using Equations 6.10 and 6.11, needed to complete the non-exceedance Composite Weibull distribution given by Equation 6.12, where k_1 and k_2 equal 2 (Rayleigh) and 3.6 (Weibull) respectively.

$$H_1 = \tilde{H}_1 \cdot H_{rms} \tag{6.10}$$

$$H_2 = \tilde{H}_2 \cdot H_{rms} \tag{6.11}$$

$$F(H) \equiv Pr(\underline{H} \leq H) \begin{cases} F_1(H) = 1 - \exp\left[-\left(\frac{H}{H_1}\right)^{k_1}\right] & H \leq H_{tr} \\ F_2(H) = 1 - \exp\left[-\left(\frac{H}{H_2}\right)^{k_2}\right] & H > H_{tr} \end{cases} \tag{6.12}$$

From Figure 6.7 above it can be deduced that the Composite Weibull wave height exceedance distribution over-estimates the incoming measured wave heights, which increases for increasing non-linearity (increasing Ursell number) of the considered wave conditions. This over-estimation may be caused by the applied reflection analysis method (Zelt and Skjelbreia (1992)), which uses linear wave theory. This increased over-estimation for increasing non-linearity is shown in Section C.2 of Appendix C, where for all cases the Composite Weibull distribution is plotted against the incoming measured wave heights. Nevertheless, the wave heights extracted from the Composite Weibull distribution are higher compared to the measured incoming wave heights and can be accepted, since they give a safer design compared to the situation where the wave height would be under-estimated. Table 6.1 gives the resulting $\eta_{0.1\%}$ using Battjes and Groenendijk (1999) technique. Additionally, the maximum measured crest elevations ($\eta_{measured}$), obtained after adopting the reflection analysis method with a zero-down crossing method, are reported. This is done to show if the extracted $\eta_{0.1\%}$ values lie within acceptable range when compared to the measured values, which is the case. The Ursell number for the NewWave profile is calculated using the 5 highest waves within each NewWave profile (obtained with a zero-down crossing method).

Case	H$_{m0}[m]$	T$_p[s]$	h [m]	$H_{0.1\%}$ [m]	$\eta_{0.1\%}$ [m]	$\eta_{measured}$ [m]	η_{set-up} [m]	L [m]	Ursell [-]
T201	0.106	2.16	0.75	0.195	0.098	0.111	0.007	5.22	6.30
T202	0.124	2.36	0.75	0.230	0.115	0.120	0.013	5.82	8.84
T203	0.138	2.53	0.75	0.257	0.129	0.141	0.018	6.32	11.70
T204	0.104	1.66	0.75	0.192	0.096	0.100	0.002	3.68	3.47
T205	0.126	1.81	0.75	0.233	0.117	0.116	0.007	4.16	5.18
T206	0.148	1.97	0.75	0.271	0.136	0.139	0.013	4.65	7.79
T207	0.101	1.32	0.75	0.186	0.093	0.094	0	2.58	1.52
T208	0.123	1.46	0.75	0.229	0.115	0.113	0.002	3.04	2.41
T209	0.144	1.56	0.75	0.266	0.133	0.138	0.003	3.40	3.70

Table 6.1: Spectral properties of the incoming measured/physical wave conditions for all considered cases. Based on the spectral wave height H_{mo}, the $H_{0.1\%}$ is found according to Battjes and Groenendijk (1999) used to construct the Composite Weibull distribution from which $\eta_{0.1\%}$ is derived and compared to the maximum $\eta_{measured}$ experienced during measurements. Additionally, for each case a degree of non-linearity has been given in terms of the Ursell number.

6.6.2. Comparison between the theoretical and the OceanWaves3D NewWave profile

A MATLAB script "focusedwaves2.m" (applying the NewWave and linear wave theory with a first order wave generation) is used to produce the NewWave profile based on spectral properties. A first-order wave generation is used to compute the required horizontal paddle velocity time series. Using the $\eta_{0.1\%}$, T_p, γ and x_p as input variables does not immediately result in the desired NewWave profile at the focus location on first try. Therefore, an iterative approach is opted where the $\eta_{0.1\%}$ and the focus location x_p are changed until comparable results are achieved. An example of a NewWave profile obtained with the iterative approach is given in Figure 6.8, which shows that the modelled NewWave profile is different from the NewWave profile according to the NewWave theory. This difference could affect wave overtopping results and is discussed below.

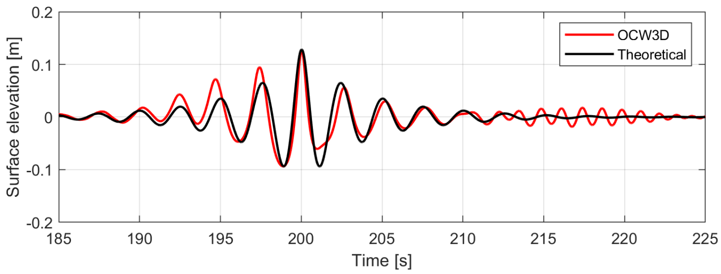

(a) Focused wave group, wave climate T203.

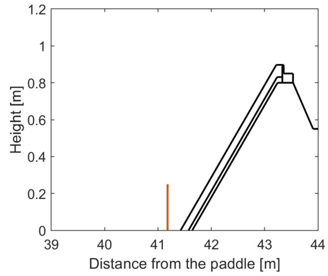

(b) Location of focusing.

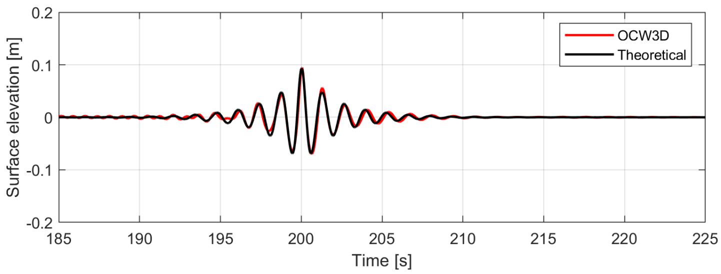

(c) Focused wave group, wave climate T207.

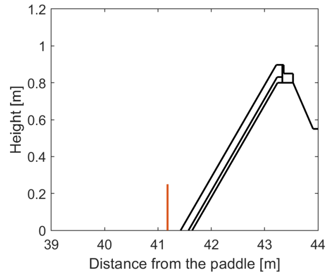

(d) Location of focusing.

Figure 6.8: Comparing the most non-linear NewWave focused wave group (a, b) with the least non-linear NewWave focused wave group (c, d), where the spurious waves gain in magnitude for increasing non-linear character.

Using a first-order wave generation to produce a NewWave profile in intermediate water depths (weakly non-linear waves) introduces errors, referred to as ”spurious waves” or ”error waves”. It is caused by using the linear wave generation outside its validity range. The error waves consist of low frequency waves travelling ahead of the NewWave profile and of high frequency waves trailing behind, as can be seen in Figure 6.8a. A set-up is experienced ahead of the NewWave profile. The set-up η_{set-up} in front of the NewWave profile is quantified by subtracting the original (black) and the filtered signal (red dotted). This set-up (approximately 0.018 m for an input $\eta_{0.1\%}$ = 0.129 m; the highest among all cases) is visible in Figure 6.9a below, where the long error wave is filtered out using a frequency cut-off filter for case T203 (most non-linear, highest Ursell number). The other remaining cases are reported in Sections C.3 and C.4 of Appendix C. The waves trailing behind will not influence the wave run-up and the overtopping results as they interact with the structure after the NewWave profile has passed. Therefore, from now on these waves are not considered anymore.

In contrast, the long error wave does influence run-up levels and overtopping quantities as reported by Orszaghova et al. (2014) and Whittaker et al. (2017). The spurious wave enhances the wave heights in front of the leading crest of the NewWave profile and flattens the troughs which induces later wave breaking. Orszaghova et al. (2014) reported that the spurious wave reduced overtopping volumes between 25-83%. However, they were studying a sloping foreshore where waves do have the time to break before arriving at the structure. In this research, instead, the bed is horizontal and the distance over which the waves tend to break small (armour slope). Therefore, the aforementioned effect on the overtopping quantities is expected to be less significant. The long error wave could be removed with a second order wave generation technique, as proposed by Schaffer (1995), but this is left for future research.

It can be concluded from the reported figures in Section C.4 of Appendix C and the reported η_{set-up} in Table 6.1 that the magnitude of the produced spurious waves is correlated with the degree of non-linearity of the produced NewWave profile. The higher the degree of non-linearity, given by the Ursell number, the more pronounced the spurious wave. The Ursell number is obtained by considering the wave height and period (wave length) of the 5 highest waves within the travelling NewWave profile. If the nine considered cases (T201-209) are ranked in function of the degree of non-linearity, and compared between themselves, some conclusions can be derived. Looking at Table 6.1 above, case T203 shows the highest degree of non-linearity (Ursell number). In contrast, Figure 6.9b (case T207) shows the least.

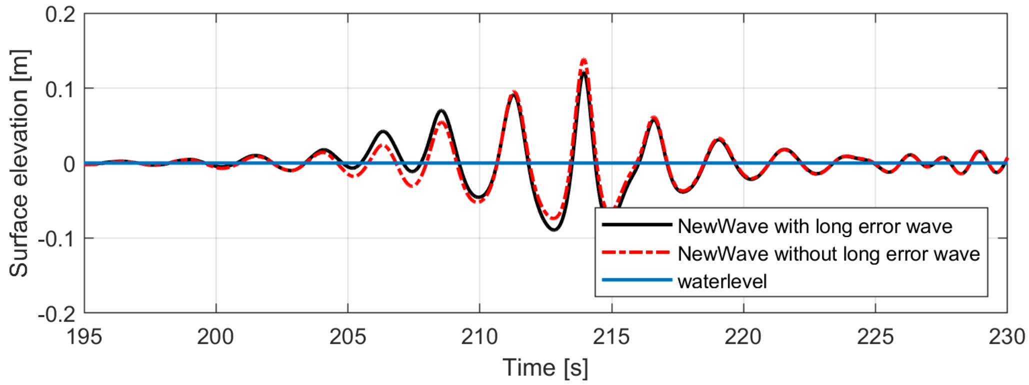

(a) Case T203.

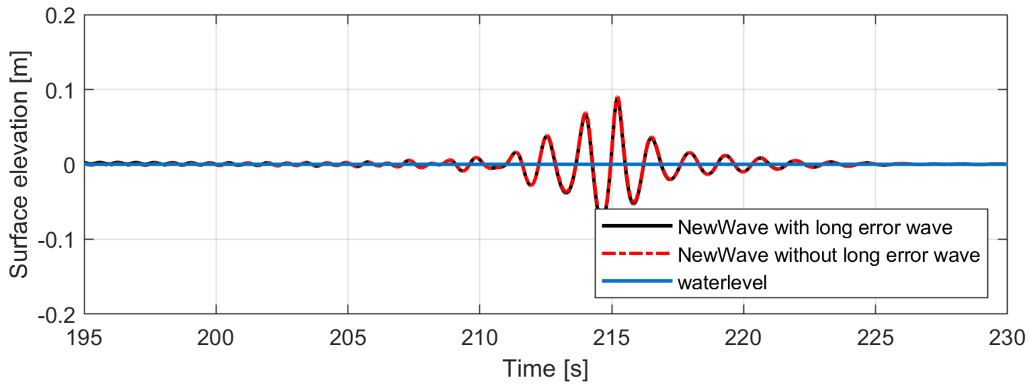

(b) Case T207.

Figure 6.9: A comparison for case T203 (a) and T207 (b) between the NewWave profile containing the low frequency error wave (black line) and the NewWave profile where the low frequency wave is filtered out (red dotted line).

If both cases (T203 and T207) are plotted (see Figure 6.9), it can be concluded that for increasing non-linearity (increasing Ursell number) the magnitude of the spurious waves increases and is most pronounced for case T203. The comparison between the theoretical NewWave profiles and what is generated in OceanWaves3D for the other cases is reported in Section C.3 of Appendix C.

6.6.3. NewWave in CoastalFOAM

The produced NewWave profiles (capturing $\eta_{0.1\%}$ well at the desired focus location, x_p) are now modelled in CoastalFOAM to procure the maximum overtopping volumes $V_{NewWave}$. The NewWave profiles are modelled in CoastalFOAM with the same numerical settings used for the validation of the average overtopping discharge. Figure 6.10 below shows the incoming wave climate (red) generated with OceanWaves3D and the total surface elevation (black) measured at focusing point close to the toe of the breakwater. The difference between the OceanWaves3D and the CoastalFOAM signal is caused by the presence of the structure in the CoastalFOAM domain, inducing reflection. The reflection coefficients for all 9 cases have been computed and lie within a 6% confidence interval when compared to measured reported reflection coefficients from the full time series. Reflection is therefore well represented using the corrected porous flow coefficients (see Chapter 5).

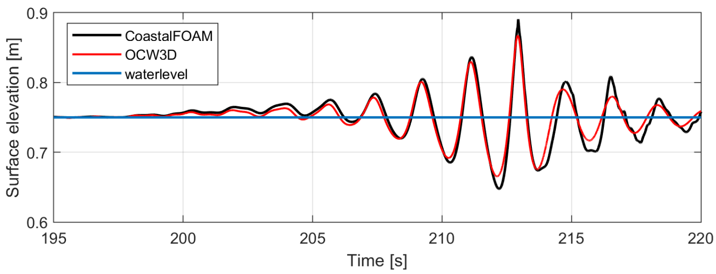

(a) Surface elevation time series.

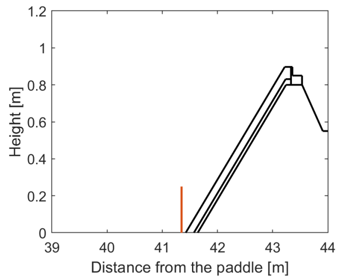

(b) Location of interest.

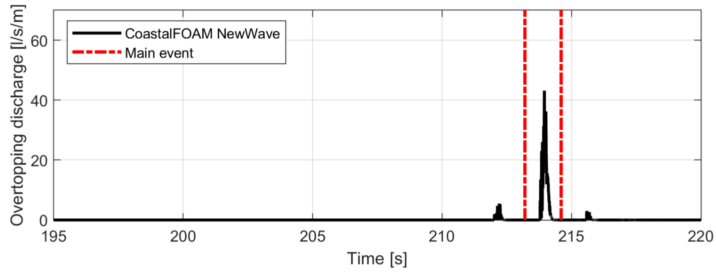

(c) Overtopping discharge time series.

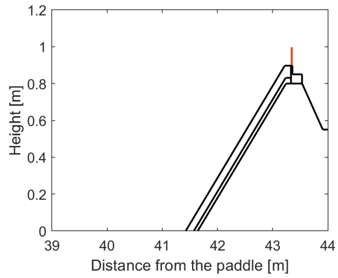

(d) Measuring location.

Figure 6.10: (a) Comparison between CoastalFOAM and OceanWaves3D surface elevation time series for a non-protruding wave wall case, where the difference is induced by the reflection of the rubble mound breakwater. (b) The location at which the comparison is made. (c) The instantaneous overtopping discharge caused by the NewWave. (d) The location at which the overtopping discharge is captured.

The distance between the wave gauge at which the focusing occurs and the measuring overtopping surface (model) is roughly 2.2 m. The time at which the $\eta_{0.1\%}$ passes is measured at 212.9 s and the time at which the peak overtopping discharge is captured occurs around 214.0 s, with a time difference equal to 1.1 s. If the wave celerity is approximated using linear wave theory for the shown case (A3W1T205), equal to 2.30 m/s, the distance covered by the wave can be estimated by multiplying the wave celerity with the time difference, $L_{covered} = t_{diff} \cdot c$, which results in 2.53 m. This estimation gives a rough first impression that the highest wave indeed causes the highest overtopping event, referred to as the Main event. Integrating the overtopping discharge over time results in the overtopped volume (l/m). For each case the overtopped volume has been computed and is compared with the maximum measured overtopping volumes (see Section 6.6.5).

Now the theoretical NewWave profile $\eta_{0.1\%,theory}$ (Section 6.6.1 above) is compared with the OceanWaves3D NewWave profile $\eta_{0.1\%,OCW3D}$ (Section 6.6.2 above) and the CoastalFOAM NewWave profile after completing the reflection analysis method ($\eta_{0.1\%,OF,in}$). The comparison is shown in Figure 6.11. For all the nine runs the focus location lies between 41.15 and 41.40 m (see Figure 6.11b). Three groups can be distinguished from Figure 6.11: an upper, a middle and a lower cloud of dots:

- Upper cloud shows the T203, T206 and T209 wave conditions
- Middle cloud shows the T202, T205 and T208 wave conditions
- Lower cloud shows the T201, T204 and T207 wave conditions

The upper part shows the largest difference between the NewWave profile in OceanWaves3D and the incoming NewWave profile in CoastalFOAM. The reflection analysis method uses linear wave theory to split the total surface elevation in incoming and reflected surface elevations and induces errors for non-linear cases. From Figure 6.11 it can be inferred that for increasing H_{m0} (see Table 6.1 above) the adopted reflection analysis method overestimates crest elevations compared to the produced OceanWaves3D crest elevations (cases T201, 202, 203, 205 and 206). Additionally, considering the overall NewWave profile, it can be deduced that the quality of reproduction of the theoretical NewWave profile decreases with increasing non-linearity, as can be seen in Figure 6.8 above.

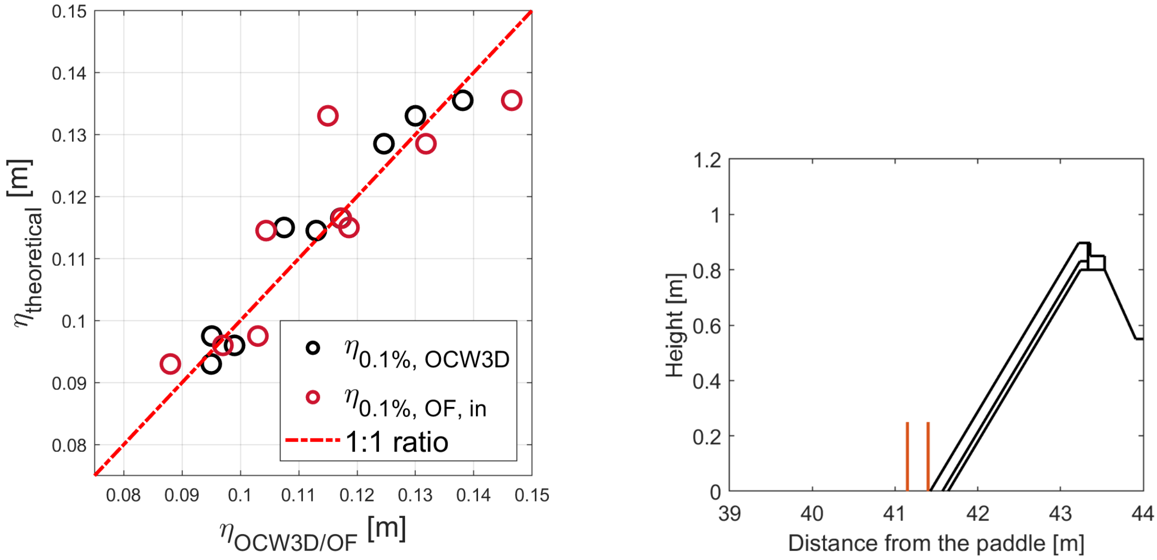

(a) Comparison $\eta_{0.1\%}$.

(b) Location lies between 41.15 and 41.40 m.

Figure 6.11: (a) Comparison between $\eta_{0.1\%,theory}$, $\eta_{max,OCW3D}$ and $\eta_{0.1\%,OF,in}$ for the nine non-protruding cases at focus location. (b) Range in which focusing of the incoming NewWave occurs.

6.6.4. Location of focusing

The focus location has a direct impact on the quantity of overtopped water (Whittaker et al., 2018). Away from the focus location the energy/maximum crest level of the NewWave profile will decrease. Therefore, to reproduce the most violent event (largest wave), focusing is forced at the toe of the breakwater, which is considered between 41.15 and 41.40 m. A region of desired focusing is defined as focusing is achieved by multiple iterations, making it difficult to attain the exact desired location. The sensitivity of this parameter (x_p) is studied for a rubble mound breakwater by running multiple CoastalFOAM simulations where the NewWave profile is focused at different locations (see Figure 6.12 and Table 6.2 below).

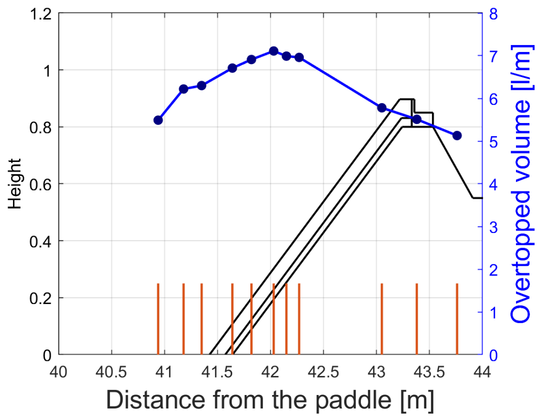

Focus location	x_p [m]	$V_{max,NewWave}$ [l/m]
Location 1	40.94	5.49
Location 2	41.18	6.22
Location 3	41.35	6.30
Location 4	41.64	6.71
Location 5	41.82	6.91
Location 6	42.03	7.11
Location 7	42.15	6.99
Location 8	42.27	6.96
Location 9	43.05	5.78
Location 10	43.38	5.51
Location 11	43.76	5.13

Figure 6.12 and Table 6.2: Figure on the left showing the various locations at which focusing is forced, for a non-protruding wave wall case (A3W1T205), and how the overtopping volume varies along these locations. Table 6.2 showing the exact results.

A non-protruding wave wall case (A3W1T205) is chosen to study the influence of the focus location on the overtopping volume. From the multiple simulations, it can be deduced that the obtained overtopped volume is highest when focusing occurs around the toe of the breakwater. The difference in overtopped volume between focus location 2 and 3 is negligible and therefore the earlier mentioned focusing range can be accepted (41.15-41.40 m). Location 6 shows the highest overtopped volume. The waves tend to break further on the slope as the influence of the breakwater is still small at that location. Consequently, higher overtopped volumes are captured. This finding can be case dependent (wave height and period, type of breakwater and foreshore), therefore focusing is kept between the previously mentioned boundaries (location 2-3). Location 7 and onwards show that the quality of focusing is reduced (waves are breaking at this location), which leads to lower overtopping volumes.

6.6.5. Comparison with measurements

Now the NewWave modelled overtopping volumes are compared with the maximum measured overtopping volumes, for non-protruding and protruding wave wall cases (see Figure 7.4 below).

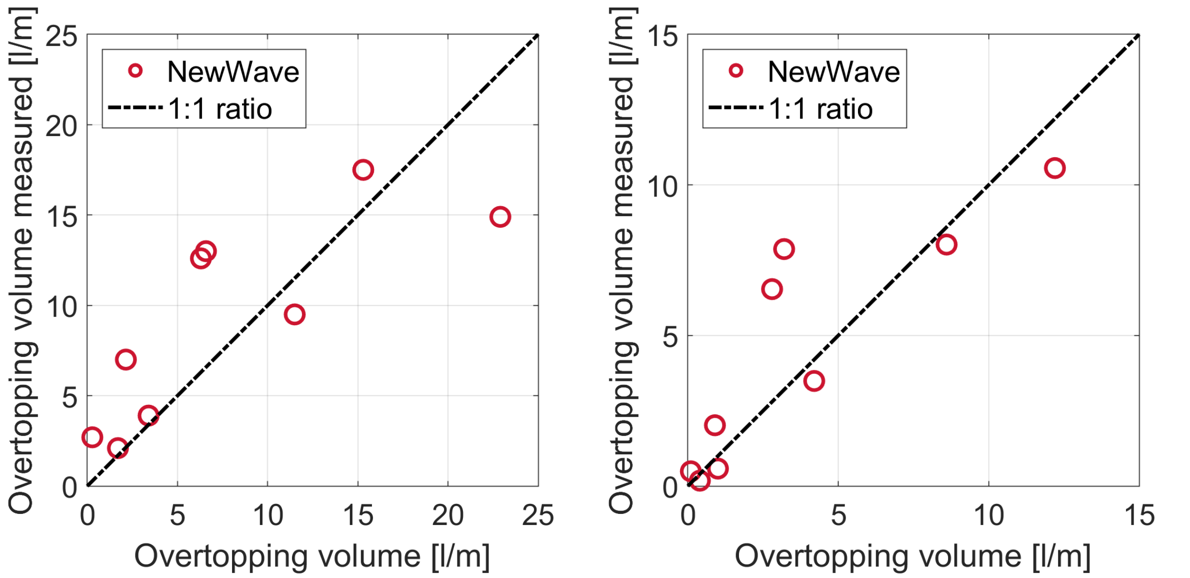

(a) Non-protruding wave wall cases.

(b) Protruding wave wall cases.

Figure 6.13: Maximum overtopping volumes, including a comparison between the NewWave approach and measurements. (a) For non-protruding wave wall cases. (b) For protruding wave wall cases.

It is noteworthy to mention that the adopted method to quantify the maximum volumes from the measured cumulative overtopping curves (see Section 6.2 above) is sensitive for errors, and this is accounted for in the discussion (see Chapter 8). Figures 6.14 and 6.15 herebelow give the overtopping volumes as function of the degree of non-linearity of the considered wave conditions. The intersect of both trend lines is forced through zero, as no waves (Ursell equals zero) results in no overtopping. In doing so, the NewWave trend line matches the measured trend line, showing that the proposed methodology matches the general trend of measured maximum overtopping volumes, for non-protruding and protruding wave wall cases. Furthermore, from Figures 6.14 and 6.15 it can be deduced that for increasing degree of non-linearity (increased Ursell number) of the considered wave climate the $V_{NewWave}$ over-estimates the $V_{Measured}$. On the contrary, the most linear cases (lowest Ursell number) have the tendency to under-estimate the $V_{Measured}$. Two possible causes can be identified:

- 1. For increasing degree of non-linearity the Composite Weibull distribution over-estimate the incoming measured wave heights. Therefore, the extracted $H_{0.1\%}$ values are higher compared to the measured data and a higher $\eta_{0.1\%}$ induces a higher maximum overtopping volume.

- 2. NewWave groups characterised by a strong non-linear character (highest Ursell number) enhance the magnitude of spurious waves (see Section 6.6.2 above). Most importantly, the long error wave travelling in front is inducing an increased water level prior to the NewWave profile. This fills the pores of the armour and filter layer, reducing the experienced roughness for the incoming waves. As a consequence, the overtopping volumes increase, which can also be seen in Table 6.3 where the modelled NewWave volumes ($V_{NewWave}$) are compared with the measurements ($V_{Measured}$).

Geometry	Protruding		Non-Protruding			
Case	$V_{NewWave}$ [l/m]	$V_{Measured}$ [l/m]	Case	$V_{NewWave}$ [l/m]	$V_{Measured}$ [l/m]	Ursell
A1T201	1.0	0.58	A3T201	3.4	3.92	6.3
A1T202	4.2	3.49	A3T202	11.5	9.56	8.8
A1T203	12.2	10.56	A3T203	22.9	14.92	11.7
A1T204	0.4	0.18	A3T204	1.7	2.10	3.5
A1T205	2.7	6.54	A3T205	6.2	12.56	5.2
A1T206	8.6	8.02	A3T206	15.3	17.53	7.8
A1T207	0.1	0.49	A3T207	0.3	2.74	1.5
A1T208	0.9	2.02	A3T208	2.1	7.03	2.4
A1T209	3.2	7.87	A3T209	6.6	13.01	3.7

Table 6.3: Maximum overtopping volumes, including a comparison between the NewWave methodology and measured maximum overtopping volumes for protruding and non-protruding wave wall cases. The Ursell number describes the degree of non-linearity for each case.

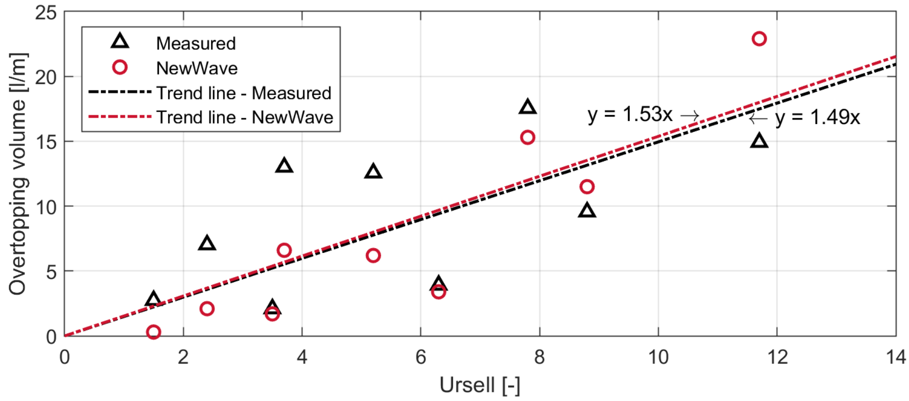

Figure 6.14: The maximum overtopping volume plotted against the Ursell number, including a comparison between: the NewWave methodology and the measurements for non-protruding wave wall cases.

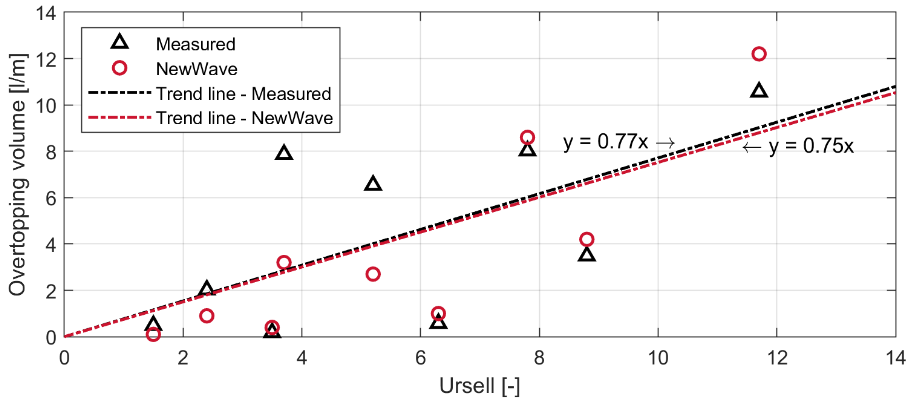

Figure 6.15: The maximum overtopping volume plotted against the Ursell number, including a comparison between: the NewWave methodology and the measurements for protruding wave wall cases.

6.7. Methodology to assess the average overtopping discharge, q

In this section the NewWave theory is applied to quantify the average overtopping discharge, given the incoming wave conditions. The present research proposes a technique referred to as the single event approach. This technique is explained below.

6.7.1. The single event approach

The maximum overtopped volumes were quantified by one single NewWave event in Section 6.6 above. Now, the NewWave overtopping volumes are used in the inverse EurOtop 2018 approach to compute the NewWave average overtopping discharges. The EurOtop 2018 manual touches upon a relation between the average overtopping discharge (q) and the maximum overtopped volume (V_{max}), given by Equations 6.13 to 6.17.

$$V_{max} = a \cdot [\ln N_{ow}]^{1/b} \tag{6.13}$$

$$a = \left(\frac{1}{\Gamma(1+\frac{1}{b})}\right)(\frac{qT_m}{P_{ov}}) \tag{6.14}$$

$$b = 0.85 + 1500\left(\frac{q}{gH_{m0}T_{m-1,0}}\right)^{1.3} \tag{6.15}$$

$$P_{ov} = N_{ow}/N_w = exp\left[-\left(\sqrt{-\ln 0.001}\frac{R_c}{R_{u,2\%}}\right)^2\right] \tag{6.16}$$

$$R_{u,2\%} = 1.75 \cdot H_{m0} \cdot \gamma_\beta \cdot \gamma_b \cdot \gamma_f \cdot \xi_{m-1,0} \tag{6.17}$$

Where a and b are fitting parameters which depend on: the average overtopping discharge q; probability of overtopping P_{ov}, which translates to the ratio between the number of waves that lead to an overtopping event (N_{ow}) and the total number of waves (N_w) within the considered incoming wave conditions; the spectral periods T_m and $T_{m-1,0}$. The probability of overtopping depends on the run up level exceeded by 2% of the waves $R_{u,2\%}$. To be coherent with the rest of the present research, the updated roughness coefficient (Molines and Medina (2015), γ_f = 0.53) is used in Equation 6.17, even if the original roughness performed better (see Table 6.4 below). Additionally, the original 0.02 value (related to the 2% run-up level; see Formula 6.16) is altered here to 0.001 as the V_{max} is the volume caused by the $H_{0.1\%}$ exceedance wave height.

6.7.2. Comparison with measurements

To compare the results of the proposed method with measurements, similar figures are used as applied in the EurOtop 2018 manual. The relative overtopping rate ($q/(gH_{m0}^3)^{0.5}$) is plotted against the relative freeboard (R_c/H_{m0}) in Figures 6.16 and 6.17. The obtained NewWave overtopping discharges are compared with measurements by means of the root mean squared errors in Table 6.4. These discharges can be evaluated against the reported measured average discharges for the respective cases.

	Non-protruding	Protruding
Method	RMSE [l/s/m]	
Measured average	0.122	0.029
NewWave/Reverse EurOtop 2018 (γ_f = 0.40)	0.137	0.047
NewWave/Reverse EurOtop 2018 (γ_f = 0.53)	0.234	0.099

Table 6.4: RMSE values when comparing both NewWave approaches (original and updated roughness) with measurements, for non-protruding and protruding wave wall cases. In addition, the measured average discharges of the respective cases are given against which the RMSE values can be evaluated.

For increasing degree of non-linearity (Ursell number) the NewWave overtopping discharges tend to over-estimate measurements. This tendance to over-estimate was also the case for the maximum overtopping volumes (see Section 6.6.5 above) and is carried further here by using the original inverse EurOtop 2018 approach. Moreover, Figures 6.16 and 6.17 reveal a wide scatter compared to measurements which is undesired when considered as design tool.

Non-protruding wave wall

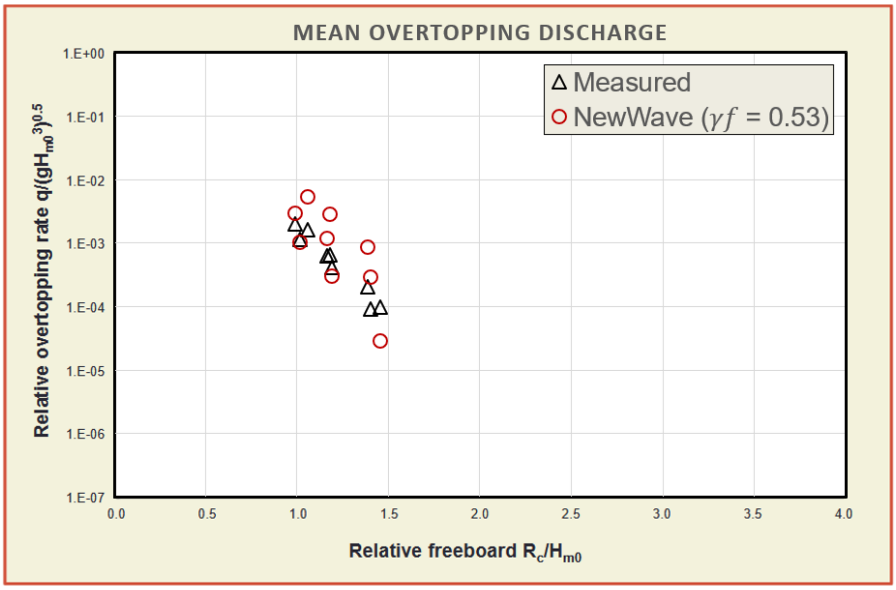

Figure 6.16: Mean overtopping discharge for non-protruding wave wall cases in terms of relative overtopping rate and relative freeboard, including a comparison between: physical laboratory measurements and the NewWave single event approach using the updated roughness (γ_f = 0.53).

Protruding wave wall

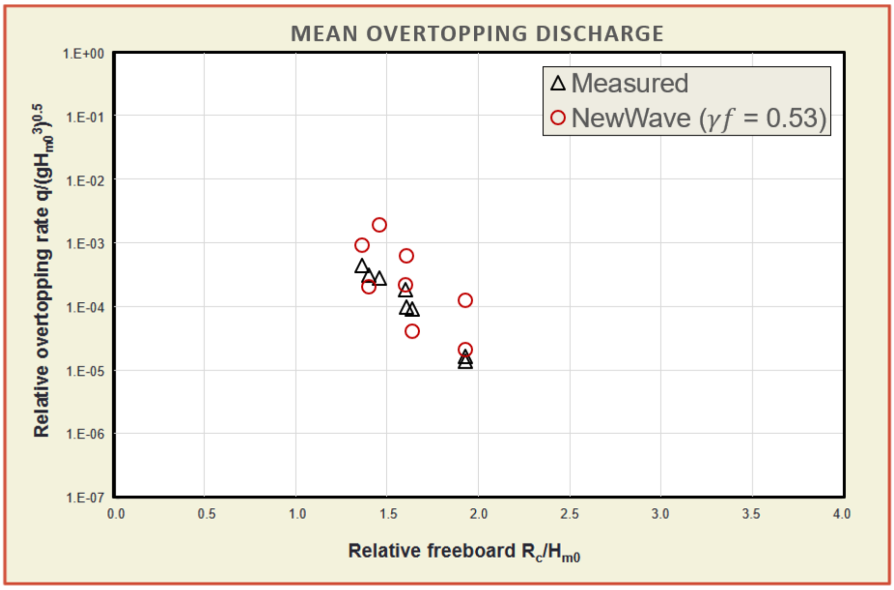

Figure 6.17: Mean overtopping discharge for protruding wave wall cases in terms of relative overtopping rate and relative freeboard, including a comparison between: physical laboratory measurements and the NewWave single event approach using the updated roughness (γ_f = 0.53).

7

Comparison with empirical methods

7.1. Introduction

Chapter 3 showed that the empirical average overtopping discharges under-estimated the physical experiments described in Chapter 2. Based on the identified research gap in Chapter 1 the choice was made to validate the wave overtopping over rubble mound breakwaters with CoastalFOAM. The aim of the present chapter is to show if the numerical model developed, calibrated and validated so far can be applied in the design process of rubble mound breakwaters and if the numerical model outcomes (see Chapters 5 and 6) perform better compared to the updated empirical method (EurOtop 2018, γ = 0.53). The original EurOtop 2018 approach (γ = 0.40) showed significant shortcomings and is therefore disregarded. In this chapter the numerical results are compared with the selected empirical method (see Chapter 3) and measurements, in two stages: a comparison with CoastalFOAM in terms of average overtopping discharges (q; accounting for 500 waves) and a comparison with the proposed NewWave methodologies in terms of maximum overtopping volumes (V_{max}) and average overtopping discharges (q; accounting for one NewWave profile).

7.2. Comparison EurOtop 2018 with CoastalFOAM, q

To compare the results of the different methods, similar figures are used as applied in the EurOtop 2018 manual. The relative overtopping rate ($q/(gH_{m0}^3)^{0.5}$) is plotted against the relative freeboard (R_c/H_{m0}). For the spectral wave height (H_{m0}) the measured incoming spectral wave height is used for all cases (modelled, measured and empirical). In doing so all results are plotted on the same vertical line since the crest-freeboard is kept constant between methods. This was possible as Chapter 5 showed that the modelled incident spectral wave height after the calibration procedure was similar to the measured one, for all cases.

The case specific cumulative overtopping curves, comparing model outcomes with measurements, were given in Chapter 5. Adding the considered empirical methods to all cumulative curves is done and shown in Section D.1 of Appendix D.

Non-protruding wave wall cases

For the non-protruding wave wall cases CoastalFOAM shows the highest accuracy compared to measurements. Table 7.1 below gives the RMSE value for each applied method. In Chapter 5 most of the numerical discrepancies compared to the physical flume were solved by calibrating the numerical model. For two (medium and large overtopping) out of the three cases CoastalFOAM performed better compared to the updated EurOtop 2018 method. Considering all non-protruding wave wall cases the numerical model (RMSE = 0.007 l/s/m) performed better compared to the EurOtop 2018 methodology (updated (RMSE = 0.044 l/s/m)). The measured average discharge of the respective non-protruding cases is 0.108 l/s/m.

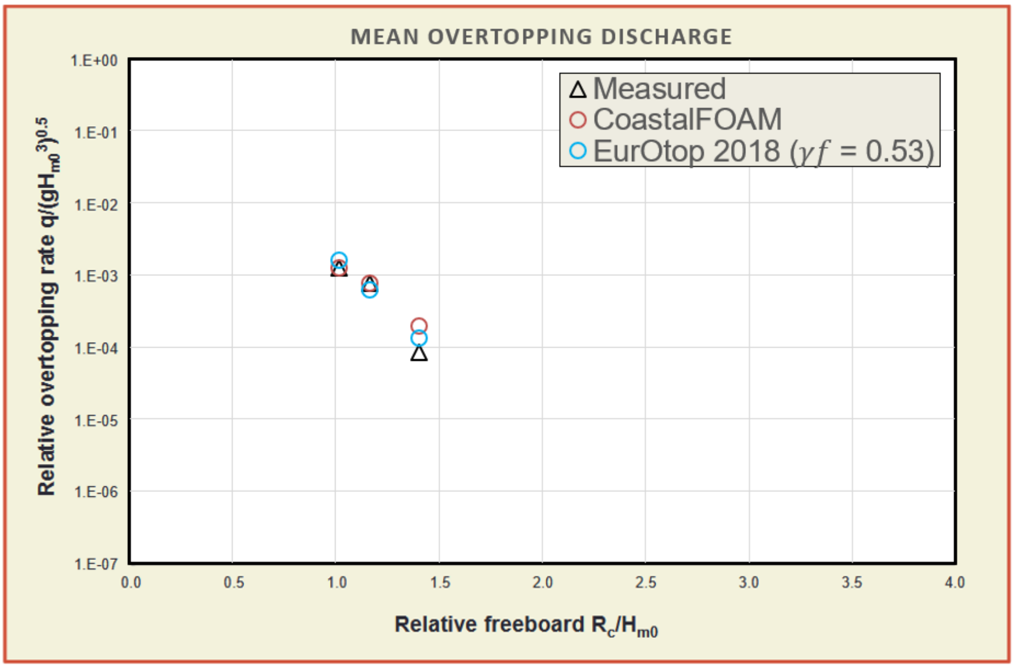

Figure 7.1: Mean overtopping discharge for non-protruding wave wall cases in terms of relative overtopping rate and relative freeboard, including a comparison between: physical laboratory measurements, the improved numerical model (CoastalFOAM) and the updated EurOtop 2018 guidelines.

Protruding wave wall cases

When considering the protruding wave wall cases (see Figure 7.2), it is evident that CoastalFOAM over-estimates and the updated EurOtop methodology under-estimates the measurements. For two (medium and large prototype overtopping) out of three cases CoastalFOAM shows good agreement with measurements. Table 7.1 below gives the RMSE value for each applied method.

	Non-protruding	Protruding
Method	RMSE [l/s/m]	
EurOtop 2018 (γ_f = 0.53)	0.044	0.020
CoastalFOAM - calibrated	0.007	0.030

Table 7.1: RMSE values of three proposed methods for the estimation of the average overtopping discharge q, including a separation between: protruding, non-protruding wave wall and overall.

From this table it can be inferred that the updated EurOtop 2018 (RMSE = 0.020 l/s/m) approach showed improved accuracy compared to CoastalFOAM (RMSE = 0.030 l/s/m). The measured average discharge of the respective protruding cases is 0.031 l/s/m. It is mainly the small overtopping discharge case (highest R_c/H_{m0} ratio) that is better estimated with the EurOtop 2018 corrected methodology when compared with model outcomes. Two causes may explain the over-estimated numerical model outcomes compared to measurements:

- The overtopping discrepancies, still present after the numerical model was calibrated, which become more frequent for protruding wave wall cases and relatively more important for decreasing average overtopping discharge (to the right in Figure 7.2). In Chapter 5 and Section 5.5.4 it was shown that numerical diffusion mainly caused this over-estimation.
- The degree of openness of the wave wall which has a significant influence on the average overtopping discharge as seen in Section 5.5.

Furthermore, from Figure 7.2 below it can be deduced that all results run on a (near) straight line, except for the measured small overtopping case. This test sample could therefore be interpreted as wrong and additional small overtopping cases should be modelled and compared.

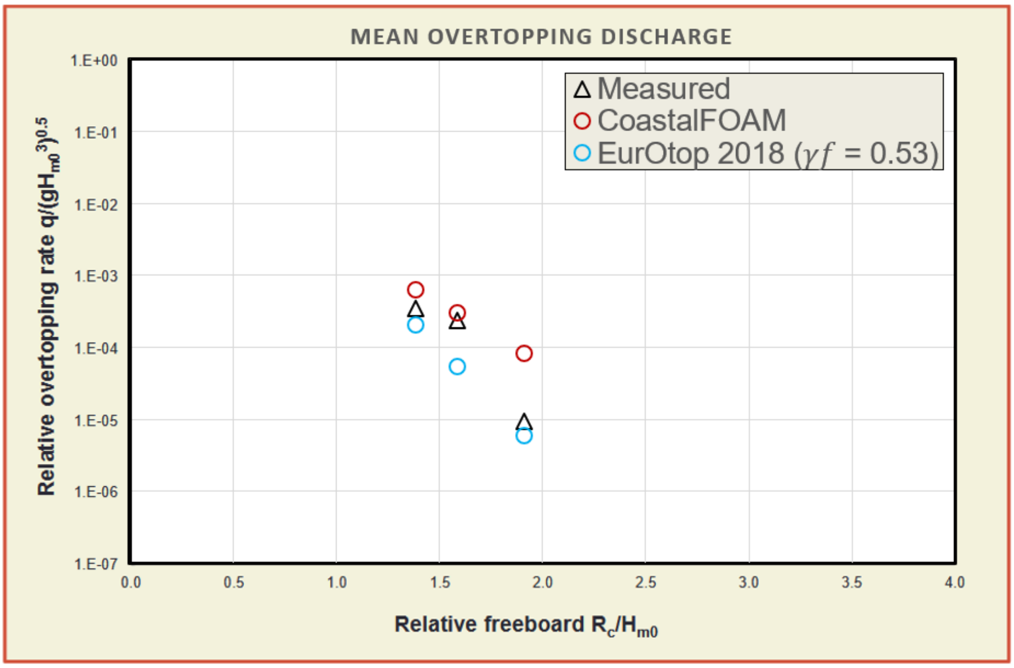

Figure 7.2: Mean overtopping discharge for protruding wave wall cases in terms of relative overtopping rate and relative freeboard, including a comparison between: physical laboratory measurements, the improved numerical model (CoastalFOAM) and the updated EurOtop 2018 guidelines.

7.2.1. Overall comparison

Figure 7.3 illustrates the four possible approaches designers can choose from when designing a rubble mound breakwater, considering the average discharge (q) as design criterion. The four different methods (EurOtop original or updated and CoastalFOAM uncalibrated or calibrated) were all addressed in this research (see Chapters 3 and 5). The designer can use Figure 7.3 to evaluate which design tool to apply, while considering aspects such as time/cost and accuracy. The achieved accuracies per method are expressed in terms of RMSE (l/s/m), where yellow stands for non-protruding wave wall and light blue for protruding wave wall cases. Additionally, the measured average discharges are given for the respective cases so that the magnitude of the computed RMSE can be quantified. To assess both EurOtop 2018 methodologies and the calibrated version of CoastalFOAM the 6 validation cases were considered. Similarly, in case of the uncalibrated version of CoastalFOAM 6 cases were selected. However, 2 cases were different compared to the selected cases in this research, hence the reported differences in measured average overtopping discharges ($q_{mes,average}$).

In lack of physical experiments, the original EurOtop 2018 and the uncalibrated CoastalFOAM model are available as design tools. Taking both into account, the uncalibrated CoastalFOAM model showed to be more promising for the non-protruding wave wall cases, considering the relation between the RMSE value and the according measured average discharge. This ratio (RMSE/$q_{mes,average}$, also known as the normalised RMSE) is lower in case of CoastalFOAM (non-protruding, CoastalFOAM ratio = 0.16 and EurOtop 2018 ratio = 0.99). On the contrary, in case of the protruding wave wall cases the original EurOtop performed better (protruding, uncalibrated CoastalFOAM ratio = 1.67 and EurOtop 2018 ratio = 1.23). However, for the original EurOtop 2018 method, the under-estimations are so large that the RMSE converges to the mean measured discharge, which can be misleading and result in an improved ratio (close to 1) compared to the uncalibrated model. As reported in Chapter 3, the under-estimations were ranging between between 14-273x, which are higher than the reported errors by Boersen et al. (2019) (over-estimating by a factor 2.5x) for the uncalibrated model. The latter is therefore advised, for both geometries, in lack of physical laboratory experiments.

When physical experiments are performed, the EurOtop 2018 approach can be updated and used along with a calibrated CoastalFOAM model. For non-protruding wave wall cases the calibrated CoastalFOAM model (ratio = RMSE/$q_{mes,average}$ = 0.008/0.108 = 0.07) showed higher accuracy when compared to the updated EurOtop 2018 technique (ratio = 0.41). However, the updated EurOtop 2018 (ratio = 0.65) demonstrated to be more capable than CoastalFOAM (ratio = 0.97) in assessing the average overtopping discharge for protruding wave wall cases. Possible causes were addressed in Section 7.2 above.

Additionally, CoastalFOAM is capable of modelling instantaneous overtopping discharges, velocities, pressures and forces simultaneously, which is an advantage when compared to empirical formulas. The use of CoastalFOAM should therefore be encouraged in the preliminary design stage of rubble mound breakwaters. However, the increased accuracy and advantages are at the cost of computational time.

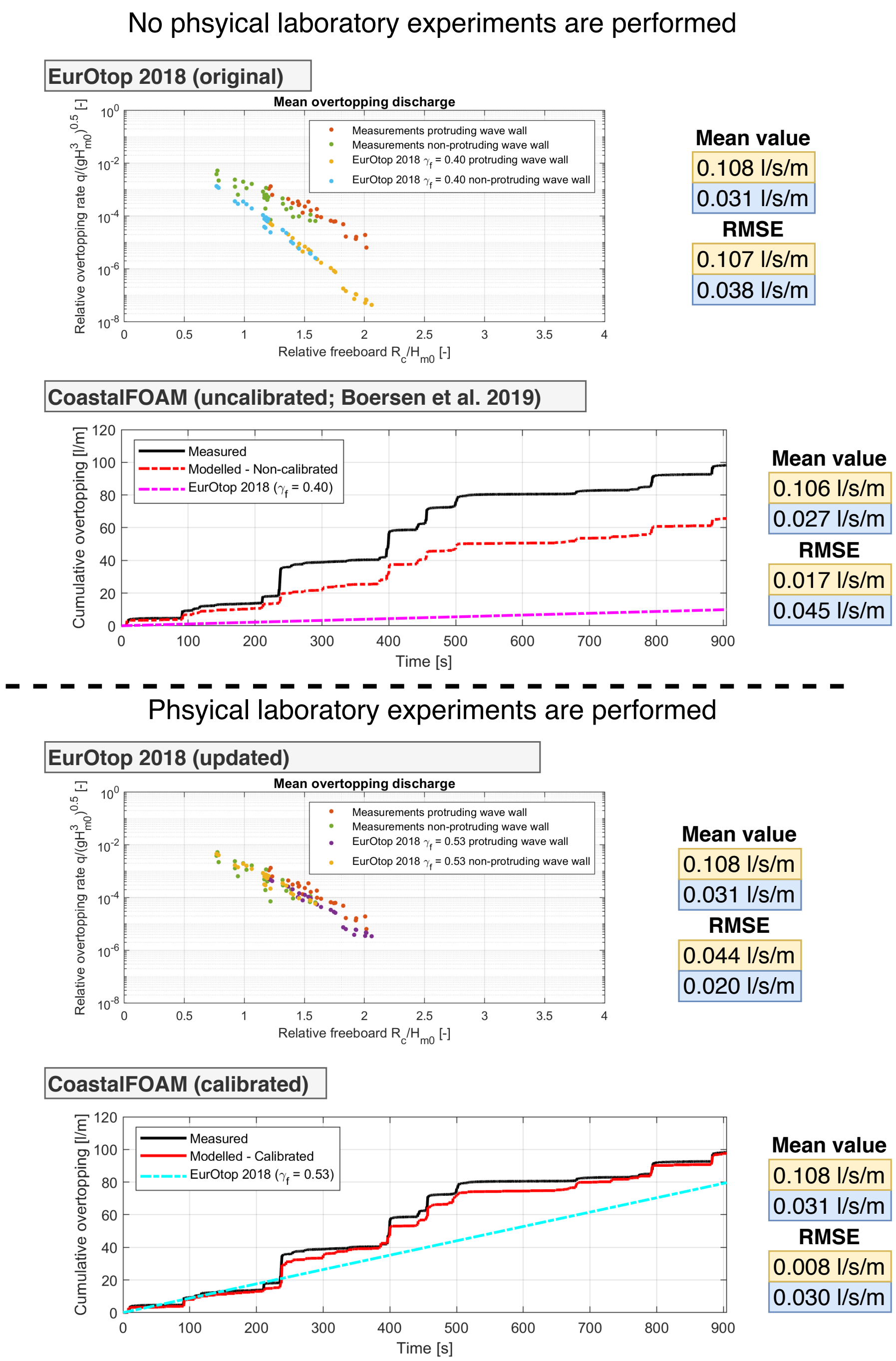

Figure 7.3: Schematization of methods considered in the present research to assess q, where a distinction is made based on the availability of physical experiments. The accuracy of each method is given in function of RMSE values and measured average overtopping discharges, light blue boxes are for protruding wave wall cases and yellow for non-protruding wave wall cases.

7.3. Comparison EurOtop 2018 with NewWave methodologies

7.3.1. Comparison of maximum overtopping volumes - NewWave approach

In this section the NewWave modelled overtopping volumes, using the approach explained in Chapter 6, are compared with: the maximum measured overtopping volumes and the EurOtop 2018 computed maximum overtopping volumes. The methodology proposed by the EurOtop 2018 was already explained in Section 6.7.1, where it was used inversely to compute the NewWave average discharge from the NewWave overtopping volume. Here the EurOtop 2018 maximum overtopping volumes are calculated using the average overtopping discharges computed in Chapter 3, adopting the updated roughness coefficient. Figure 7.4 compares: the earlier computed NewWave overtopping volumes (see Chapter 6), the EurOtop 2018 overtopping volumes (using the updated roughness coefficient) and the measured maximum overtopping volumes retrieved from the measured cumulative overtopping curves.

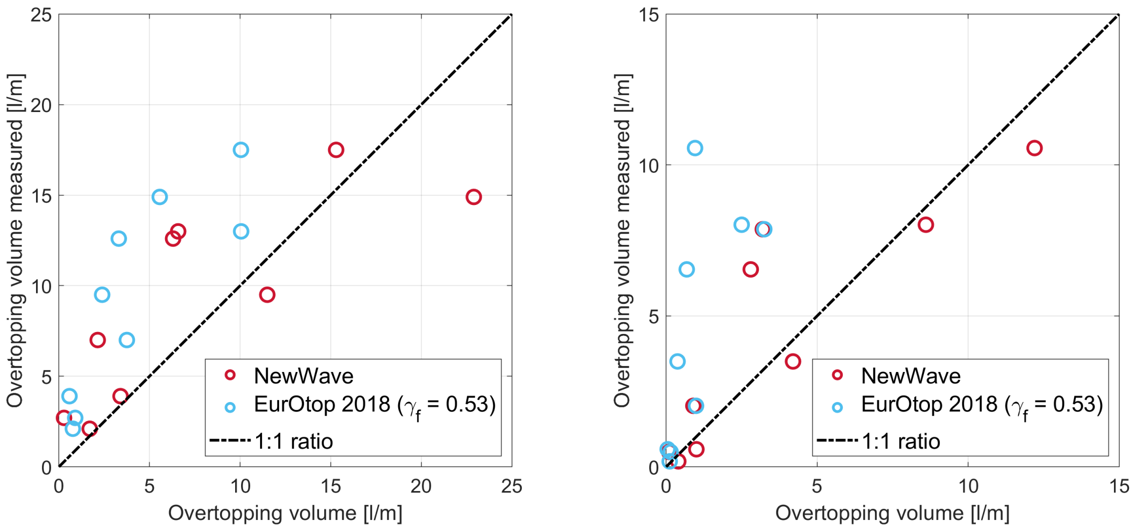

(a) Non-protruding wave wall cases.

(b) Protruding wave wall cases.

Figure 7.4: Maximum overtopping volumes, including a comparison between three different methods and measurements: NewWave, EurOtop 2018 (γ_f = 0.40) and EurOtop 2018 (γ_f = 0.53); (a) for non-protruding wave wall cases; (b) for protruding wave wall cases.

The NewWave overtopping volumes are compared with the measured and empirically (EurOtop 2018) obtained maximum overtopping volumes in the following Table 7.2.

Geometry	Protruding			Non-protruding				
Case	$V_{NewWave}$ [l/m]	$V_{Measured}$ [l/m]	$V_{EurOtop}$ [l/m]	Case	$V_{NewWave}$ [l/m]	$V_{Measured}$ [l/m]	$V_{EurOtop}$ [l/m]	Ursell
A1T201	1.0	0.58	0.05	A3T201	3.4	3.92	0.58	6.3
A1T202	4.2	3.49	0.38	A3T202	11.5	9.56	2.39	8.8
A1T203	12.2	10.56	0.96	A3T203	22.9	14.92	5.56	11.7
A1T204	0.4	0.18	0.12	A3T204	1.7	2.10	0.77	3.5
A1T205	2.7	6.54	0.68	A3T205	6.2	12.56	3.30	5.2
A1T206	8.6	8.02	2.5	A3T206	15.3	17.53	10.05	7.8
A1T207	0.1	0.49	0.15	A3T207	0.3	2.74	0.90	1.5
A1T208	0.9	2.02	0.98	A3T208	2.1	7.03	3.75	2.4
A1T209	3.2	7.87	3.25	A3T209	6.6	13.01	10.06	3.7

Table 7.2: Maximum overtopping volumes, including a comparison between the NewWave, the corrected EurOtop 2018 method and measured maximum overtopping volumes for protruding and non-protruding wave wall cases. The Ursell number describes the degree of non-linearity for each case.

In Section 6.6.5 (see Chapter 6) the NewWave overtopping volumes ($V_{NewWave}$) were evaluated against the maximum measured overtopping volumes ($V_{Measured}$). It was concluded that the NewWave overtopping volumes, when plotted against the degree of non-linearity of the considered wave conditions, showed a similar trend with measurements (similar equations in Figures 7.5 and 7.6 below). The exact same figures are reconstructed and the updated EurOtop 2018 maximum overtopping volumes are added. From these figures it can be deduced that the updated EurOtop 2018 results show an underestimating trend (also seen in Figure 7.4 above) compared to the measured maximum volumes for both the non-protruding and protruding wave wall cases.

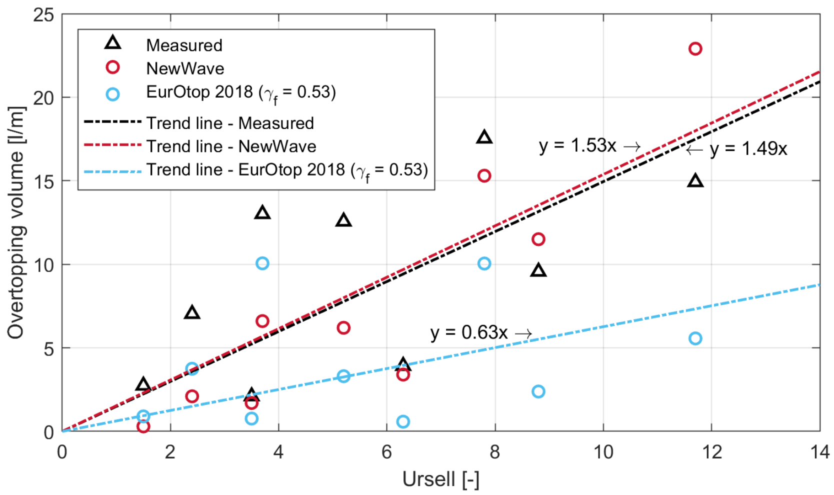

Figure 7.5: The maximum overtopping volume plotted against the Ursell number, including a comparison between: the NewWave methodology, the updated EurOtop 2018 approach and the measurements for non-protruding wave wall cases.

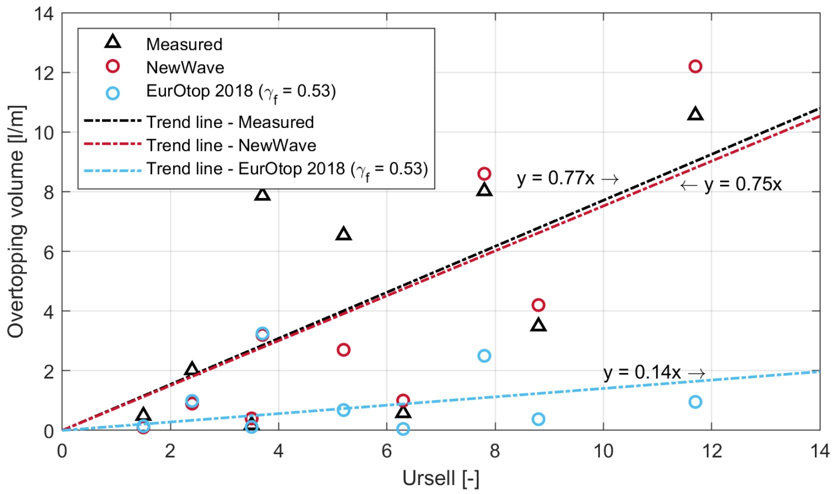

Figure 7.6: The maximum overtopping volume plotted against the Ursell number, including a comparison between: the NewWave methodology, the updated EurOtop 2018 approach and the measurements for protruding wave wall cases.

The comparison in terms of RMSE values between: the proposed NewWave methodology, the updated EurOtop 2018 methodology and measurements is done in Table 7.3 below.

	Non-protruding	Protruding
Method	RMSE [l/m]	
EurOtop 2018 (γ_f = 0.53)	5.91	4.59
NewWave	4.53	2.15

Table 7.3: RMSE and error values of two proposed methods for the estimation of maximum overtopping volume.

The measured average maximum volumes of the respective cases are: 9.26 l/m for non-protruding and 4.41 l/m for protruding wave wall cases. From the above it can be concluded that the proposed NewWave methodology, referred to as (i) in Chapter 6, shows improved results compared to the updated EurOtop 2018 methodology. The NewWave methodology shows the lowest RMSE values for both protruding (RMSE = 2.15 l/s/m) and non-protruding (RMSE = 4.53 l/s/m) wave wall cases. One of the conclusions of Chapter 3 was that for increasing complexity of a rubble mound breakwater (wave walls) the EurOtop 2018 manual increases in uncertainty. Therefore, for rubble mound breakwaters with increasing complexity the NewWave proposed methodology can be adopted as an improved estimator (lowest RMSE values; see Table 7.3 above) of the maximum overtopping volume. Most importantly, this can be done without knowing the average overtopping discharge of the considered storm, saving computational effort and time, which can then be used to study various configurations or increased breakwater complexity (berms, recurved wave wall, etc.).

7.3.2. Comparison of average overtopping discharge - NewWave approach

In the present section the NewWave average overtopping discharges are compared with the updated EurOtop 2018 approach and measurements. As inferred earlier in Chapter 3, the original EurOtop 2018 approach under-estimated the measurements. Therefore, only the updated EurOtop 2018 approach is used in the comparison with the NewWave methodology and measurements. In Chapter 6 and Section 6.7 the proposed methodology, where the NewWave average overtopping discharge is calculated using the inverse q to V EurOtop 2018, was explained. The NewWave overtopping volumes were applied as input. In Section 7.3 the updated roughness (γ_f = 0.53) was used to compute the EurOtop 2018 maximum overtopping volumes, which were evaluated against the NewWave overtopping volumes. Therefore, to be coherent along this research, the updated roughness (γ_f = 0.53) was preferred even if the original roughness (γ_f = 0.40) performed best. The NewWave average overtopping discharges are displayed with the EurOtop 2018 and measured average overtopping discharges in Figures 7.7 and 7.8 herebelow.

Non-protruding

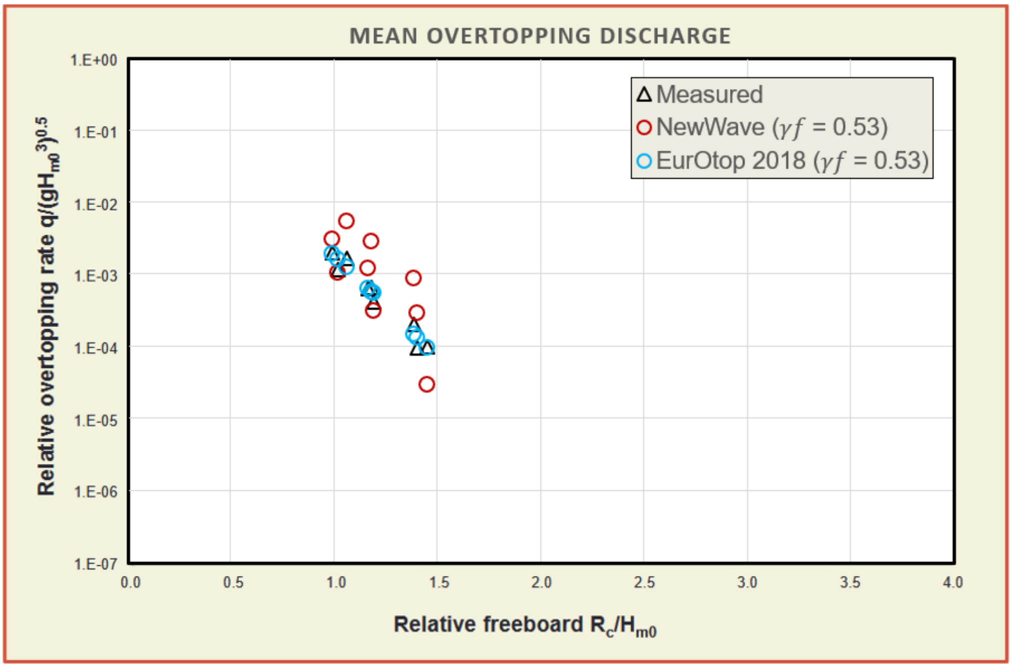

Figure 7.7: Mean overtopping discharge for non-protruding wave wall cases in terms of relative overtopping rate and relative freeboard, including a comparison between: physical laboratory measurements, the NewWave single event methodology and the EurOtop 2018 guideline (using the updated roughness).

In view of the foregoing, it can be concluded that for the non-protruding wave wall cases the NewWave overtopping discharges (red circles) show an over-estimating trend compared to measurements (black triangles). On the other hand, the updated EurOtop 2018 (cyan circles) results show a trend identical to the measurements.

Protruding

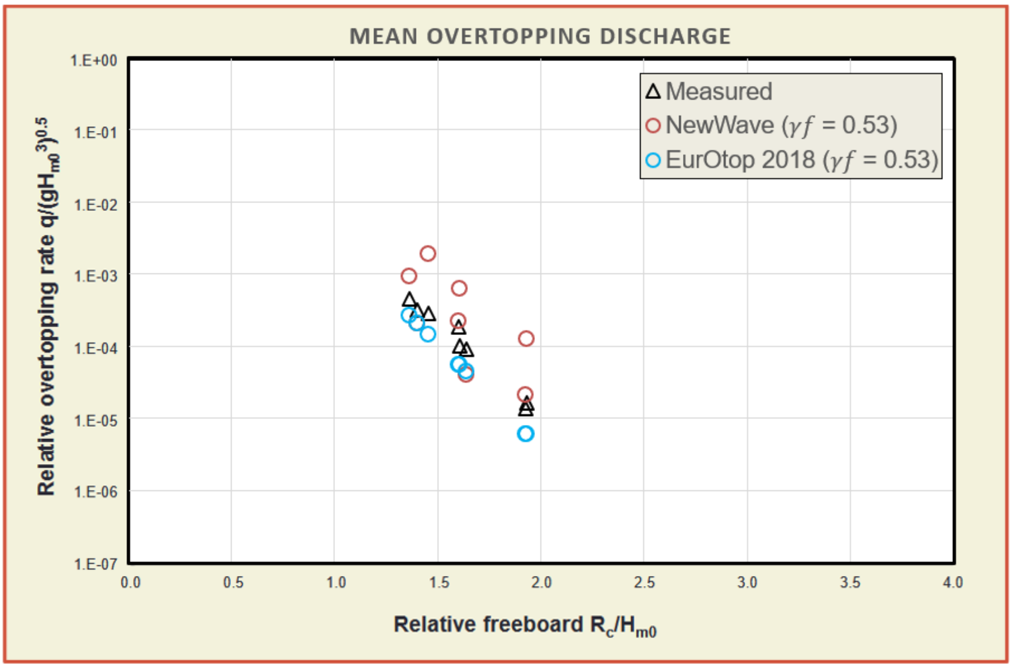

Figure 7.8: Mean overtopping discharge for protruding wave wall cases in terms of relative overtopping rate and relative freeboard, including a comparison between: physical laboratory measurements, the NewWave single event methodology and the EurOtop 2018 guideline (using the updated roughness).

For the protruding wave wall cases the NewWave overtopping discharges show an over-estimating trend compared to measurements, whereas the updated EurOtop 2018 results show an under-estimating trend compared to measurements. The over-estimated trend in both wave wall cases for the NewWave method can be explained as follows:

- The EurOtop 2018 (γ_f = 0.53) discharges showed excellent comparability with measurements. However, the resulting maximum overtopping volumes when adopting the q to V approach under-estimated the measurements (see Section 7.3.1 above).
- The NewWave overtopping volumes showed improved accuracy with measurements compared to the EurOtop 2018 volumes. As a consequence, using the NewWave overtopping volumes as input for the inverse EurOtop 2018 approach leads to an over-estimating trend compared to the updated EurOtop 2018 average discharges and therefore also to the measurements.

From Table 7.4 below it can further be deduced that the NewWave method (RMSE = 0.183 l/s/m) achieves lower accuracy when compared to the advised EurOtop 2018 method (γ_f = 0.53; RMSE = 0.029 l/s/m). The measured average overtopping discharges over the 18 considered cases were: non-protruding q = 0.122 l/s/m and protruding q = 0.026 l/s/m. Additionally, the NewWave method shows high scatter as shown in Figures 7.7 and 7.8 and is undesired when used as design tool.

	Non-protruding	Protruding	Overall
Method	RMSE [l/s/m]		
EurOtop 2018 (γ_f = 0.53)	0.037	0.017	0.029
NewWave	0.234	0.099	0.183

Table 7.4: Reported errors when using the various methodologies to compute q compared to the measured average overtopping discharges.

7.4. Provisional conclusions

The designer can choose the average overtopping discharge (q) or the maximum overtopping volume (V_{max}) as design criterion. In the present research different methods were proposed to assess these two properties.

As concluded in Chapter 3, the original EurOtop 2018 methodology revealed to be inaccurate in assessing the average overtopping discharge (q) and was therefore re-evaluated and updated (from γ_f = 0.40 to γ_f = 0.53). Moreover, of the various methods to assess the average overtopping discharge during a design storm, CoastalFOAM (modelling approximately 500 waves; approximately 4 days simulation time) showed the highest comparability with measurements in case of non-protruding wave wall cases. On the other hand, CoastalFOAM showed to be less capable in assessing overtopping discharges for protruding wave wall cases, mainly the small overtopping discharge case. A possible cause was the numerical diffusion in the overtopping region. This diffusion is enhanced in case of protruding wave wall cases (as explained in Section 5.5.4). It is therefore the updated EurOtop 2018 that performed the best considering the protruding wave wall cases, which is also quick and easy to use. However, CoastalFOAM is capable of modelling instantaneous overtopping discharges, velocities, pressures and forces simultaneously, which is an advantage when compared to empirical formulas. Additionally, a first attempt is made in this research to assess q using V_{max} as input. Yet, the proposed NewWave methodology showed to be the least accurate in assessing the average overtopping discharge and requires further improvement.

To assess the maximum overtopping volume (V_{max}) during a design storm, the NewWave methodology showed more promising results compared to the updated EurOtop 2018 method. The advantage of the NewWave methodology is that it provides the engineer with an important design property (V_{max}) within approximately 1.5 hours. This would permit to quickly evaluate different breakwater cross sections in quite some detail in one day, considering not only wave overtopping but also forces. In Chapter 5 it was also shown that the individual volumes within a 500 waves simulation were modelled with good accuracy using the calibrated (A5) model set-up. Therefore, CoastalFOAM is also capable of assessing the maximum volumes occurring within a storm. Yet, the computational time required is high when compared to the NewWave approach.

From all the foregoing, it is worth to consider the following proposed methods:

- Applying the NewWave methodology in CoastalFOAM as first estimator for the maximum overtopping volume instead of the EurOtop 2018 approach or running 500 waves in CoastalFOAM.
- Using the calibrated CoastalFOAM set-up (500 waves) to assess small (with an adequate grid resolution), medium and large overtopping discharges as it provides more information compared to empirical methods. When a quick assessment is required, the updated EurOtop 2018 is advised.

8

Discussion, conclusions and further research

8.1. Discussion

The present research discusses wave overtopping over rubble mound breakwaters, in terms of average overtopping discharges and maximum overtopping volumes. It focuses on the validation and applicability of a numerical model to accurately quantify average overtopping discharges and maximum overtopping volumes. The results show the accuracy of the numerical model compared to measurements, allowing the designer to consider whether the numerical model could be implemented instead of empirical methods within the preliminary design stages of breakwaters. In making this assessment, the designer should take particular care of certain aspects when considering the calibration of the numerical model (see Sections 8.1.1 to 8.1.3) and the proposed NewWave methodologies (see Sections 8.1.4 to 8.1.6).

8.1.1. Turbulence

Turbulence was not directly modelled in this research (see Section 4.3.4). Wave breaking played little or no role in the majority of the cases, since the type of wave-breaking was defined as surging (ξ > 2.5-3.0). Therefore, it was assumed that the turbulence generated outside the structure would have negligible effect on assessing the wave overtopping. The turbulence within the structure was accounted for by calibrating the resistance coefficients: α, β and KC. On the other hand, if the designer wants to apply the numerical model in wave-breaking (ξ < 2.5-3.0) conditions, the turbulence outside the structure can not be neglected and should be modelled for. As a consequence, the porous flow coefficients should be re-calibrated to not account twice for turbulence within the structure.

8.1.2. Porous flow coefficients and the degree of openness

When using the porous flow coefficients proposed by Jacobsen et al. (2018) (α = 1,000, β = 1.1 and KC = 10,000), the obtained reflection coefficients were too high. Losada et al. (2016) performed a literature study listing multiple set of porous flow coefficients used in past numerical and physical rubble mound breakwater studies. In the present research some of these sets were tested. Among the tested configurations the set-up by Losada et al. (2008) showed the most promising results in terms of modelled reflection coefficients when compared to measurements and was therefore selected. This research also showed that when using the reflection coefficient as selection criterion, multiple different combinations of porous flow coefficients can be accepted. Yet, the sensitivity analysis showed that the porous flow coefficients influence the overtopping results. The designer should therefore be aware of the sensitivity of such parameters and select them adequately by considering additional evaluation criteria (such as wave breaking and overflow over the slope and crest of the breakwater). Another sensitive parameter which the designer should consider is the degree of openness of the front of the wave wall, a computational solution for air entrapment and over-estimated forces against the wall developed by Jacobsen et al. (2018). For protruding wave wall cases the degree of openness showed to considerably influence the average overtopping discharge and individual overtopping events. The parameter can be altered in order to achieve improved comparability with measurements. Yet, in this research the parameter was kept constant on the reported value, as suggested by Jacobsen et al. (2018).

8.1.3. Overtopping events

For certain parts of this research individual measured overtopping events were needed for comparison with model outcomes. However, no instantaneous overtopping discharges, from which individual events could be characterised, were provided with the available data. The measurements contained cumulative overtopping curves, which were used to identify individual overtopping events. The latter were determined by taking the difference between the upper overtopping volume and the lower overtopping volume of a vertical increment within one peak period of the considered case. The maximum overtopping volume was then defined as the highest value of the identified individual overtopping volumes. The cumulative overtopping curve could thus be transformed to an instantaneous discharge. However, due to the sloshing behaviour (dynamic) within the measuring overtopping tray, it was difficult to distinguish individual overtopping events. As a consequence, the cumulative overtopping curves were used. Yet, very small overtopping events could not be determined as they were not visible in the cumulative overtopping curve. The aforementioned technique is not accurate and could induce errors. Nevertheless, it was the best method available.

8.1.4. First-order wave generation

A first-order wave generation was used to generate the NewWave profile at focus location (see Section 6.4.2). Using a first-order wave generation in intermediate water depths introduced errors, referred to as "spurious waves", which increased in magnitude for increasing non-linearity (see Section 6.6.2). These error waves consisted of low frequency waves travelling ahead of the NewWave group and high frequency waves trailing behind. The latter were disregarded as they did not have a direct influence on the overtopping results. On the contrary the low frequency waves, causing a set-up in front of the focused wave group, do influence run-up levels and overtopping quantities, as reported by Orszaghova et al. (2014) and Whittaker et al. (2017). In the present research for both non-protruding and protruding wave wall cases the modelled overtopping volumes showed similar trend lines compared to the maximum measured overtopping volumes. Nonetheless, for increasing degree of non-linearity the modelled maximum overtopping volumes over-estimated the measurements. It was therefore hypothesised that the low frequency waves may have caused the found over-estimations, of which the designer should be aware when using the proposed methodology in intermediate to shallow waters.

8.1.5. Crest elevation

One of the input parameters for NewWave profile is the desired crest elevation (η_{goal}). The η was roughly estimated by dividing the design wave height by two ($H_{0.1\%}/2$). Furthermore, the design wave height ($H_{0.1\%}$) was extracted from a Composite Weibull distribution. However, using the latter in cases of horizontal bottoms introduces errors (Van Os et al., 2011), under-estimating high wave heights (Caires and Van Gent, 2012).

8.1.6. EurOtop 2018

The methodology proposed by the EurOtop 2018 manual is used in the present research to assess the maximum overtopping volume (V_{max}) given the average overtopping discharge (q). When using this technique the designer assumes that the waves are Rayleigh distributed in front of the rubble mound breakwater and therefore also the run-up levels, which is a questionable assumption in intermediate waters. Furthermore, to calculate the probability of overtopping (P_{ov}) the factor 0.02 is altered to 0.001 as the V_{max} is the volume caused by the $H_{0.1\%}$ exceedance wave height in this research. Last, as shown in Chapters 3 and 7, the choice of the roughness coefficient, used in the EurOtop 2018 approach, influences the accuracy to assess the average discharges and maximum overtopping volumes.

8.2. Conclusions

This final Section provides the main conclusions which can be inferred from the present research given the research objective formulated in Chapter 1:

> "Demonstrate that CFD (Computational Fluid Dynamics) can be applied to accurately and efficiently simulate two-dimensional overtopping of rubble mound breakwaters, in terms of average overtopping discharges and individual overtopping volumes."

The following sub-research questions were extracted (in Chapter 1) from the research objective:

1. Which methods do exist and to what extent are they able to accurately assess average overtopping quantities over rubble mound breakwaters with protruding and non-protruding wave wall?
2. Can the proposed numerical model accurately capture small to large average overtopping discharges whilst considering 500 incident waves, replacing empirical methods in the preliminary design stages of rubble mound breakwaters?
3. Can a methodology be developed which accurately captures the maximum overtopping volume and average overtopping discharge by modelling only a couple of incident waves, therefore reducing computational time?

WHICH METHODS DO EXIST AND TO WHAT EXTENT ARE THEY ABLE TO ACCURATELY ASSESS AVERAGE OVERTOPPING QUANTITIES OVER RUBBLE MOUND BREAKWATERS WITH PROTRUDING AND NON-PROTRUDING WAVE WALL?

Multiple tools exist for the design of rubble mound breakwaters: empirical methods, numerical models and physical laboratory experiments, ordered in increasing accuracy, time and money. Within the preliminary design stages of rubble mound breakwaters engineers usually opt for empirical methods, e.g. EurOtop 2018 when considering wave overtopping as failure criterion. Nonetheless, this research showed that the current EurOtop 2018 approach (using γ_f = 0.40) under-estimates the average overtopping discharges by a factor ranging between 2-273x compared to measurements. The under-estimation increases for increasing geometrical complexity of the breakwater (protruding wave wall). The roughness coefficient was therefore re-calibrated, for the EurOtop 2018 approach, based on the 54 available physical laboratory experiments. The obtained roughness coefficient, considering both the non-protruding and protruding wave wall cases, had a mean of 0.53 and a standard deviation of 0.05. The present research therefore agreed with Molines and Medina (2015) that when using the original EurOtop 2018 roughness (γ_f = 0.40) the measurements are under-estimated. Consequently, the re-evaluated roughness coefficients by Molines and Medina (2015) were introduced and applied to the used data ranges. Among all the considered empirical approaches (Molines and Medina 2016, the Neural Network and the EurOtop 2018) with re-evaluated roughness coefficients, the EurOtop 2018 (using γ_f = 0.53) performed best for both non-protruding (RMSE = $6.86 \cdot 10^{-2}$ (l/s/m)) and protruding (RMSE = $3.19 \cdot 10^{-2}$ (l/s/m)) wave wall cases. **In conclusion, accurate empirical methods do exist. However, this research showed that the roughness factor should be carefully and properly selected and that, in case of doubt, it is advisable to perform a physical model test to confirm the proposed design.**

CAN THE PROPOSED NUMERICAL MODEL ACCURATELY CAPTURE SMALL TO LARGE AVERAGE OVERTOPPING DISCHARGES WHILST CONSIDERING 500 INCIDENT WAVES, REPLACING EMPIRICAL METHODS IN THE PRELIMINARY DESIGN STAGES OF RUBBLE MOUND BREAKWATERS?

The numerical model was set-up according to Jacobsen et al. (2018) as starting point for the validation of wave overtopping over rubble mound breakwaters with protruding and non-protruding wave wall. A calibration procedure was proposed in which: the incoming wave conditions were calibrated, the reflection of the structure was calibrated and the total surface elevation was evaluated. The calibration was carried out for a medium overtopping with non-protruding wave wall case. Some important findings concerning the calibration of the model are outlined below:

- The original steering file generated under-dimensioned incoming wave conditions (8% in terms of spectral wave height H_{m0}) compared to measurements. It was therefore decided to amplify the wave paddle steering file with a frequency dependent amplification factor.

- The incoming wave conditions were still (after the performed amplification) under-dimensioned (15% in terms of H_{m0}) in OpenFOAM and this was mainly caused by a coupling issue between OceanWaves3D and OpenFOAM. The coupling between OceanWaves3D and OpenFOAM was improved (difference <5% in terms of H_{m0}) by increasing the resolution (2x) in propagating wave direction of the OceanWaves3D grid.
- From the performed reflection analysis method it was concluded that the reflection of the structure in the numerical flume was too high. The bulk reflection of the structure was altered by re-assessing the porosity (n), the grading (D_{n50}) and the porous flow coefficients (α, β and KC).

The calibrated numerical model, in this report referred to as CoastalFOAM[1], was thereafter used for the evaluation of six overtopping cases. The cases were pre-selected to cover small to large average overtopping discharges and varying bulk reflection coefficients, showing the strength (or weakness) of CoastalFOAM. The calibrated numerical results were compared by means of RMSE relative to the average measured discharge with empirical methods and the uncalibrated model results by Boersen et al. (2019). CoastalFOAM (ratio = RMSE/$q_{mes,average}$ = 0.07) performed the best compared to the updated EurOtop 2018 (γ_f = 0.53; ratio = 0.41) approach and the uncalibrated model (ratio = 0.16) for the non-protruding wave wall cases. The updated EurOtop 2018 (γ_f = 0.53; ratio = 0.65) method showed the highest accuracy compared to the uncalibrated model (ratio = 1.67) and CoastalFOAM (ratio = 0.97) when compared to measurements in case of protruding wave wall cases. However, this was mainly caused by the over-estimation of CoastalFOAM for the protruding wave wall with small overtopping case. This over-estimation was caused by multiple modelled small overtopping events which were not observed during the physical laboratory experiments. Possible causes were identified and studied more closely in the sensitivity analysis (e.g. the porous flow coefficients, the degree of openness of the wave wall and the grid size in the overtopping region). A few key findings regarding the performed sensitivity analysis are mentioned below:

- The porous flow coefficients influence the wave-structure process (e.g. wave breaking and the flow over the crest of the breakwater). The reflection coefficient was used as selection criterion. However, numerical simulations characterised by equal reflection coefficients, achieved by adopting different sets of porous flow coefficients, showed differences in the cumulative overtopping curves in terms of individual overtopping volumes and average discharges. These differences show how sensitive the porous flow coefficients are in assessing the wave overtopping.
- The degree of openness of the wave wall is a sensitive parameter, where a change from 3% to 0.5% resulted in a 42% increase in terms of average overtopping discharge.
- The grid size in the overtopping region is important when modelling small overtopping discharges and volumes to avoid numerical diffusion. The latter was reduced by increasing the grid resolution (from 0.0125 m to 0.0016 m; increased simulation time by a factor 2.35x is reported).

From all the above it can be concluded that CoastalFOAM can be used, instead of the current empirical methods, within the design cycle of rubble mound breakwaters. However, according to what has emerged so far, CoastalFOAM has shown to be less accurate in calculating small overtopping discharges as opposed to medium and large. Additionally, CoastalFOAM is capable of modelling instantaneous overtopping discharges (individual events), forces and pressures (not used in this research), which is an advantage compared to empirical methods. Therefore, its use should be encouraged. In order to assess the overtopping in CoastalFOAM a cross section is needed. To establish that cross section the updated EurOtop 2018 (γ_f = 0.53) can be used as starting point.

CAN A METHODOLOGY BE DEVELOPED WHICH ACCURATELY CAPTURES THE MAXIMUM OVERTOPPING VOLUME AND AVERAGE OVERTOPPING DISCHARGE BY MODELLING ONLY A COUPLE OF INCIDENT WAVES, THEREFORE REDUCING COMPUTATIONAL TIME?

In the present research two methodologies were developed to:

- (i) assess V_{max}
- (ii) assess q using V_{max}

[1]CoastalFOAM is Royal HaskoningDHV's short for OpenFOAM + Waves2Foam etc.; Figure 4.2 in Chapter 4 explains the framework of CoastalFOAM.

i: methodology to assess V_{max}

To generate the desired surface elevation at focus location a first-order wave generation was employed. However, using the latter to generate a NewWave profile in intermediate waters created ”spurious waves”. Further, from the comparison between the theoretical and the OceanWaves3D profiles it was concluded that for increasing degree of non-linearity the magnitude of the ”spurious waves” increased. The desired crest height used as input for the NewWave profile was extracted from a Composite Weibull distribution (CWD; Battjes and Groenendijk (1999)) and had a 0.1% exceedance value. By doing so the maximum measured overtopping volumes (occurring within approximately 1000 waves) could be compared with the volumes induced by the NewWave profiles. The generated NewWave profiles were modelled in CoastalFOAM and maximum overtopping volumes captured. The comparison was done for 18 cases (9 protruding and 9 non-protruding). The maximum overtopping volumes obtained with the proposed methodology showed excellent agreement with measurements. However, for increasing Ursell number the modelled maximum overtopping volumes over-estimated the measurements. The set-up in front of the NewWave, which increased for increasing Ursell number, was pointed out as possible cause. The EurOtop 2018 also presents a technique to estimate the maximum overtopping volume given the average overtopping discharge. However the updated (γ_f = 0.53) approach under-estimated the maximum measured overtopping volumes. Upon plotting the modelled, empirical and measured maximum overtopping volumes against each other, it was found that: the proposed NewWave methodology displayed improved agreement with measurements. The calculated RMSE values when compared with measurements for both non-protruding (NewWave RMSE = 4.53 l/m; EurOtop 2018 RMSE = 5.91 l/m) and protruding wave wall (NewWave RMSE = 2.15 l/m; EurOtop 2018 RMSE = 4.59 l/m) cases were lower when compared to the considered empirical method. **In view of these results, it can be concluded that this NewWave methodology can be used for preliminary design considerations using V_{max}, for both ULS and SLS, instead of the EurOtop 2018 proposed methodology.**

ii: methodology to assess q using V_{max}

The maximum modelled overtopping volumes ($V_{NewWave}$), were used as input for the reversed EurOtop 2018 (using γ_f = 0.53) method to compute the average overtopping discharge. This methodology, named the ”single event” approach, consists in modelling only one NewWave profile to find q. From the comparison between the EurOtop 2018 (updated γ_f = 0.53; RMSE = 0.029 l/s/m) and the NewWave average discharges (RMSE = 0.183 l/s/m), it was concluded that the NewWave method achieves lower accuracy when compared to the updated EurOtop 2018. **To assess the average overtopping discharge, it is therefore advisable to use the updated EurOtop 2018 technique, when applicable, instead of the NewWave methodology.**

Final conclusions

Having regard to all the foregoing, the following conclusions can be drawn:

- CoastalFOAM can be used, instead of empirical methods, to assess average overtopping discharges within the preliminary design stages of rubble mound breakwaters. CoastalFOAM showed excellent agreement with measurements for large and medium overtopping cases (both non-protruding and protruding), while revealing to be less accurate for small overtopping cases.
- To assess the maximum overtopping volume over a rubble mound breakwater, the proposed NewWave methodology can be used instead of the EurOtop 2018 proposed methodology or the 500 waves simulation.
- The total numerical time required to model and process a NewWave profile in CoastalFOAM is approximately 1.5 hours (single event). The NewWave proposed methodology is therefore more efficient when compared to the 500 waves simulations.

8.3. Recommendations

Although the calibrated numerical model was proven to be capable to predict surface elevation time series, average overtopping discharges and individual overtopping events with sufficient accuracy, aspects that require improvement have been identified and are listed in degree of importance as recommendations for further research (see Sections 8.3.2 to 8.3.8). Furthermore, a methodology is recommended to calibrate CoastalFOAM, should it be used in other projects (see Section 8.3.1).

8.3.1. Calibration procedure of CoastalFOAM

When using CoastalFOAM to design a rubble mound breakwater a designer has two options: using a numerical model which is calibrated through physical laboratory experiments (see Figure 8.2) or using an uncalibrated model (validated in this research). Depending on the availability of physical experiments, this research recommends to follow the methodology depicted in Figure 8.1.

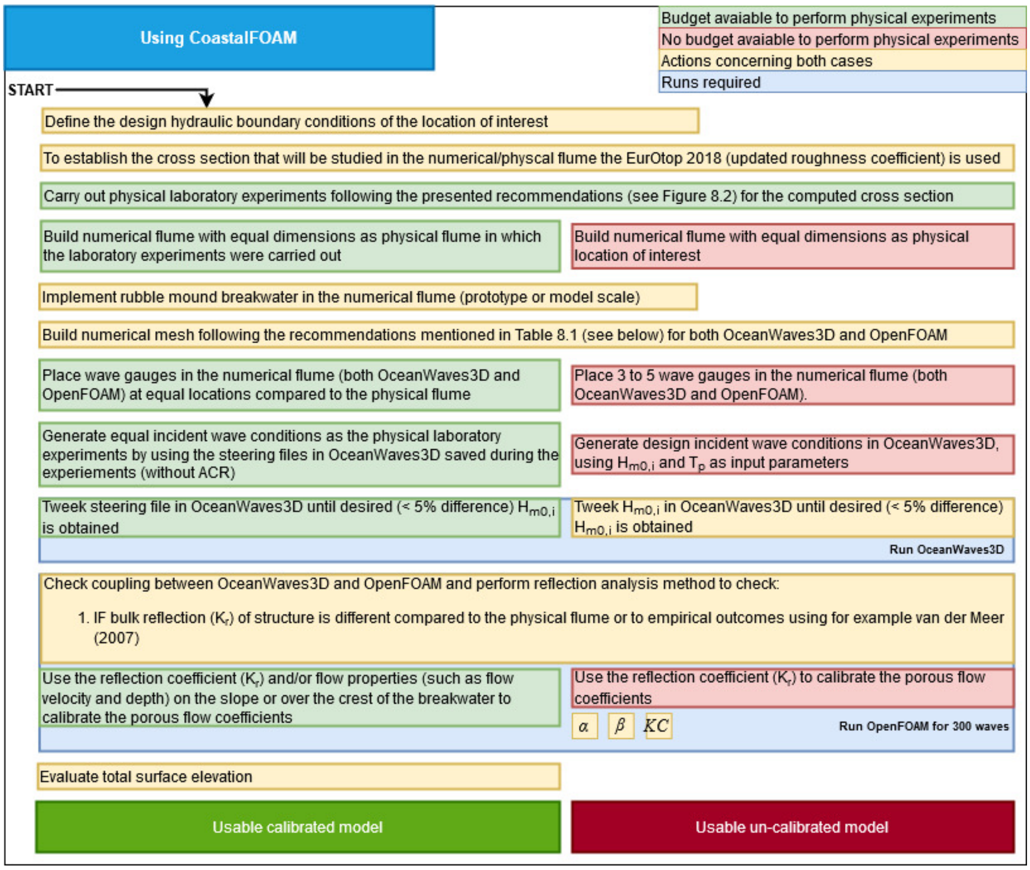

Figure 8.1: Recommended methodology to follow at start of the design of a rubble mound breakwater when CoastalFOAM is to be used to assess the amount of wave overtopping.

The used and recommended mesh resolutions, applied around the water level in both numerical domains, to ensure the quality of both the coupling (between OpenFOAM and OceanWaves3D) and the wave propagation, are listed in Table 8.1 herebelow. The vertical resolution in OceanWaves3D was fixed for all cases consisting of twelve grid points. The vertical distance between these twelve grid points reduced closer to the water level (vertically clustered grid). The mesh properties are given in function of the incident wave parameters, making the resolution case specific.

Recommended mesh properties for wave propagation	Δx [m]	Number of points per L [-]	Δy [m]	Number of points per H_{m0}
OpenFOAM	0.0063	635	0.0063	20
OceanWaves3D	0.024	165	-	-

Table 8.1: Recommended mesh properties concerning the wave propagation in both numerical domains, according to the present research.

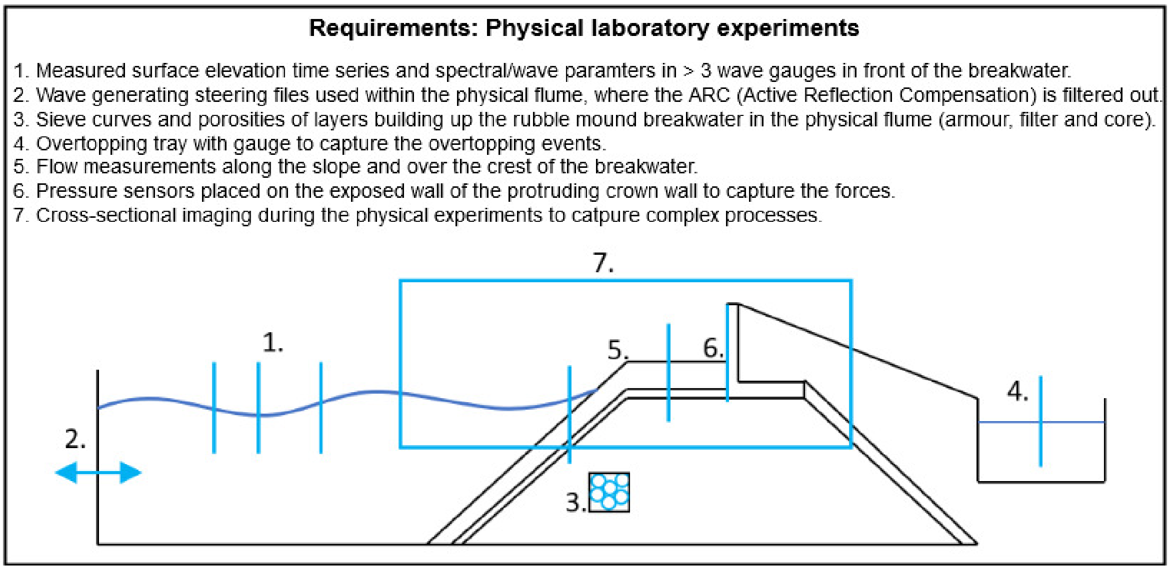

Figure 8.2: In the event that physical laboratory experiments are to be performed the present research recommends to carry out steps 1 to 7 and collect the best possible data to calibrate the numerical model.

Considering further improvement and extension of the numerical model:

8.3.2. OceanWaves3D and OpenFOAM coupling

In this research the coupling between OceanWaves3D and OpenFOAM for steep waves (extremes) was improved by increasing the resolution in propagating direction (x-axis). However, this solution increased computational time (approximately by a factor 2 on average over all cases). It is therefore recommended to look at numerically more attractive solutions to improve the coupling.

8.3.3. Forces on protruding wave wall

In the present research the numerical model was set-up according to Jacobsen et al. (2018) as starting point. Jacobsen et al. (2018) used this set-up to validate: the numerical solution to avoid air entrapment (degree of openness of the wave wall) and the forces acting on a protruding wave wall. Nonetheless, discrepancies in the set-up were identified and tackled, and this resulted in a calibrated model. The calibrated model showed improved results when compared with measurements in terms of the cumulative overtopping curve. As a consequence, it is expected that the calibrated model will show differences with the reported findings by Jacobsen et al. (2018) concerning the forces acting on the protruding wave wall. It is thus recommended to use the calibrated model set-up and compare the outcomes with the findings reported in Jacobsen et al. (2018) in order to show if the advised degree of openness (3%) is still valid.

8.3.4. Bulk resistance structure

As shown by Losada et al. (2016) a wide set of dimensionless resistance coefficients (α, β and KC) has been used numerically to recreate the porous flow and resulting bulk reflection coefficients of the breakwater. First, it is recommended to use the presently selected set within another case study to see if the proposed coefficients are applicable to other situations. Second, as shown in this research, multiple sets of dimensionless coefficients can be used to correctly reconstruct the presence of the structure, defined by the reflection coefficient (K_r). Consequently, the designer should adopt a different evaluation methodology to select the set of porous flow coefficients, by accounting for additional evaluation criteria (for example the flow along the slope or over the crest of the breakwater), and see what the influence is on the overtopping results.

8.3.5. Hydraulic boundary conditions

The validation procedure considered the variation of wave height (H_{m0}), peak period (T_p) and geometry (R_c, protruding and non-protruding). Nevertheless, the variation of the mean water level was discarded to reduce workload. However, the water level is an important hydraulic parameter when considering wave overtopping, where q is correlated to R_c (Van der Meer et al., 2018). It is therefore recommended to perform additional validation runs with varying water levels for which data is available, as shown in Chapter 2.

8.3.6. Increased geometrical complexity

The model was validated for a conventional rubble mound breakwater with or without protruding wave wall. Yet, many other types of rubble mound breakwaters do exist, e.g. rubble mound breakwaters with toe structure, berm or multiple protruding wave walls. It is thus recommended to test and validate the proposed calibration methodology for rubble mound breakwaters for which no empirical methodologies exist.

Considering the proposed NewWave methodologies:

8.3.7. Second-order wave generation

The first order wave generation introduced spurious waves which increased for increasing non-linearity. One possible solution is to use the second order wave generation by Schaffer (1995). It is recommended to compare the overtopping results considering a NewWave profile generated with a first or second order wave generation. The comparison will show how big the influence of the spurious waves is on the overtopping results when considering wave overtopping over rubble mound breakwaters, as similar to what has been done for sloping foreshores by Orszaghova et al. (2014).

8.3.8. Crest elevation

Other methods do exist to obtain the crest height from the design wave height (instead of assuming $\eta = H/2$), which consider the water depth, deep water steepness and the slope of the foreshore to estimate the crest elevation using the cnoidal theory (Buhr Hansen, 1990). Another option is to run other type of numerical models (e.g. Mike 3 Wave FM model or SWASH) beforehand, to generate the incoming surface elevation time series (offshore to nearshore), giving an improved prediction of the $\eta_{0.1\%}$ value at the toe of the breakwater. This $\eta_{0.1\%}$ value is recommended and can thus be used as input for the proposed NewWave methodology.

References

W. Allsop, T. Bruce, J. M. Pearson, and J. Alderson. Violent wave overtopping at the coast, when are we safe? Impact wave-forces View project Input to the Concrete Manual View project. *Proceedings of the International Conference on Coastal Management*, pages 1–16, 2003. URL https://www.researchgate.net/publication/287547182.

P. Aminti and L. Franco. WAVE OVERTOPPING ON RUBBLE MOUND BREAKWATERS. 1988.

A. Antonini, R. Archetti, and A. Lamberti. Wave simulation for the design of an innovative quay wall: The case of Vlorë Harbour. *Natural Hazards and Earth System Sciences*, 17(1):127–142, 2017. ISSN 16849981. doi: 10.5194/nhess-17-127-2017.

C. Arrighi, H. Oumeraci, and F. Castelli. Hydrodynamics of pedestrians' instability in floodwaters. *Hydrology and Earth System Sciences*, 21(1):515–531, 2017. ISSN 16077938. doi: 10.5194/hess-21-515-2017.

J. A. Battjes and H. W. Groenendijk. Shallow foreshore wave height statistic. *Proc. Coastal Structures*, (January):29–35, 1999. URL http://repository.tudelft.nl/view/ir/uuid:fe03dda9-40d9-4046-87fb-459f01fcd3d3/.

E. Berberović, N. P. Van Hinsberg, S. Jakirlić, I. V. Roisman, and C. Tropea. Drop impact onto a liquid layer of finite thickness: Dynamics of the cavity evolution. *Physical Review E - Statistical, Nonlinear, and Soft Matter Physics*, 79(3), 2009. ISSN 15393755. doi: 10.1103/PhysRevE.79.036306.

P. Besley. Wave overtopping of seawalls, design and assessment manual. *R\&D technical report W178*, (February):37, 1999. URL http://www.scribd.com/doc/7333031/-Over-Topping-Manual.

S. Boersen, O. Scholl, N. Jacobsen, and C. van der Lem. APPLYING A NUMERICAL WAVE FLUME TO PREDICT WAVE OVERTOPPING. In *38th IAHR World Congress*, number 1, page 10, Panama City, 2019.

M. Bozorgnia, J.-J. Lee, and F. Raichlen. Wave Structure Interaction: Role of Entrapped Air on Wave Impact and Uplift Forces. *Coastal Engineering Proceedings*, 1(32):57, 2012. ISSN 0589-087X. doi: 10.9753/icce.v32.structures.57.

A. P. Bradbury, N. W. H. Allsop, and R. V. Stephens. Hydraulic Performance of Breakwater Crown Walls. (March):1–108, 1988.

T. Bruce, J. W. van der Meer, L. Franco, and J. M. Pearson. Overtopping performance of different armour units for rubble mound breakwaters. *Coastal Engineering*, 56(2):166–179, 2009. ISSN 03783839. doi: 10.1016/j.coastaleng.2008.03.015. URL http://dx.doi.org/10.1016/j.coastaleng.2008.03.015.

J. Buhr Hansen. Periodic Waves in the Surf Zone: Analysis of Experimental Data. *Coastal Engineering*, 14:19–41, 1990.

S. Caires and M. R. Van Gent. Wave height distribution in constant and finite depths. *Proceedings of the Coastal Engineering Conference*, 2012. ISSN 0589-087X. doi: 10.9753/icce.v33.waves.15.

M. Castellino, P. Sammarco, A. Romano, L. Martinelli, P. Ruol, L. Franco, and P. De Girolamo. Large impulsive forces on recurved parapets under non-breaking waves. A numerical study. *Coastal Engineering*, 136:1–15, 2018. ISSN 03783839. doi: 10.1016/j.coastaleng.2018.01.012.

N. Chini and P. K. Stansby. Extreme values of coastal wave overtopping accounting for climate change and sea level rise. *Coastal Engineering*, 65:27–37, 2012. ISSN 03783839. doi: 10.1016/j.coastaleng.2012.02.009. URL http://dx.doi.org/10.1016/j.coastaleng.2012.02.009.

CIRIA, CUR, and CETMEF. *Chapter 5 of The Rock Manual. Physical processes and design tools (2nd edition)*. C683, CIRIA, London, 2007a.

CIRIA, CUR, and CETMEF. *Chapter 3 of The Rock Manual. Materials (2nd edition)*. C683, CIRIA, London, 2007b.

G. Cuomo, K. i. Shimosako, and S. Takahashi. Wave-in-deck loads on coastal bridges and the role of air. *Coastal Engineering*, 56(8):793–809, 2009. ISSN 03783839. doi: 10.1016/j.coastaleng.2009.01.005. URL http://dx.doi.org/10.1016/j.coastaleng.2009.01.005.

R. G. Dean and R. A. Dalrymple. Water Wave Mechanics for Engineers and Scientists. *Advanced Series on Ocean Engineering*, Volume 2, 1991.

J. Dekker, S. Caires, and M. R. van Gent. Reflection of non-standard wave spectra by sloping structures. *Proc. Coastal Structures*, pages 760–770, 2007.

A. P. Engsig-Karup, H. B. Bingham, and O. Lindberg. An efficient flexible-order model for 3D nonlinear water waves. *Journal of Computational Physics*, 228(6):2100–2118, 2009. ISSN 00219991. doi: 10.1016/j.jcp.2008.11.028. URL http://dx.doi.org/10.1016/j.jcp.2008.11.028.

L. Franco, M. de Gerloni, and J. W. van der Meer. Wave overtopping on vertical and composite breakwaters. *Coastal Engineering*, pages 1030–1045, 1994.

J. Geeraerts, P. Troch, J. De Rouck, H. Verhaeghe, and J. J. Bouma. Wave overtopping at coastal structures: prediction tools and related hazard analysis. *Journal of Cleaner Production*, 15(16):1514–1521, 2007. ISSN 09596526. doi: 10.1016/j.jclepro.2006.07.050.

M. Hayatdavoodi, B. R. Seiffert, and R. C. Ertekin. Experiments and computations of solitary-wave forces on a coastal-bridge deck. Part II: Deck with girders. *Coastal Engineering*, 88(November 2017):210–228, 2014. ISSN 03783839. doi: 10.1016/j.coastaleng.2014.02.007.

P. Higuera, J. L. Lara, and I. J. Losada. Simulating coastal engineering processes with OpenFOAM®. *Coastal Engineering*, 71:119–134, 2013. ISSN 03783839. doi: 10.1016/j.coastaleng.2012.06.002. URL http://dx.doi.org/10.1016/j.coastaleng.2012.06.002.

P. Higuera, J. L. Lara, and I. J. Losada. Three-dimensional interaction of waves and porous coastal structures using OpenFOAM®. Part II: Application. *Coastal Engineering*, 83:259–270, 2014a. ISSN 03783839. doi: 10.1016/j.coastaleng.2013.09.002. URL http://dx.doi.org/10.1016/j.coastaleng.2013.09.002.

P. Higuera, J. L. Lara, and I. J. Losada. Three-dimensional interaction of waves and porous coastal structures using OpenFOAM®. Part I: Formulation and validation. *Coastal Engineering*, 83:243–258, 2014b. ISSN 03783839. doi: 10.1016/j.coastaleng.2013.08.010. URL http://dx.doi.org/10.1016/j.coastaleng.2013.08.010.

B. Hofland, I. Wenneker, and P. V. Steeg. Short Test Durations for Wave Overtopping Experiments. *Conference Paper*, (SEPTEMBER):1–10, 2014.

T. J. Hsu, T. Sakakiyama, and P. L. Liu. A numerical model for wave motions and turbulence flows in front of a composite breakwater. *Coastal Engineering*, 46(1):25–50, 2002. ISSN 03783839. doi: 10.1016/S0378-3839(02)00045-5.

N. G. Jacobsen and J. Fredsoe. Formation and development of a breaker bar under regular waves. Part 2: Sediment transport and morphology. *Coastal Engineering*, 88:55–68, 2014. ISSN 03783839. doi: 10.1016/j.coastaleng.2014.01.015. URL http://dx.doi.org/10.1016/j.coastaleng.2014.01.015.

N. G. Jacobsen, D. R. Fuhrman, and J. Fredsøe. A wave generation toolbox for the open-source CFD library: OpenFoam®. *International Journal for Numerical Methods in Fluids*, 70(9):1073–1088, 2012. ISSN 02712091. doi: 10.1002/fld.2726.

N. G. Jacobsen, M. R. van Gent, and G. Wolters. Numerical analysis of the interaction of irregular waves with two dimensional permeable coastal structures. *Coastal Engineering*, 2015. ISSN 03783839. doi: 10.1016/j.coastaleng.2015.05.004.

N. G. Jacobsen, M. R. van Gent, and J. Fredsøe. Numerical modelling of the erosion and deposition of sand inside a filter layer. *Coastal Engineering*, 120(September 2016):47–63, 2017. ISSN 03783839. doi: 10.1016/j.coastaleng.2016.09.003. URL http://dx.doi.org/10.1016/j.coastaleng.2016.09.003.

N. G. Jacobsen, M. R. van Gent, A. Capel, and M. Borsboom. Numerical prediction of integrated wave loads on crest walls on top of rubble mound structures. *Coastal Engineering*, 142(April 2017):110–124, 2018. ISSN 03783839. doi: 10.1016/j.coastaleng.2018.10.004. URL https://doi.org/10.1016/j.coastaleng.2018.10.004.

B. Jensen, N. G. Jacobsen, and E. D. Christensen. Investigations on the porous media equations and resistance coefficients for coastal structures. *Coastal Engineering*, 84:56–72, 2014. ISSN 03783839. doi: 10.1016/j.coastaleng.2013.11.004. URL http://dx.doi.org/10.1016/j.coastaleng.2013.11.004.

P. Jonathan and P. H. Taylor. Irregular, non-linear waves in a spread sea. *Proceedings of the International Conference on Offshore Mechanics and Arctic Engineering - OMAE*, 1(Part A):9–16, 1995. ISSN 1528896X. doi: 10.1115/1.2829043.

Kansai Airport. FY2018 Consolidated Finanacial Resulst. Technical report, Kansai Region, 2019.

N. Karagiannis, T. Karambas, and C. Koutitas. Wave overtopping numerical simulation using OpenFoam. *E-Proceeding of the 36th IAHR world congress*, 2(2012):1–12, 2015.

J. L. Lara, M. del Jesus, and I. J. Losada. Three-dimensional interaction of waves and porous coastal structures. *Coastal Engineering*, 64:26–46, 2012a. ISSN 03783839. doi: 10.1016/j.coastaleng.2012.01.009. URL http://dx.doi.org/10.1016/j.coastaleng.2012.01.009.

J. L. Lara, M. del Jesus, and I. J. Losada. Three-dimensional interaction of waves and porous coastal structures. *Coastal Engineering*, 64:26–46, 2012b. ISSN 03783839. doi: 10.1016/j.coastaleng.2012.01.009. URL http://dx.doi.org/10.1016/j.coastaleng.2012.01.008.

P. Lin and S. A. Karunarathna. Numerical Study of Solitary Wave Interaction with Porous Breakwaters. *Journal of Waterway, Port, Coastal, and Ocean Engineering*, 133(5):352–363, 2007. ISSN 0733-950X. doi: 10.1061/(asce)0733-950x(2007)133:5(352).

G. Lindgren. Some Properties of a Normal Process Near a Local Maximum. the Annals of Mathematical Statistics. *Annals of Mathematical Statistics*, 41(6):1870–1883, 1970.

I. J. Losada, J. L. Lara, R. Guanche, and J. M. Gonzalez-Ondina. Numerical analysis of wave overtopping of rubble mound breakwaters. *Coastal Engineering*, 55(1):47–62, 2008. ISSN 03783839. doi: 10.1016/j.coastaleng.2007.06.003.

I. J. Losada, J. L. Lara, and M. del Jesus. Modeling the Interaction of Water Waves with Porous Coastal Structures. *Journal of Waterway, Port, Coastal, and Ocean Engineering*, 142(6):03116003, 2016. ISSN 0733-950X. doi: 10.1061/(asce)ww.1943-5460.0000361.

J. Molines and J. R. Medina. Calibration of overtopping roughness factors for concrete armor units in non-breaking conditions using the CLASH database. *Coastal Engineering*, 96:62–70, 2015. ISSN 03783839. doi: 10.1016/j.coastaleng.2014.11.008.

J. Molines and J. R. Medina. Explicit Wave-Overtopping Formula for Mound Breakwaters with Crown Walls Using CLASH Neural Network–Derived Data. *Journal of Waterway, Port, Coastal, and Ocean Engineering*, 142(3):04015024, 2016. ISSN 0733-950X. doi: 10.1061/(asce)ww.1943-5460.0000322.

J. Orszaghova, P. H. Taylor, A. G. Borthwick, and A. C. Raby. Importance of second-order wave generation for focused wave group run-up and overtopping. *Coastal Engineering*, 94(1959):63–79, 2014. ISSN 03783839. doi: 10.1016/j.coastaleng.2014.08.007.

B. T. Paulsen, H. B. Bingham, and H. Bredmose. Efficient computations of wave loads on offshore structures. (August):152, 2013.

J. Pearson, T. Bruce, L. Franco, J. W. van der Meer, M. Falzacappa, and R. Molino. Roughness factor. Technical report, Work package 4.4, D24 Report on additional tests, Part B, CLASH reportEVK3-CT-2001-00058, 2004.

Port of Rotterdam. Facts & Figures about the port, 2018. URL https://www.portofrotterdam.com/sites/default/files/feiten-en-cijfers-haven-rotterdam.pdf?token=PBcH9rLs.

T. Pullen, H. R. Wallingford, N. W. H. Allsop, T. Bruce, and C. Mitchel. The EurOtop Team Authors: Steering group: Funding bodies. (August), 2007.

A. Romano, G. Bellotti, R. Briganti, and L. Franco. Uncertainties in the physical modelling of the wave overtopping over a rubble mound breakwater: The role of the seeding number and of the test duration. *Coastal Engineering*, 103:15–21, 2015. ISSN 03783839. doi: 10.1016/j.coastaleng.2015.05.005.

H. A. Schaffer. Pergamon SECOND-ORDER WAVEMAKER THEORY FOR IRREGULAR WAVES. *Ocean Engineering*, 23(1):47–88, 1995.

J. G. Schierirck and H. J. Verhagen. *Introduction to bed, bank, shore protection*. Delft Academic Press, 2016.

B. R. Seiffert, M. Hayatdavoodi, and R. C. Ertekin. Experiments and computations of solitary-wave forces on a coastal-bridge deck. Part I: Flat Plate. *Coastal Engineering*, 88(November 2017):194–209, 2014. ISSN 03783839. doi: 10.1016/j.coastaleng.2014.01.005.

B. R. Seiffert, R. C. Ertekin, and I. N. Robertson. Wave loads on a coastal bridge deck and the role of entrapped air. *Applied Ocean Research*, 2015. ISSN 01411187. doi: 10.1016/j.apor.2015.07.010.

TAW. Technisch rapport golfoploop en golfoverslag bij dijken/Wave run-up and waveovertopping at dikes, 2002.

P. S. Tromans, A. R. Anatruk, and P. Hagemeijer. New model for the kinematics of large ocean waves application as a design wave. *Proceedings of the First International Offshore and Polar Engineering Conference, August 11, 1991 - August 16*, Ill(August):64–71, 1991.

J. Van den Bos, H. Verhagen, and C. Kuiper. Numerical modelling of wave reflection and transmission in vertical porous structures. page 16. ASCE - COPRI, 2015.

J. van der Meer and T. Bruce. New Physical Insights and Design Formulas on Wave Overtopping at Sloping and Vertical Structures. *Journal of Waterway, Port, Coastal, and Ocean Engineering*, 140(6): 04014025, 2013. ISSN 0733-950X. doi: 10.1061/(asce)ww.1943-5460.0000221.

J. Van der Meer, N. Allsop, D. R. Bruce, T., A. J., Kortenhaus, T. Pullen, H. Schüttrumpf, P. Troch, and B. Zanuttigh. EurOtop, 2018. Manual on wave overtopping of sea defences and related structures. An overtopping manual largely based on European research, but for worldwide application. page 320, 2018. URL www.overtopping-manual.com.

M. R. van Gent. Wave interaction with permeable coastal structures. *International Journal of Rock Mechanics and Mining Sciences & Geomechanics Abstracts*, 33(6):A277, 1995. ISSN 01489062. doi: 10.1016/0148-9062(96)81968-1.

M. R. van Gent. Physical model investigations on coastal structures with shallow foreshores; 2D model test with single and double-peaked wave energy spectra, 1999.

M. R. van Gent and G. Wolters. Granular slopes with open filters under wave loading. *Coastal Engineering*, 104:135–150, 2015. ISSN 03783839. doi: 10.1016/j.coastaleng.2015.06.004.

M. R. van Gent, H. F. van den Boogaard, B. Pozueta, and J. R. Medina. Neural network modelling of wave overtopping at coastal structures. *Coastal Engineering*, 54(8):586–593, 2007. ISSN 03783839. doi: 10.1016/j.coastaleng.2006.12.001.

M. R. van Gent, N. G. Jacobsen, and G. Wolters. Modelling of open filters under wave loading. (September):2–11, 2017. URL https://www.researchgate.net/publication/319877988.

J. Van Os, S. Caires, and M. Van Gent. Guidelines for metocean data analysis. *Proceedings of the International Offshore and Polar Engineering Conference*, (January 2011):290–297, 2011. ISSN 10986189.

D. Vanneste and P. Troch. 2D numerical simulation of large-scale physical model tests of wave interaction with a rubble-mound breakwater. *Coastal Engineering*, 103:22–41, 2015. ISSN 03783839. doi: 10.1016/j.coastaleng.2015.05.008. URL http://dx.doi.org/10.1016/j.coastaleng.2015.05.008.

H. Verhagen and J. Van den Bos. Breakwater design: Lecture notes CIE5308. (Draft), 2018.

H. G. Weller, G. Tabor, H. Jasak, and C. Fureby. A tensorial approach to computational continuum mechanics using object-oriented techniques. *Computers in Physics*, 12(6):620, 1998. ISSN 08941866. doi: 10.1063/1.168744. URL http://scitation.aip.org/content/aip/journal/cip/12/6/10.1063/1.168744.

C. N. Whittaker, A. C. Raby, C. J. Fitzgerald, and P. H. Taylor. The average shape of large waves in the coastal zone. *Coastal Engineering*, 114:253–264, 2016. ISSN 03783839. doi: 10.1016/j.coastaleng.2016.04.009. URL http://dx.doi.org/10.1016/j.coastaleng.2016.04.009.

C. N. Whittaker, C. J. Fitzgerald, A. C. Raby, P. H. Taylor, J. Orszaghova, and A. G. Borthwick. Optimisation of focused wave group runup on a plane beach. *Coastal Engineering*, 121(November 2016):44–55, 2017. ISSN 03783839. doi: 10.1016/j.coastaleng.2016.12.001. URL http://dx.doi.org/10.1016/j.coastaleng.2016.12.001.

C. N. Whittaker, C. J. Fitzgerald, A. C. Raby, P. H. Taylor, and A. G. Borthwick. Extreme coastal responses using focused wave groups: Overtopping and horizontal forces exerted on an inclined seawall. *Coastal Engineering*, 140(March):292–305, 2018. ISSN 03783839. doi: 10.1016/j.coastaleng.2018.08.004. URL https://doi.org/10.1016/j.coastaleng.2018.08.004.

J. Zelt and J. E. Skjelbreia. Estimating Incident and Reflected Wave Fields Using an Arbitrary Number of Wave Gauges. *Coastal Engineering*, pages 777–789, 1992. doi: 10.1061/9780872629332.058.

A

Appendix A

Case	H_{m0} [m]	T_p [s]	$T_{m-1,0}$ [s]	h [m]	$\xi_{m-1,0}$ [-]	K_r [-]	Ursell [-]	q_{model} [l/s/m]	q_{proto} [l/s/m]
A1W1T101	0.08	1.82	1.73	0.80	3.77	0.31	3.51	0.004	0.78
A1W1T102	0.10	2.12	1.98	0.80	3.84	0.33	7.59	0.037	8.03
A1W1T103	0.12	2.26	2.22	0.80	3.96	0.36	14.28	0.181	37.36
A1W1T104	0.08	1.45	1.35	0.80	2.97	0.23	1.30	0.001	0.26
A1W1T105	0.10	1.63	1.51	0.80	2.94	0.25	2.57	0.027	5.88
A1W1T106	0.12	1.72	1.66	0.80	2.94	0.28	4.50	0.149	31.34
A1W1T107	0.08	1.14	1.12	0.80	2.50	0.19	0.59	0.000	0.00
A1W1T108	0.10	1.29	1.25	0.80	2.45	0.19	1.16	0.013	2.89
A1W1T109	0.12	1.37	1.37	0.80	2.46	0.20	2.06	0.084	18.13
A1W1T201	0.10	2.03	1.99	0.75	3.86	0.33	9.37	0.002	0.36
A1W1T202	0.12	2.26	2.25	0.75	3.98	0.37	18.48	0.014	2.91
A1W1T203	0.14	2.51	2.47	0.75	4.16	0.40	29.32	0.044	9.59
A1W1T204	0.10	1.63	1.51	0.75	2.94	0.25	3.15	0.001	0.30
A1W1T205	0.12	1.76	1.67	0.75	2.96	0.28	5.65	0.025	5.37
A1W1T206	0.15	1.94	1.87	0.75	3.06	0.29	10.41	0.078	16.55
A1W1T207	0.10	1.24	1.25	0.75	2.47	0.20	1.39	0.002	0.41
A1W1T208	0.12	1.37	1.39	0.75	2.48	0.21	2.60	0.012	2.60
A1W1T209	0.14	1.46	1.50	0.75	2.48	0.22	4.17	0.052	11.32
A1W1T301	0.12	2.26	2.29	0.70	4.06	0.36	24.38	0.000	0.00
A1W1T302	0.14	2.51	2.54	0.70	4.21	0.41	42.13	0.011	2.28
A1W1T303	0.16	2.61	2.79	0.70	4.31	0.45	69.78	0.072	15.48
A1W1T304	0.12	1.72	1.70	0.70	3.01	0.27	7.29	0.001	0.16
A1W1T305	0.15	1.93	1.90	0.70	3.12	0.30	13.59	0.012	2.48
A1W1T306	0.17	2.00	2.11	0.70	3.24	0.32	23.51	0.049	10.49
A1W1T307	0.12	1.37	1.39	0.70	2.49	0.21	3.20	0.000	0.00
A1W1T308	0.14	1.46	1.52	0.70	2.51	0.23	5.43	0.010	2.25
A1W1T309	0.16	1.60	1.64	0.70	2.55	0.25	8.27	0.033	7.13
A3W1T101	0.08	1.82	1.74	0.80	3.76	0.31	3.61	0.037	7.89
A3W1T102	0.11	2.12	1.99	0.80	3.84	0.34	7.93	0.256	54.81
A3W1T103	0.13	2.26	2.23	0.80	3.94	0.36	14.78	0.731	155.82
A3W1T104	0.08	1.45	1.36	0.80	2.96	0.23	1.35	0.014	3.06
A3W1T105	0.11	1.63	1.52	0.80	2.92	0.26	2.64	0.138	29.40
A3W1T106	0.13	1.72	1.68	0.80	2.95	0.28	4.79	0.542	113.10
A3W1T107	0.08	1.14	1.13	0.80	2.51	0.20	0.62	0.005	1.09
A3W1T108	0.10	1.29	1.26	0.80	2.46	0.20	1.23	0.066	14.28
A3W1T109	0.12	1.35	1.39	0.80	2.47	0.21	2.17	0.301	64.22
A3W1T201	0.11	2.03	2.00	0.75	3.84	0.33	9.79	0.022	4.73
A3W1T202	0.12	2.26	2.25	0.75	3.98	0.36	18.28	0.088	18.95
A3W1T203	0.14	2.51	2.48	0.75	4.17	0.39	30.38	0.267	56.74
A3W1T204	0.10	1.63	1.52	0.75	2.93	0.25	3.22	0.010	2.11
A3W1T205	0.13	1.76	1.68	0.75	2.96	0.28	5.80	0.088	18.43
A3W1T206	0.15	1.94	1.88	0.75	3.05	0.29	10.76	0.358	74.68
A3W1T207	0.10	1.29	1.25	0.75	2.46	0.19	1.45	0.010	2.11
A3W1T208	0.12	1.37	1.39	0.75	2.47	0.20	2.67	0.056	11.93
A3W1T209	0.14	1.46	1.51	0.75	2.48	0.22	4.31	0.195	42.18
A3W1T301	0.13	2.26	2.30	0.70	4.02	0.38	25.34	0.010	2.04
A3W1T302	0.15	2.51	2.59	0.70	4.18	0.41	47.52	0.084	17.91
A3W1T303	0.17	2.61	2.81	0.70	4.29	0.46	73.66	0.249	52.10
A3W1T304	0.13	1.72	1.70	0.70	2.98	0.29	7.59	0.016	3.26
A3W1T305	0.15	1.93	1.92	0.70	3.10	0.31	14.29	0.053	11.33
A3W1T306	0.17	2.00	2.13	0.70	3.22	0.33	24.91	0.186	39.08
A3W1T307	0.12	1.37	1.39	0.70	2.47	0.22	3.32	0.009	1.92
A3W1T308	0.15	1.46	1.53	0.70	2.50	0.25	5.71	0.032	6.82
A3W1T309	0.16	1.60	1.65	0.70	2.54	0.27	8.65	0.110	23.69

Table A.1: Hydraulic boundary conditions for all 54 experimental cases. First half containing cases with protruding wave wall, defined by the A1 code. The bottom half containing the cases without protruding wave wall element with code A3. The water depth is described by the T-code, where cases containing T1 are for a water depths of 0.80 m, T2 for 0.75 m and T3 for 0.70 m.

B
Appendix B

B.1. Time lag

A time step error between measured and modelled incoming surface elevations, increasing over time, is captured. Two possibilities are discussed next:

- Numerical diffusion: errors (between modelled and measured) due to the introduction of simplifications and assumptions into the numerical framework compared to the real world. The numerical model is not an exact representation of the experimental flume. However, for each modelled wave traveling towards the structure, the error induced due to numerical diffusion would be the same. Therefore, the induced time lag would be close to constant at a selected wave gauge. However, the time step error increases in time and not over the distance covered by the travelling waves. This rules out numerical diffusion as cause.

- The time steps for which the steering velocities are written out are coarse (0.04 s), two decimals. Therefore, small differences between recorded time steps for which the velocities of the paddle are written off in the physical model and the steering signal used to reconstruct the same wave climate, induce errors over 1800 simulated seconds (1000 waves).

This is solved by applying the following correction (see Equation B.1), to each time step for which the velocity is written out within the original steering file.

$$T_{reduction} = 0 : \Delta T_{lag}/N_{steps} : \Delta T_{lag} \tag{B.1}$$

Where ΔT_{lag} has been established by applying the "finddelay" function in MATLAB at the end of the surface elevation time series. Now modelled and measured signals can be compared by means of RMSE (Root mean squared error) and PCC (Pearson correlation coefficient) values. Before, due to time shifts, the signals could not be compared with the aforementioned statistical parameters.

B.2. Amplification steering paddle

The uncoupled incoming modelled surface elevation spectrum in OceanWaves3D (A2 steering file) and the incoming measured wave signal spectrum, are shown Figure B.1. Table B.1 describes the relation between both signal by means of spectral and statistical parameters. It can be inferred that the base OceanWaves3D steering file generates under dimensioned (**-8%**) incoming wave conditions (in terms of H_{m0}) when comparing to the measured incoming wave conditions. However, when the original steering files (Base = RAW) are compared with the provided steering files within the JIP, amplification factors can be inferred, used in order to achieve improved comparisons between modelled and measured wave incident conditions. The applied technique uses a constant factor over all time steps. In the present research, a frequency based amplification is preferred, explained in intermezzo - Amplification.

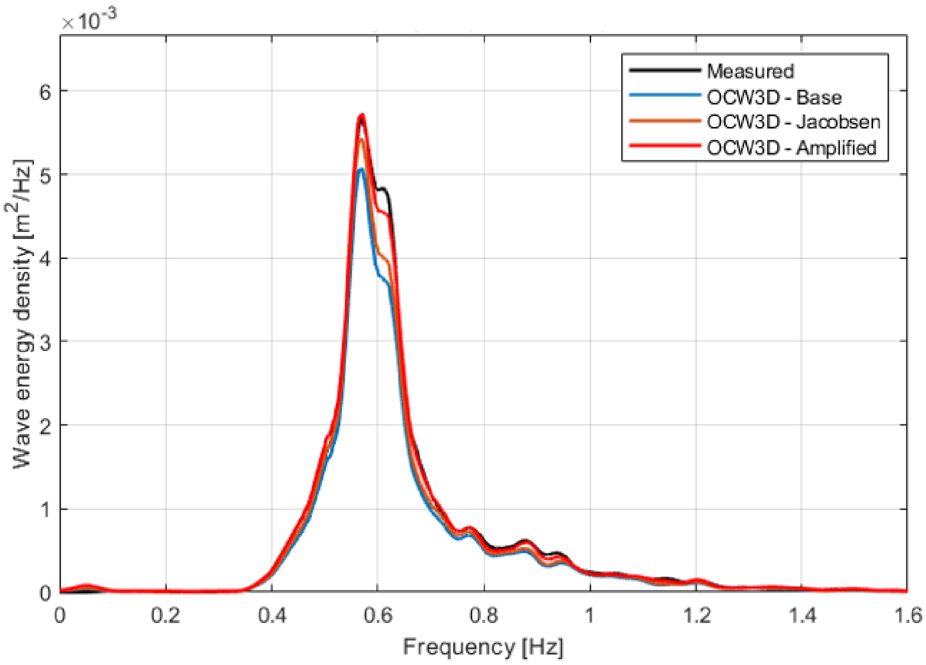

Figure B.1: Incoming modelled and measured spectra at wave gauge closest to structure (5), x = 40.10 m. Showing that the amplification performed in this research performs better in terms of spectral wave height comparison with measurements.

Intermezzo - Amplification

In order to achieve an improved comparison between incoming modelled and measured surface elevations, a frequency based amplification is performed. This required multiple chronological steps:

1. A spectral comparison is made between the base (provided raw steering file) incoming surface elevation modelled within OCW3D (with the non-amplified steering files) and measured incoming surface elevation (achieved after applying the reflection analysis method).
2. Both signals are interpolated to equal time steps, transformed to spectra and divided by each other, giving an amplification factor which varies over the frequency band.
3. The velocity spectrum is obtained from the provided steering files (velocities per time step, interpolated to the equal time steps as the previous two data sets).
4. The square root of the frequency based amplification factor is multiplied with the velocity spectrum, amplifying regions were discrepancies are encountered between modelled and measured signals. Amplifying the velocity spectrum in a range of interest results in amplifications in equal frequency ranges within the wave spectrum.
5. An inverse Fourier transform is executed to the amplified velocity spectrum in order to obtain the amplified steering file, used again as input in OCW3D, resulting in an amplified incoming surface elevation (OCW3D - Amplified = A3).

This process can be done iteratively in order to obtain the optimal match in terms of H_{m0} between the OCW3D and measured incoming wave signal. However, a second iteration step does not improve RMSE and PCC values and therefore the first iteration step is sufficient. Around 500 waves were used to compare the modelled wave conditions with measurements.

According to Table B.1 the amplification applied by Jacobsen et al. (2018) (Jacobsen = B1) showed improved results, compared to the base (Base = RAW) case provided by Deltares, in terms of RMSE and PCC. However, RMSE and PCC values are sensitive for time shifts, which were applied previously to improve the comparability between modelled and measured surface elevations. Therefore the spectral wave height is given more importance as evaluation factor. In that case, the amplification executed in this research (A3) achieved the best result.

Case	RMSE [m]	PCC [%]	Hm0 [%]
OCW3D - RAW	0.0121	92.5	- 8.0%
OCW3D - B1	0.0115	93.3	- 3.7%
OCW3D - A3	0.0122	92.6	+ 0.1%

Table B.1: Statistical and spectral parameters describing the relation between the various OCW3D configurations.

B.3. OceanWaves3D coupling

Comparing the OceanWaves3D (uncoupled) modelled incoming wave climate, detached from OpenFOAM, with the OceanWaves3D (coupled) modelled incoming wave climate extracted from an OpenFOAM run, gives Figure B.2. It can be concluded (see Figure B.2), that under the current conditions (A3) the numerical model is not capable to reproduce extreme waves accurately (high steepness). Upon coupling, **9.6%** of the incoming wave condition (H_{m0}) is lost.

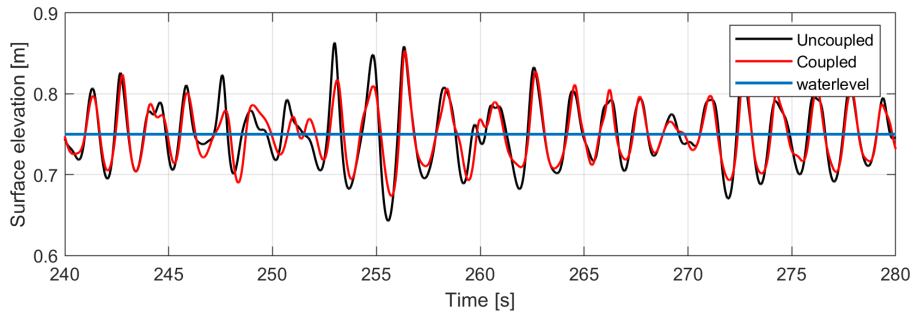

Figure B.2: Incident surface elevation captured at wave gauge closest to structure (No. 5), x = 40.10 m, showing the the discrepancies in modelling the incident surface elevations (extreme waves) when OceanWaves3D is coupled to OpenFOAM.

The aforementioned phenomenon is caused by the coupling between OpenFOAM and OceanWaves3D, done by Paulsen et al. (2013). To solve the problem, the resolution in the propagation direction of the incoming waves (x-direction) needs to be increased, within OceanWaves3D domain. Instead of having 85 grid points (which is much higher as the horizontal 10 grid points per leading wave length suggested by Paulsen et al. (2013)) per leading wave length (N_x) the number of grid points was doubled to 170. Various other set-ups have been tested, varying: time steps, Courant numbers and y-resolution, however, without any success. Therefore, all x-directed resolutions of the provided OceanWaves3D.input files were increased, ensuring good quality upon coupling. Applying the presented solution gives significant improvements in terms of spectral wave heights H_{m0}, losing **2.5%**, (see Figure B.3).

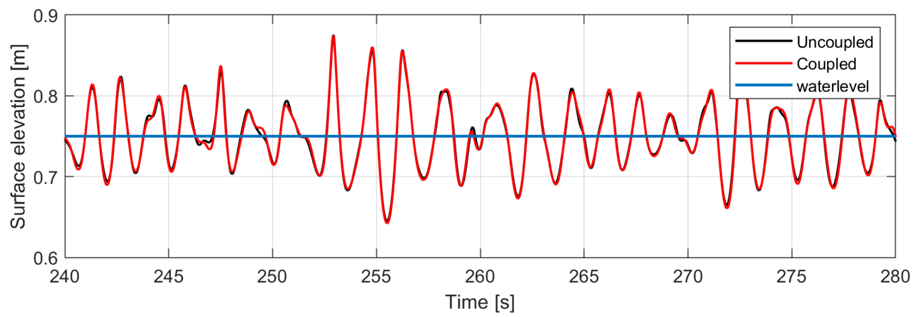

Figure B.3: Incident surface elevation captured at wave gauge closest to structure (No. 5), x = 40.10 m, showing the improvement in coupling when adopting the proposed solution.

The reduction in H_{m0} can be further reduced by increasing the resolution, however, the computational time it would require is not worth the improvement in accuracy it would yield.

B.4. Reflection structure

The reflection of the structure is too high ($K_{r,mod}$ = 0.34) compared to measurements ($K_{r,mes}$ = 0.28). The bulk reflection of the rubble mound breakwater depends on various parameters, e.g. Irribarren number, the angle of the slope and the porous flow properties. As the first two factors can not be altered, a closer look is given to the parametrisation by van Gent (1995) to describe the porous flow through the various layers of which the breakwater consists. In the upcoming sections the n (porosity), α, β and KC coefficients are discussed.

Porosity

Increasing of the porosity lowers both resistance coefficients (a and b), reducing the resistance the incoming flow experiences and therefore reduces the reflection coefficient. The porosity of all layers in the numerical model has been set at 0.40, however, this was done without measuring it during the physical laboratory experiments. The Rock Manual 2007 (CIRIA et al., 2007b) suggests to use formulas (see Equations B.2 and B.3) to predict the average porosity for different gradings and shape characteristics. The Equation applies to all bulk-placed granular materials (core, filter and armour). The procedure was briefly discussed in Chapter 5. Here the methodology is elaborated. A procedure, estimating the porosity based on the grain size distribution parameters, such as the uniformity index of the Rosin-Rammler (Ros-Ram) curve based on the grain diameter, n_{RRD}.

$$n_v = \frac{1}{90} \cdot (e_0) \cdot \arctan(0.645 \cdot n_{RRD}) \cdot \frac{180}{\pi} \tag{B.2}$$

$$n_v = \frac{e}{1+e} \tag{B.3}$$

Where, e is the void ratio equal to the volume of voids divided by the volume of solids, e_0 the void ratio associated to the single-size particles of different shapes and n_v the bulk porosity of the granular material. For typically mechanical crushed the single-size void ratio (e_0) ranges between 0.92-0.96 and is taken as 0.94 here. In order to find the uniformity index describing the shape of the Ros-Ram curve, the gradings of the granular materials are needed. The following gradings, for the different layers, were reported by Deltares and are listed in Table B.2. The grading curves are shown below. The Ros-Ram equation describes the typical shape of the mass/size grading curves and will be used here to estimate the bulk porosity of the granular materials.

Type	**Laboratory scale**			**Prototype scale**					
Layer	Dn_6 [mm]	Dn_{50} [mm]	Dn_{90} [mm]	Dn_6 [mm]	Dn_{50} [mm]	Dn_{90} [mm]	M_6 [kg]	M_{50} [kg]	M_{90} [kg]
Armour	20.6	32.1	52.4	741.6	1155.6	1886.4	1080.8	4089.5	17788.8
Filter	11.5	16.5	23.8	414.0	594.0	856.8	188.0	555.4	1666.8
Core	3.9	6.3	9.0	140.4	226.8	324	7.3	30.9	90.1

Table B.2: Grading parameters for different subdivisions of the rubble mound breakwater, on laboratory and prototype scale.

According to the Rock Manual 2007 guidelines the mass uniformity index (n_{RRM}) can be determined given any two fixed points on Ros-Ram curve (see Equations B.4-B.8). In practice, the nominal lower limit mass of a grading (NLL) with the maximum allowable passing fraction y_{NLL}, and similarly the nominal upper limit mass of a grading (NUL) with the the maximum allowable passing fraction y_{NUL}, are set as two fixed points on the Ros-Ram curve. Combining both equations solves for the the mass uniformity index, based on the pre-determined fractions of passing.

$$y = 1 - \exp \cdot \left(\ln\left(\frac{1}{2}\right) \cdot \frac{M_y}{M_{50}}^{n_{RRM}} \right) \cong 1 - \exp \cdot \left(-0.693 \cdot \frac{M_y}{M_{50}}^{n_{RRM}} \right) \tag{B.4}$$

the inverse:

$$M_y = M_{50} \cdot \left(\frac{\ln(1-y)}{\ln\left(\frac{1}{2}\right)} \right)^{1/n_{RRM}} \cong M_{50} \cdot \left(\frac{-\ln(1-y)}{0.693} \right)^{1/n_{RRM}} \tag{B.5}$$

two fixed points:

$$M_{50} = NNL \cdot \left(\frac{\ln(1-y_{NNL})}{-0.693} \right)^{-1/n_{RRM}} \tag{B.6}$$

$$M_{50} = NUL \cdot \left(\frac{\ln(1-y_{NUL})}{-0.693} \right)^{-1/n_{RRM}} \tag{B.7}$$

reworked:

$$n_{RRM} = \frac{\log\left(\frac{\ln(1-y_{NUL})}{\ln(1-y_{NNL})}\right)}{\log\left(\frac{NUL}{NLL}\right)} \tag{B.8}$$

Where, y is the fraction passing value depending on the grading type (EN 13383 standard grading) of the granular material, M_y is the mass of the granular particles corresponding to the fraction of passing and n_{RRM} the mass uniformity index which is a measure for the steepness of the grading curve. In order to find the EN 13383 standard gradings of the materials used during the experiments, the prototype rock masses were computed (ρ_{rock} = 2650 kg/m^3, scale factor 36x) and are listed in Table B.2. The coefficient relating the nominal diameter (D_n) with the diameter (D) is taken as 0.84. The EN 13383 standard grading table listed in Bed Bank and Shore protection (Schierirck and Verhagen, 2016) shows that the gradings can be classified as heavy (armour), heavy (filter) and light (core). According to the Rock Manual 2007 the fraction of passing (y_{NLL} and y_{NUL}) in cases of light-heavy gradings can be chosen as 6% and 90% respectively. From the attached grading curves provided by Deltares (see Figures B.4, B.5 and B.6), the $M_{6\%}$ and $M_{90\%}$ can be estimated which are used to re-evaluate n_{RRM}. This resulted in the following n_{RRM} values, **1.29** for the armour layer, **1.66** for the filter layer and **1.47** for the core. Finally, the average bulk porosity of the granular materials can be estimated, using Equations B.2 and B.3, where n_{RRD} = 3 $\cdot n_{RRM}$, giving:

- n_{Armour} = **0.416**
- n_{Filter} = **0.432**
- n_{Core} = **0.425**

Plugging in the re-evaluated porosities and D_{n50}, following the guidelines mentioned in the Rock Manual 2007, the reflection coefficient $K_{r,modelled}$ remains 0.34. The adaptations did not reduce the reflection sufficiently and therefore additional changes are needed to lower the bulk reflection.

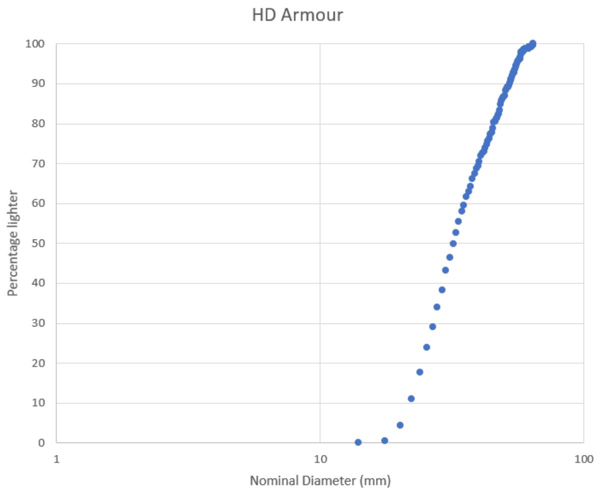

Figure B.4: Measured sieving curve of the armour layer in the physical flume.

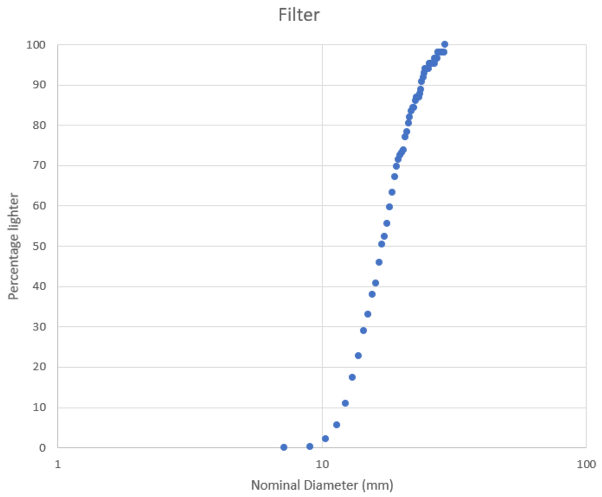

Figure B.5: Measured sieving curve of the filter layer in the physical flume.

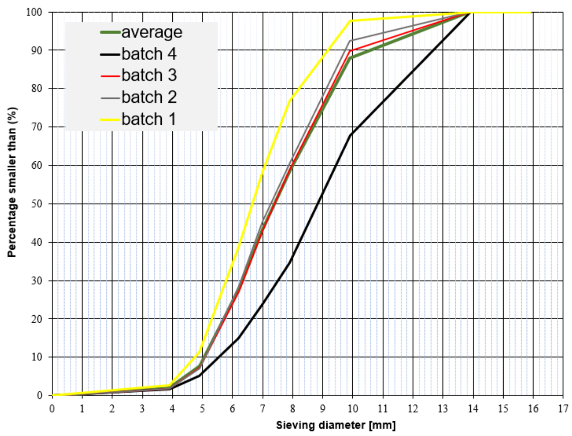

Figure B.6: Measured sieving curve of the core in the physical flume. Four different batches were used to construct the core of the breakwater in the physical flume. All four sieve curves are plotted against each other.

α, β and KC

From all the considered dimensionless porous flow coefficients sets by Losada et al. (2016) the technique proposed by Jensen et al. (2014) is investigated here. Jensen et al. (2014) extended the research by comparing experimental data sets with numerical model outcomes (using OpenFoam) for different flow regimes (based on the porous Reynolds Re_p number) and ranges of dimensionless coefficients (α and β). Four different flow regimes were characterised, the Darcy flow regime (laminar) $1 < Re_p < 10$, the Forcheimer flow regime $10 < Re_p < 150$, the transitional flow regime $150 < Re_p < 300$ and the fully turbulent flow regime $300 < Re_p$. The regimes were determined based on the porous Reynolds number and reconstructed with different dam break configurations. Three experimental laboratory test were set up to represent each type of flow regime (except the laminar flow regime), which the numerical model tried to mimic by running several simulations with different dimensionless coefficients (α and β). From this, three graphs were derived (see Figures B.7a, B.7b and B.7c). Each graph displays the errors introduced by the numerical model when comparing modelled with measured surface elevations representing the dam break flow, for different combinations of coefficients. As the recommended coefficients according to van Gent (1995) produced a $K_{r,mod}$ which is too high, the ranges which introduced acceptable errors reported by Jensen et al. (2014) are selected and studied next. However, first the type of flow regime needs to be determined. The porous Reynolds number is calculated using Equation B.9.

$$Re_p = \frac{\langle \bar{u} \rangle \cdot D_{n50}}{n \cdot \nu} \tag{B.9}$$

Where, $\langle \bar{u} \rangle$ is the flow velocity averaged per time step and over each control volume (representing the most probable occurring flow regime in each cell) and ν the kinematic viscosity which at $18°$ is equal to 1.053e-06 m^2/s. Evaluating the type of flow is an iterative process (as the flow velocity will change for different porosities and dimensionless resistance coefficients), however, here the reference case is taken as first estimate. The Re_p values will vary per cell, from which contour lines describing the flow type over the breakwater can be derived. Instead of looking at the variation over all cells, the average is taken over all cells contained within each layer type. The following flow regimes are found:

- $Re_{p,Armour}$ = 4468.1 - fully turbulent flow regime
- $Re_{p,Filter}$ = 1050.0 - fully turbulent flow regime
- $Re_{p,Core}$ = 57.6 - Forcheimer flow regime

All flow regimes lie within the region where a non-linear relation between the resistance and the flow rate appears. For the armour and filter layer the third graph (turbulent flow; see Figure B.7c) can be used. Jensen et al. (2014) noticed that in case of turbulent flow the dependency on the turbulent coefficient β is high, which was also noticed by Losada et al. (2008). In case of the core the first graph, Figure B.7a, must be used for the selection of a set of dimensionless coefficients. From all the foregoing the following sets are tested in the numerical model (1) α = 500, β = 2 for each layer and (2) α = 0.001, β = 1.1 for armour and filter and α = 250, β = 0.75 for the core.

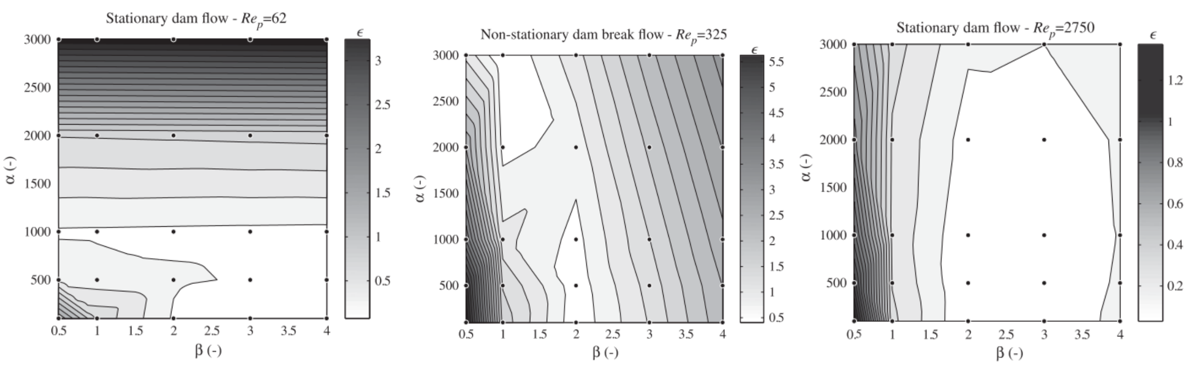

(a) Re_p = 62. (b) Re_p = 325. (c) Re_p = 2750.

Figure B.7: The α dimensionless resistance coefficient plotted against the β dimensionless resistance coefficients. Contours of the error between simulated and experimental surface elevations, using a set of dimensionless resistance coefficients, for different flow regimes (characterised by the porous Reynolds number (Re_p)).

C

Appendix C

C.1. Spectrum fit

The following figures show the spectrum fit applied to the measured incident wave conditions for each studied incoming wave condition (T201-T209), except the ones already reported in Chapter 6.

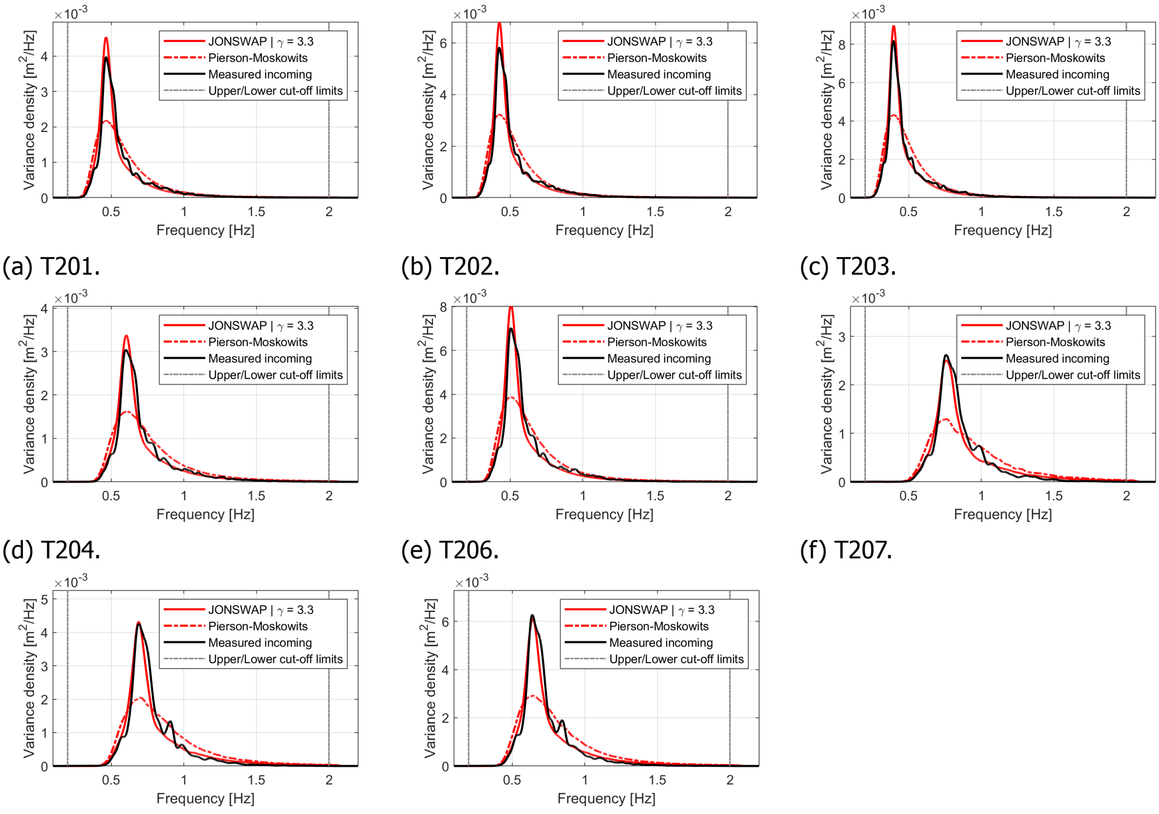

(a) T201. (b) T202. (c) T203.

(d) T204. (e) T206. (f) T207.

(g) T208. (h) T209.

Figure C.1: Showing two possible spectrum fits applied to the incoming wave spectrum. Where the JONSWAP (γ = 3.3) showed a good comparison with the measured incoming spectrum. Grey lines showing the threshold cut-off limits f_{LC} and f_{HC}. Cases T201 to T209 without T205.

C.2. Composite Weibull distribution

The following figures show the Composite Weibull distribution for each studied incident wave condition (T201-T209), except the ones already reported in Chapter 6, compared with the incident measured wave heights. The latter were obtained by applying a reflection analysis combined with a zero-down crossing method.

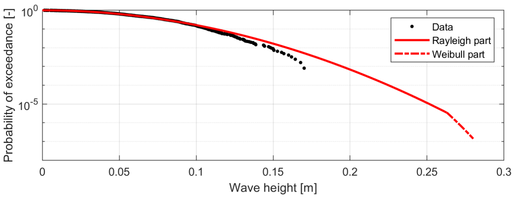

(a) T201.

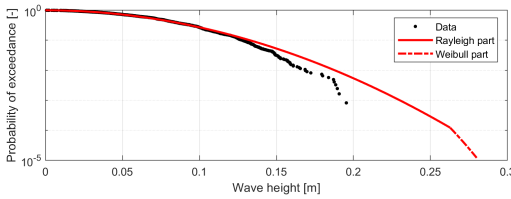

(b) T202.

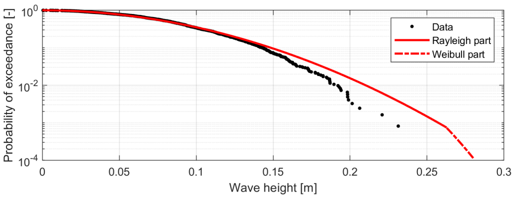

(c) T203.

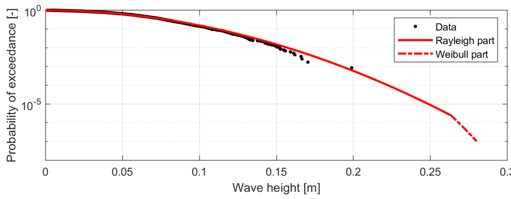

(d) T204.

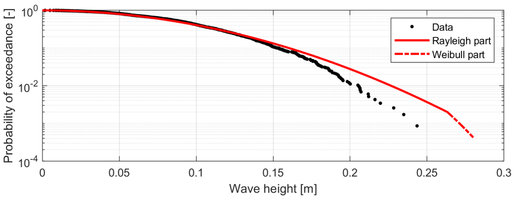

(e) T206.

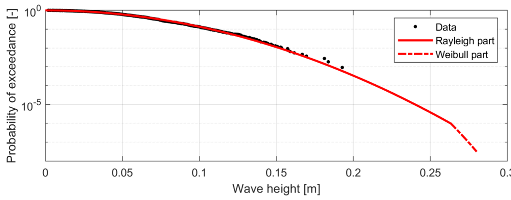

(f) T207.

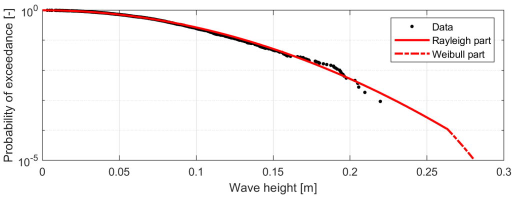

(g) T208.

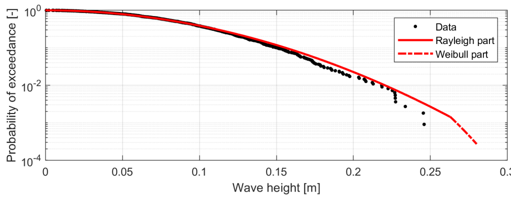

(h) T209.

Figure C.2: Composite Weibull exceedance curve for incoming wave heights considering cases T201 to T209 without T205, showing a Rayleigh distribution (red) until the threshold wave height and from there a Weibull distribution (red dotted line).

C.3. NewWave profiles in OceanWaves3D

The following figures show a comparison between the theoretical NewWave profile using NewWave theory versus the NewWave profile generated in OceanWaves3D, for all the studied incoming wave conditions (T201-209) except the ones already reported in Chapter 6. As already reported, the magnitude of the spurious waves (in OceanWaves3D) increases with increasing degree of non-linearity which is also seen here.

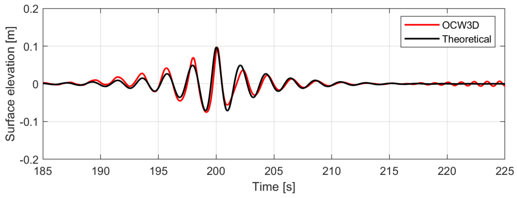

(a) T201.

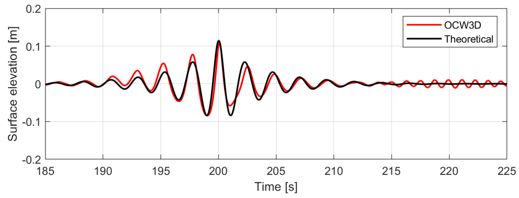

(b) T202.

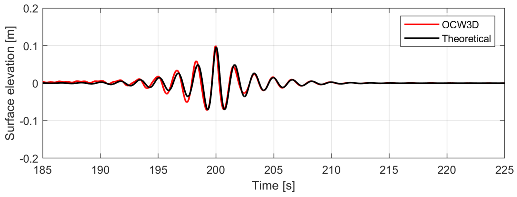

(c) T204.

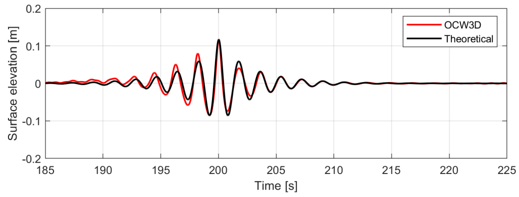

(d) T205.

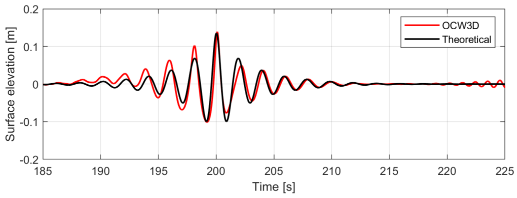

(e) T206.

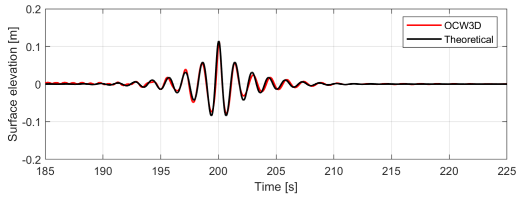

(f) T208.

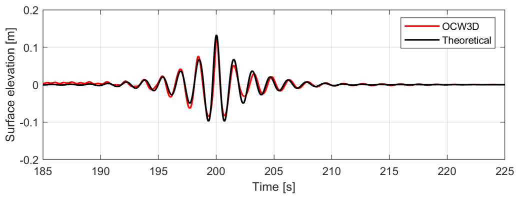

(g) T209.

Figure C.3: Incident surface elevation measured at focusing point, including a comparison between: the OceanWaves3D model generated surface elevation using a first-order wave generation and the theoretical NewWave profile according to NewWave theory, for cases T201 to T209 without T203 and T207.

C.4. Filtering out the spurious waves

The spurious long error wave, inducing a set-up in front of the NewWave profile, is filtered out using a frequency cut-off filter. This is done to study the importance of the long error wave per case. As already reported, the magnitude of the long error wave relative to the input crest elevation was highest for the most non-linear case T203. Here the cases not reported in Chapter 6 are shown.

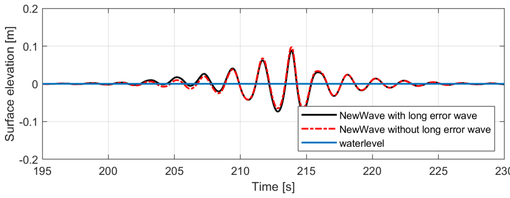

(a) T201.

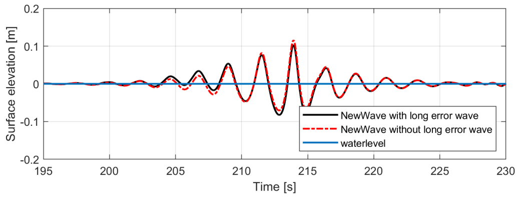

(b) T202.

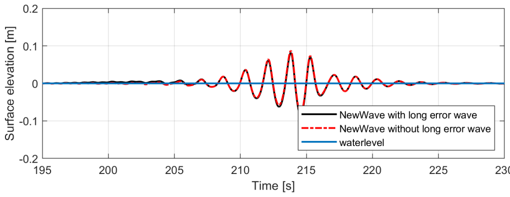

(c) T204.

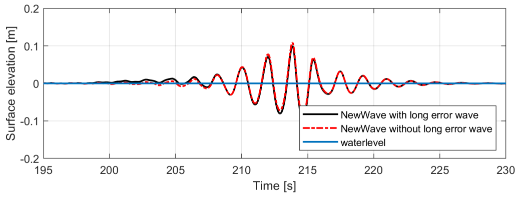

(d) T205.

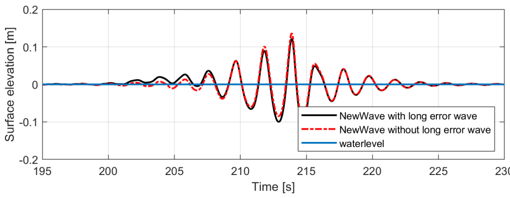

(e) T206.

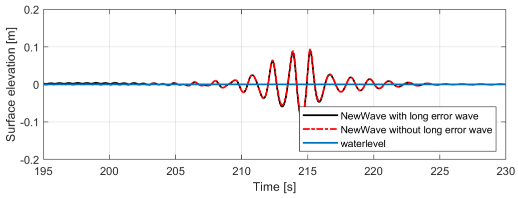

(f) T208.

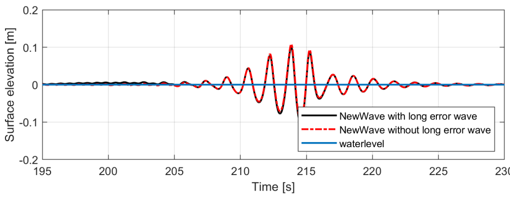

(g) T209.

Figure C.4: A comparison between the NewWave profile containing the low frequency error wave (black line) and the NewWave profile where the low frequency wave is filtered out (red dotted line), showing the induced set-up in front of the incident NewWave profile for highly non-linear cases such as T206 for example. Cases T201-T209 are shown except T203 and T207.

D

Appendix D

D.1. Cumulative overtopping figures

In this section the modelled cumulative overtopping curves using the calibrated numerical model (CoastalFOAM) are compared with measurements and the EurOtop 2018 method (updated γ_f = 0.53), ordered from large to small overtopping discharges.

D.1.1. Large overtopping discharge

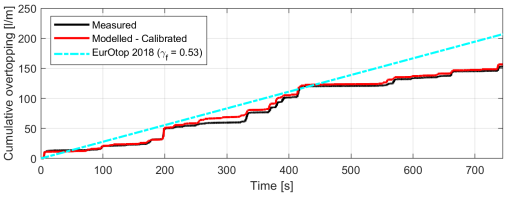

(a) Non-protruding wave wall case.

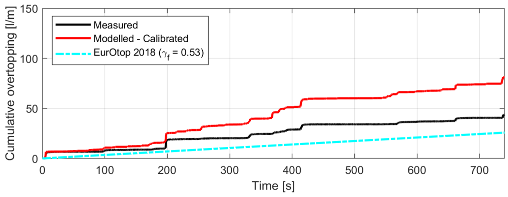

(b) Protruding wave wall case.

Figure D.1: Cumulative overtopping results for a large overtopping discharge for (a) a non-protruding wave wall and (b) a protruding wave wall, including a comparison between: physical laboratory measurements, the improved numerical model and the updated EurOtop 2018 guideline.

D.1.2. Medium overtopping discharge

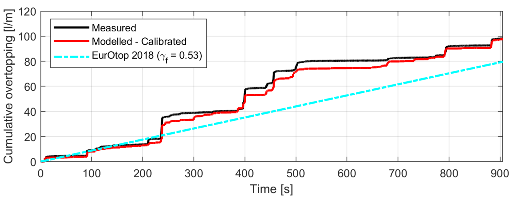

(a) Non-protruding wave wall case.

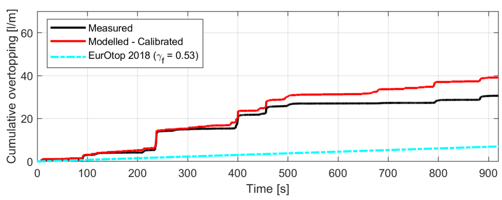

(b) Protruding wave wall case.

Figure D.2: Cumulative overtopping results for a medium overtopping discharge for (a) a non-protruding wave wall and (b) a protruding wave wall, including a comparison between: physical laboratory measurements, the improved numerical model and the updated EurOtop 2018 guideline.

D.1.3. Small overtopping discharge

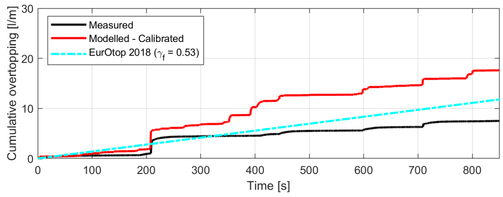

(a) Non-protruding wave wall case.

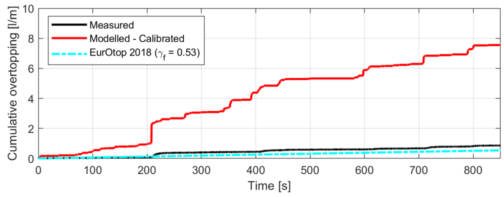

(b) Protruding wave wall case.

Figure D.3: Cumulative overtopping results for a small overtopping discharge for (a) a non-protruding wave wall and (b) a protruding wave wall, including a comparison between: physical laboratory measurements, the improved numerical model and the updated EurOtop 2018 guideline.